Intracortical recordings reveal Vision-to-Action cortical gradients driving human exogenous attention

Tal Seidel Malkinson*[1,2], Dimitri J. Bayle[3], Brigitte C. Kaufmann[1], Jianghao Liu[1,4], Alexia Bourgeois[5], Katia Lehongre[6], Sara Fernandez-Vidal[6], Vincent Navarro[1,7,8], Virginie Lambrecq[1,7,8], Claude Adam[1,7,8], Daniel S. Margulies[9], Jacobo D. Sitt[1], and Paolo Bartolomeo[1]

[1] Sorbonne Université, Inserm UMRS 1127, CNRS UMR 7225, Paris Brain Institute, ICM, Hôpital de la Pitié-Salpêtrière ; 75013 Paris, France
[2] Laboratoire IMoPA, UMR 7365 CNRS, Université de Lorraine, Biopôle de l'Université de Lorraine, Vandoeuvre-lès-Nancy Cedex, France
[3] Licae Lab, Université Paris Ouest-La Défense ; 92000 Nanterre, France
[4] Dassault Systèmes, Vélizy-Villacoublay, France
[5] Laboratory of Cognitive Neurorehabilitation, Faculty of Medicine, University of Geneva; 1206 Geneva, Switzerland
[6] CENIR - Centre de Neuro-Imagerie de Recherche, Paris Brain Institute, ICM, Hôpital de la Pitié-Salpêtrière ; 75013 Paris, France
[7] AP-HP, Epilepsy and EEG Units, Pitié-Salpêtrière Hospital, 75013 Paris, France
[8] Reference center of rare epilepsies, EpiCare, Pitié-Salpêtrière Hospital, 75013 Paris, France
[9] Laboratoire INCC, équipe Perception, Action, Cognition, Université de Paris ; 75005 Paris, France
* Corresponding author. Email: tal.seidel@mail.huji.ac.il

Abstract

Exogenous attention, the process that makes external salient stimuli pop-out of a visual scene, is essential for survival. How attention-capturing events modulate human brain processing remains unclear. Here we show how the psychological construct of exogenous attention gradually emerges over large-scale gradients in the human cortex, by analyzing activity from 1,403 intracortical contacts implanted in 28 individuals, while they performed an exogenous attention task. The timing, location and task-relevance of attentional events defined a spatiotemporal gradient of three neural clusters, which mapped onto cortical gradients and presented a hierarchy of timescales. Visual attributes modulated neural activity at one end of the gradient, while at the other end it reflected the upcoming response timing, with attentional effects occurring at the intersection of visual and response signals. These findings challenge multi-step models of attention, and suggest that frontoparietal networks, which process sequential stimuli as separate events sharing the same location, drive exogenous attention phenomena such as inhibition of return.

Keywords

Attention, intracerebral recordings, cortical gradient, timescales, inhibition of return, response time, frontoparietal networks

Introduction

Imagine sitting in your car, waiting for the traffic light to change when suddenly an adjacent billboard sign starts flashing, capturing your attention. How would the flashing sign affect your ability to subsequently detect the light changing to green? In such a situation, the flashing automatically renders the sign more salient in the visual scene through a fast and dynamic orientation process known as exogenous attention. Exogenous attention is a fundamental process that modulates response speed and perceptual sensitivity [1], and is prevalent among many vertebrate species [2–4], yet the expansion of attention systems in the human brain sets us apart [5]. Understanding how our brain handles such salient distractions has become ever more crucial in our information-saturated modern environment. Yet, what exactly determines if our attention will be captured or reoriented away is not clear. Attention's temporal dimension, that is, how a previous stimulus such as a salient attention-capturing cue affects the processing of a subsequent stimulus, such as a target, is a key element for answering this important question. For instance, when successive stimuli appear at the same location within short delays, they lead to faster performance (response time (RT) facilitation). Slightly longer delays, however, slow down responses, a phenomenon termed inhibition of return (IOR), which may promote spatial exploration [6,7]. Under certain conditions (e.g. when cue and target do not overlap in time), IOR may even offset RT facilitation [8]. These opposing RT modulations reflect underlying attentional processes [9]. However, the corresponding neural mechanisms remain uncertain. Despite decades of research, the nature and underlying neural mechanisms that mediate these attentional effects remain unclear [10,11]. Evidence from human and non-human studies suggests that information about physical salience, which guides exogenous attention, may emerge as early as primary visual cortex, but this is still debated [12,13]. There are mixed results about the brain localization of such activities and the specific stimulus features that elicit exogenous attention [14–16]. Salience information converges with top-down influences in several higher-order areas related to attention [13,17,18]. In humans, attention-related networks include a dorsal frontoparietal network and a more right-lateralized ventral network, comprising the temporoparietal junction (TPJ) and the ventral prefrontal cortex [19]. Global salience may be computed within salience maps in the parietal cortex [18,20–22] or the prefrontal cortex [22–24], as well as in subcortical structures such as the superior colliculi and the pulvinar [25]. Several of these areas, such as the superior colliculi, the frontal eye fields (FEF), the posterior parietal cortex, and their connections were also shown to be involved in IOR [26–34]. For example, dysfunction of these regions in the right hemisphere [35] causes spatial neglect, a condition characterized by a failure to orient attention to left-sided events and persistent RT facilitation instead of the typical IOR for right-sided targets [33,34], linking abnormal exogenous attention to this disabling neurological condition. However, there is no consensus regarding the exact nature and neural basis of IOR [10,36] and very little effort was directed into exploring the neural basis of RT facilitation, with no single neural marker of these effects identified [11]. There are several contentious neural theories of IOR, but very few about RT facilitation and the evidence supporting each of them is limited, indirect and often contradictory. Theories of IOR diverge on the mechanistic nature of IOR and its putative localization(s) in the brain (sensory/attentional and/or motor/decisional). It was suggested, for instance, that IOR is caused by attentional capture of previously cued locations [37], perhaps by delaying bottom-up signals of the salience map [26,27,38], or by an inhibitory attentional bias [39,40]. A recent theoretical model based on the known architecture of frontoparietal cortical networks and on their anatomical and functional asymmetries [41], proposed that IOR, that arises from a noise-increasing reverberation propagation of activity within priority maps of the frontoparietal circuit linking frontal eye field (FEF) and intraparietal sulcus (IPS) [42]. Other theories proposed that IOR might occur early, over perceptual neural pathways through the reduction of stimulus salience around a previously attended location [43], or due to sensory adaptation [44] or habituation [45]. IOR was suggested to occur also later in processing, involving motor/decision circuits, in the form of a bias against responses toward previously attended spatial locations [43], motor habituation [45] or an oculomotor activation signal [46]. For example, the Cue-target event integration-segregation hypothesis [47] postulates that the summation of early and late perceptual processes, spatial selection processes and decision processes, determines together if the net behavioral effect is facilitatory (RT facilitation) or inhibitory (IOR) [6,11]. According to this theory, binding together of sequential stimuli that share similar features (such as location and close-timing) into a single event file [48], can lead to facilitatory effects helping to select the target location in advance [6]. However, binding can also cause inhibitory effects when the similar sequential stimulus needs to be detected as a new separate event, resulting in a cost in detecting the onset of the target [6]. These theories remain highly debated, and the evidence supporting each one is inconclusive. This is due at least in part to the fact that prior work investigating the neural basis of these fast and dynamic processes is quite sparse, and based either on high-resolution recordings in specific brain regions in non-human primates, or on indirect human neuroimaging methods with limited spatial resolution, such as EEG, or with limited temporal resolution, such as functional MRI. These considerations are critical when studying the neural correlates of exogenous attention, which operates on a very rapid time scale and dynamically involves large neural networks over the entire brain, thus rendering past findings not informative enough for supporting or refuting existing neural theories of attention. Thus, our understanding of these attention processes stays fragmented, leaving the involved networks and underlying mechanism obscure.

Here we set out to establish the large-scale spatiotemporal neural dynamics of the mechanisms involved in the exogenous orienting of spatial attention. We chose to use intracortical EEG (iEEG) in humans [37–39], acquired across 28 patients (1,403 contacts), to achieve comprehensive cortical coverage. iEEG is the only method that allows to track human attentional dynamics directly (i.e. invasively) with high temporal resolution and excellent spatial precision over large brain topographies, crucial for capturing rapid attentional dynamics across the brain. Because of the lack of consensus on the neural basis of exogenous attention, we chose to use a data-driven approach, leveraging the advantages of iEEG to establish how neural activity tracks visual, attentional and response aspects of the classic Posner exogenous attention task [7] and test whether the findings converge with existing theoretical frameworks. This approach allowed us to study the impact of attentional cues on the detection of subsequent targets, as a function of the delay between them. Typically, depending on the congruence between cue and target locations and the cue-target delay, this task generates differences in RT (RT facilitation or IOR) [7,8]. We assumed that the activity of putative neural mechanisms underlying these exogenous attention RT effects should present: 1) visual spatial sensitivity; 2) sensitivity to cue-target delay; 3) sensitivity to task relevance (cue/target); 4) association with RT.

To study how the evoked activity relates to large-scale brain organization, we examined its mapping across the cortical gradient, an axis of variance in anatomical, functional, neurodevelopmental and evolutionary features, along which areas fall in a spatially continuous order [49–52]. The cortical gradient is a recently discovered organizing principle of cortical topography [49,51], based on the differentiation of connectivity patterns that captures a spatial and functional spectrum from early regions dedicated to perception and action (Periphery) to high-level regions of more abstract cognitive functions (Core) [51], akin to Mesulam's [53] unimodal-to-transmodal cortical hierarchy. Therefore, localizing activity along this gradient indicates the microstructural and genetic features, connectivity profile, and functional role of the activated region [49,50].

This combined approach sought to clarify the theoretical debate on the neural basis of exogenous attention by tracking precisely its neural correlates and mapping them onto the large-scale topography of the brain.

Results

Twenty-eight participants undergoing presurgical evaluation of their epilepsy with iEEG (age 31.7 ± 8.1 years, 15 women, Table 1) performed the Posner peripheral cueing detection task [7] (Fig. 1A). Participants were asked to press a central button as soon as a target (an X) appeared within a left- or right-sided placeholder box. A non-predictive peripheral cue (a 100-ms thickening of contour of one box) preceded the target with two possible stimulus onset asynchronies (SOA): 150ms (short-SOA), or 600ms (long-SOA), and appeared either on the same side of the target (Congruent trials) or opposite side (Incongruent trials) with equal probability.

Patients' performance was neurotypical [6,7], with a 30-ms IOR effect (Fig. 1B; 2-way-ANOVA: SOA X Congruence interaction, $F_{(1,27)}=39.50$, $p<0.001$, $\eta^2=0.164$; post-hoc test: long-SOA congruent vs. Incongruent $p<0.001$). Congruent and incongruent RTs differed between SOAs (post-hoc tests: $p=0.047$ and $p=0.008$, respectively), but facilitation at short-SOA failed to reach significance ($p=0.37$; see Fig. S1 for individual RT effects and target-side analysis), as is often the case with this subtle effect [8]. Moreover, left target Congruent RTs were slower than right target Congruent RTs, across both SOAs (Fig. S1B; repeated-measures 3-way ANOVA: Target-side X Congruence interaction- $F_{(1,27)}=8.28$, $p=0.008$, $\eta^2=0.007$), reflecting a Poffenberger effect [54,55], i.e. faster RTs for right cue & target than for left cue & target, when responding with the right hand. In Incongruent trials in which cue & target appear at opposite sides of the screen, this effect might have averaged out. No other Target-side effects reached significance, and IOR and RT facilitation effects did not significantly differ between left-sided and right-sided targets (paired samples t-test; IOR side: $t(27)=1.83$, $p=0.077$; RT Facilitation side: $t(27)=1.68$, $p=0.11$). Catch trials were not statistically analyzed because of their small number, but patients never responded in those trials.

High-frequency broadband power (HFBB; 55-145Hz) was extracted from 1,403 usable contacts with bipolar montage, pooled across all participants (Fig. 2A; See Table 2 for detailed localization). Target-locked mean normalized HFBB activity was computed for each contact in the eight experimental conditions (2x2x2 design: SOA x Congruence x Ipsilateral/Contralateral target relative to contact; Fig. 2A).

The following steps were taken in the neural analysis approach. We first aimed to identify contacts with similar temporal activity across all conditions in a data-driven manner, using an adapted clustering trajectory k-means algorithm, which operated on the contacts target-locked temporal responses. We next explored the temporal progression of activity between the identified clusters. Given that the clusters were defined only based on their temporal dynamics, we then investigated the clusters' spatial localization, their white matter connectivity and their spatial relations within the large-scale hierarchy of the cortical gradient, testing the prediction that meaningful clusters will group spatially in an ordered manner. We then turned to characterize how the neural activity across the clusters tracked visual, attentional and response aspects of the Posner paradigm. Specifically, (1) we tested attentional effects by comparing neural activity across the attention contrasts used for the behavioral analysis; (2) We revealed response-related modulation by examining how differentiating target-locked activity according to the RT affected neural activity; (3) We uncovered visual modulation of neural activity by applying the clustering anew to response-locked activity and studying how separating response-locked activity according to visual stimuli onset time influenced the clusters' neural activity. Finally, (4) we investigated whether the embedding of the cluster gradient in the cortical gradient extends beyond spatial topography and shares a functional hierarchy of temporal integration windows, which could correspond to a proposed theoretical mechanism underlying RT facilitation and IOR [6,42].

In order to reveal the main temporal patterns of activity that were sensitive to the experimental manipulations in a data-driven manner, we customized an unsupervised trajectory-clustering approach based on the k-means algorithm to cluster iEEG contacts according to their dynamic temporal patterns of activity across experimental conditions (Fig. S2). First, we selected responsive contacts, i.e. contacts with a significant effect in one condition or more, compared to baseline, which lasted at least 100ms, for inclusion in the clustering analysis. This resulted in 644 responsive contacts, for each of which we calculated the temporal trajectory in the 8-dimensional condition space (Congruent / Incongruent Trial X short-SOA / long-SOA X Ipsilateral / contralateral target; see Fig. S2A-B), i.e. the path of each contact's HFBB over time across all experimental conditions. Each contact trajectory was then assigned to the cluster with the nearest trajectory-centroid, by iteratively minimizing within-cluster Manhattan distances. For further analyses, we used a *k*=6 solution, chosen using the Elbow method (see Fig. S2C, Fig. S3 and Table S1 for cluster number and stability across different k solutions, and Fig. S4A for the distribution of cluster contacts within participants).

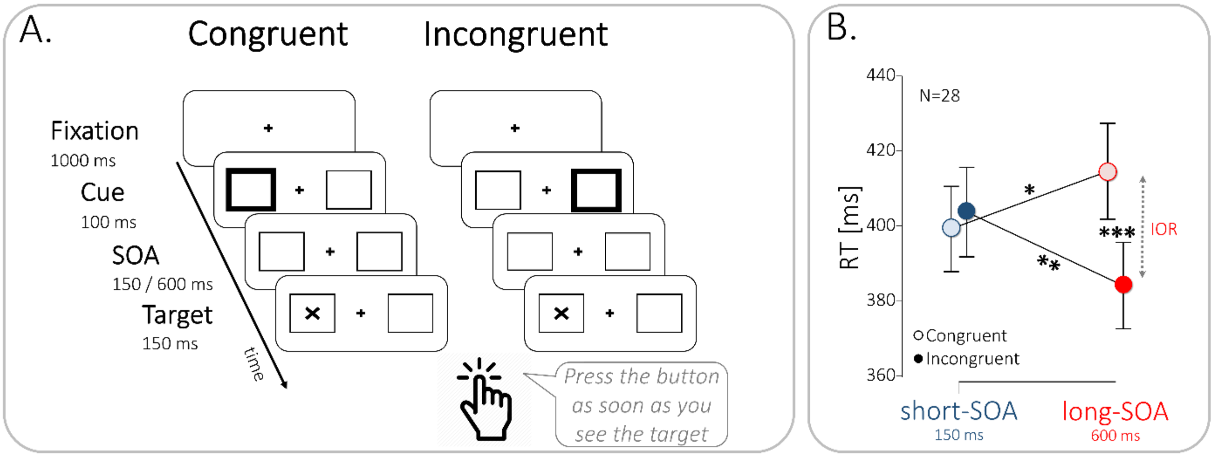

Figure 1 - Neurotypical performance of implanted patients in the Posner task. (A) Illustration of the Posner cued detection task. After 1000ms of fixation, a cue (thickened placeholder) appeared for 100ms at either side of the screen. On short SOA trials (short-SOA), the target (the letter X) occurred 150ms after cue onset; on long SOA trials (long-SOA) the target appeared 600ms after cue onset. The target appeared either on the same side of the screen as the cue (Congruent condition), or on the opposite site (Incongruent condition). Patients were required to press a central button with their right hand, as soon as the target appeared, while maintaining central fixation throughout stimuli presentation. Catch trials (n=24) had the same duration and cue presentation, but no target followed the cue. All trial types (n=336) were equiprobable and randomly interleaved. Stimuli are not drawn to scale. (B) Patients' performance is neurotypical. 2-way-ANOVA, * *p*=0.047; ** *p*=0.008; *** p<0.001. Error bars represent normalized SEM. n=28 independent participants.

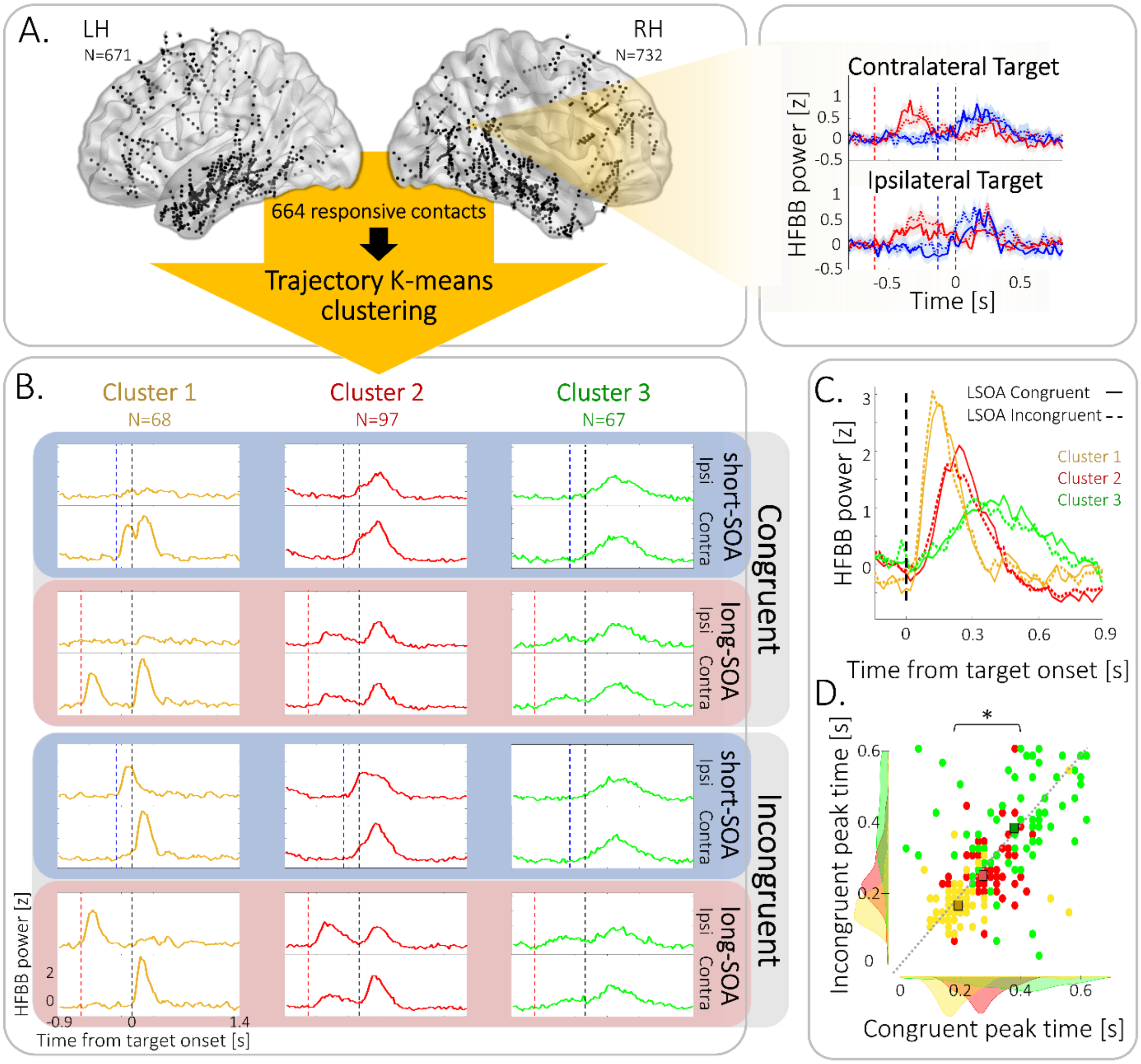

Figure 2 - Contact localization and trajectory clustering. (A) Left: Illustration of the localization in normalized space (MNI152) of the contacts included in the analysis (black circles; n=1,403) in the left hemisphere (LH; n=671) and in the right hemisphere (RH, n=732), pooled across patients. Each localization is the mean coordinates of the two contacts composing the contact's bipolar montage. To reveal prototypical temporal patterns simultaneously across all conditions, the trajectories across the 8 condition dimensions of the mean high-frequency broadband (HFBB) target-locked activity of 664 significantly responsive contacts (significant time-point-by-time-point t-test for at least 100ms in one of the experimental conditions compared to baseline), were clustered using a custom-made trajectory K-means approach. Right: Example of target-locked mean normalized HFBB responses of one contact in the right angular gyrus in Congruent (full lines) and Incongruent (dashed lines) trials, at short-SOA (blue) and long-SOA (red), with targets contralateral or ipsilateral to the contact. Dashed vertical lines represent onsets of target (black), and short-SOA (blue) and long-SOA (red) cues. Shaded areas represent SEM across trials. (B) Prototypical temporal profiles of contact clusters across conditions: Trimmed-mean target-locked activity profiles of three contact clusters, across the 8 conditions (Congruent / Incongruent Trial X short-SOA / long-SOA X Ipsilateral target (Ipsi) / contralateral target (Contra)). Cluster 1 (yellow) shows contralateral fast responses, with cue-target activity segregation at both SOAs; Cluster 2 (red) shows bilateral slower responses with spatial sensitivity, with cue-target activity segregation at long-SOA but response integration in short-SOA; and Cluster 3 (green) shows bilateral slowest responses with stimulus-type sensitivity, with cue-target activity segregation at long-SOA but response integration at short-SOA. Dashed vertical lines represent target onset (black) and cue onset at short-SOA (blue) and long-SOA (red). (C) Temporal gradient of target-locked activity (trimmed-mean) of the three clusters. Black dashed line depicts target onset. (D) Scatter plot of peak times of mean target-locked activity of contacts of Cluster 1 (yellow circles),

Cluster 2 (red circles) and Cluster 3 (green circles), in Congruent (x-axis) and Incongruent (y-axis) conditions, showing a significant temporal gradient (Mixed 2-way ANOVA, Cluster main effect $p<0.001$, $\eta^2=0.378$; linear polynomial contrast: $p\leq0.001$). Squares represent mean peak time; Dotted grey line denotes the equity line; Shaded areas represent peak time distributions.

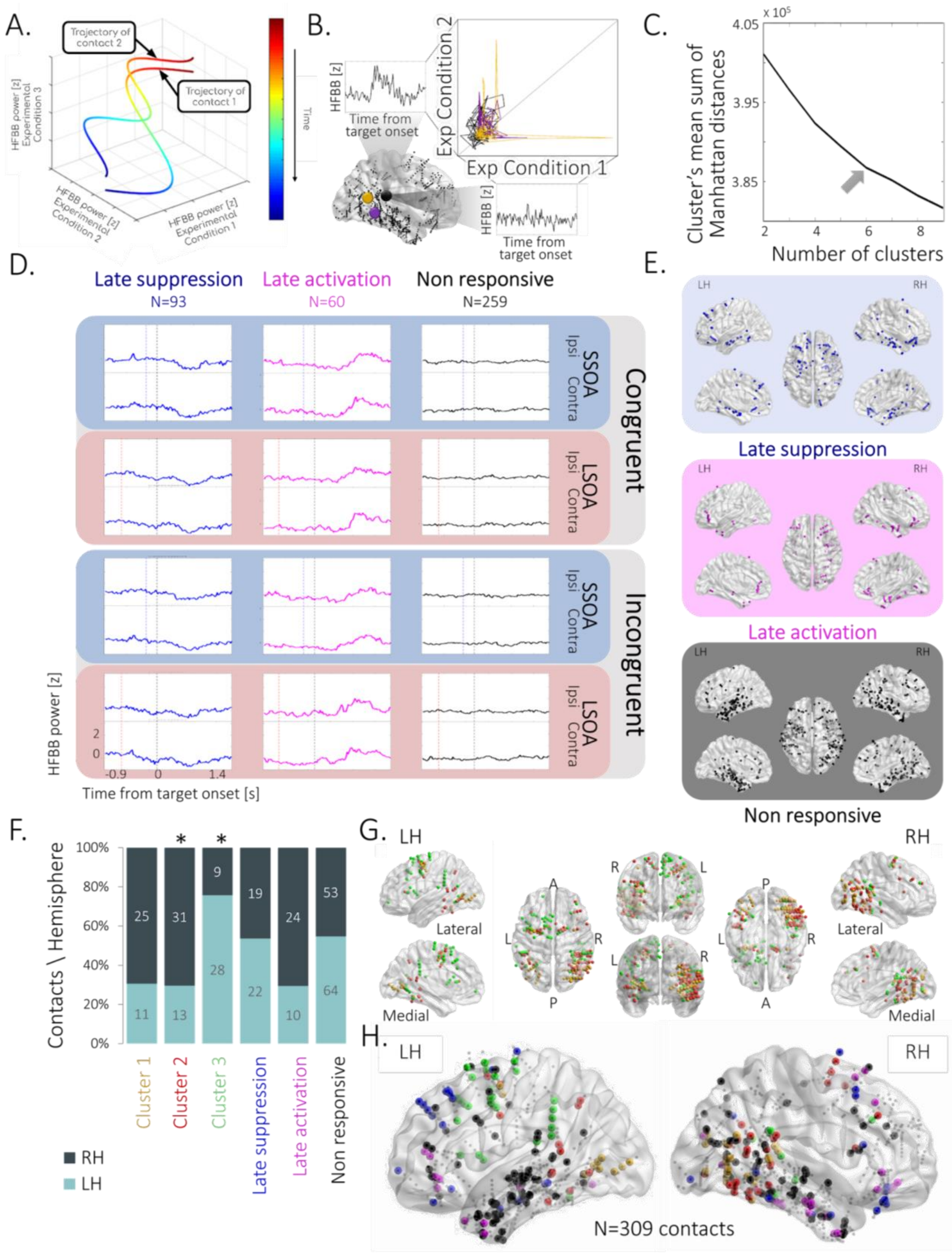

Figure S2 – Clusters' spatiotemporal profile. (A) A schematic illustration of two trajectories of contact neural activity in a multi-dimensional experimental condition space (3-dimensional for visualization simplicity). The temporal order of the sampled neural activity, composing the illustrated contact trajectories, is color-coded (red to blue). The dimensions of the 3-D space correspond to the three experimental conditions, such that the trajectories represent the contacts' neural activity measured as HFBB power in all three experimental conditions simultaneously. (B) A simplified example transformation of HFBB time series traces of a contact (black) in two experimental conditions into a neural activity trajectory in a 2-dimensional experimental condition space, represented along with the trajectories of two other contacts (yellow & purple). Contact locations in the brain are depicted in the lower left inset (black, yellow & purple circles). (C) Elbow method. Mean sum of Manhattan distances between each contact trajectory and its assigned cluster trajectory for 2-9 clusters' solution. Maximal elbow (grey arrow) is observed at the 6-cluster solution. (D) Prototypical activity profiles of contact clusters not included in the main analysis: Trimmed-mean target-locked activity profiles of Late suppression cluster (blue); Late activation cluster (magenta); Non responsive cluster (black), across the 8 conditions (Congruent / Incongruent X short-SOA / long-SOA X Ipsilateral target (Ipsi) / contralateral target (Contra)). Dashed vertical lines represent Target onset (black) and Cue onset at short-SOA (blue) and long-SOA (red) conditions.(E) Spatial profile of clusters not included in the main analysis. Illustration of the localization of the contacts composing each cluster: Late suppression cluster (blue); Late activation cluster (magenta); Non responsive cluster (black). Note that the Non responsive cluster contained contacts whose responses were probably idiosyncratic or induced (as opposed to evoked) and therefore were averaged out in the cluster centroid trajectory. For each cluster, dots represent contacts' localization, computed as the mean coordinates of the two contacts composing each contact's bipolar montage, depicted in normalized space (MNI152) in dorsal (middle), lateral (top) and medial (bottom) views in the right hemisphere (RH; right) and the left hemisphere (LH; left). (G) Relative localization of contacts of clusters 1, 2 & 3 (yellow, red & green; correspondingly) visualized from different views. (F) Clusters' spatial distribution in symmetrically covered regions significantly differs between right and left hemispheres (dark grey & light grey respectively; $\chi^2_{(5)}=29.09$, $p<0.001$), resulting from a significant right lateralization of Cluster 2 (red) and a significant left lateralization of Cluster 3 (green; post hoc binomial tests, $p=0.01$ and $p=0.003$; See Supplementary Results). (H) Symmetrically covered regions were defined by calculating the overlap between the volumes of 3mm radius spheres around each contact for each hemisphere (See Supplementary Results and Methods sections). Proportion of colors in each bar represents the percentage of contacts per hemisphere in each cluster; numbers are the raw contact number per hemisphere in each cluster.

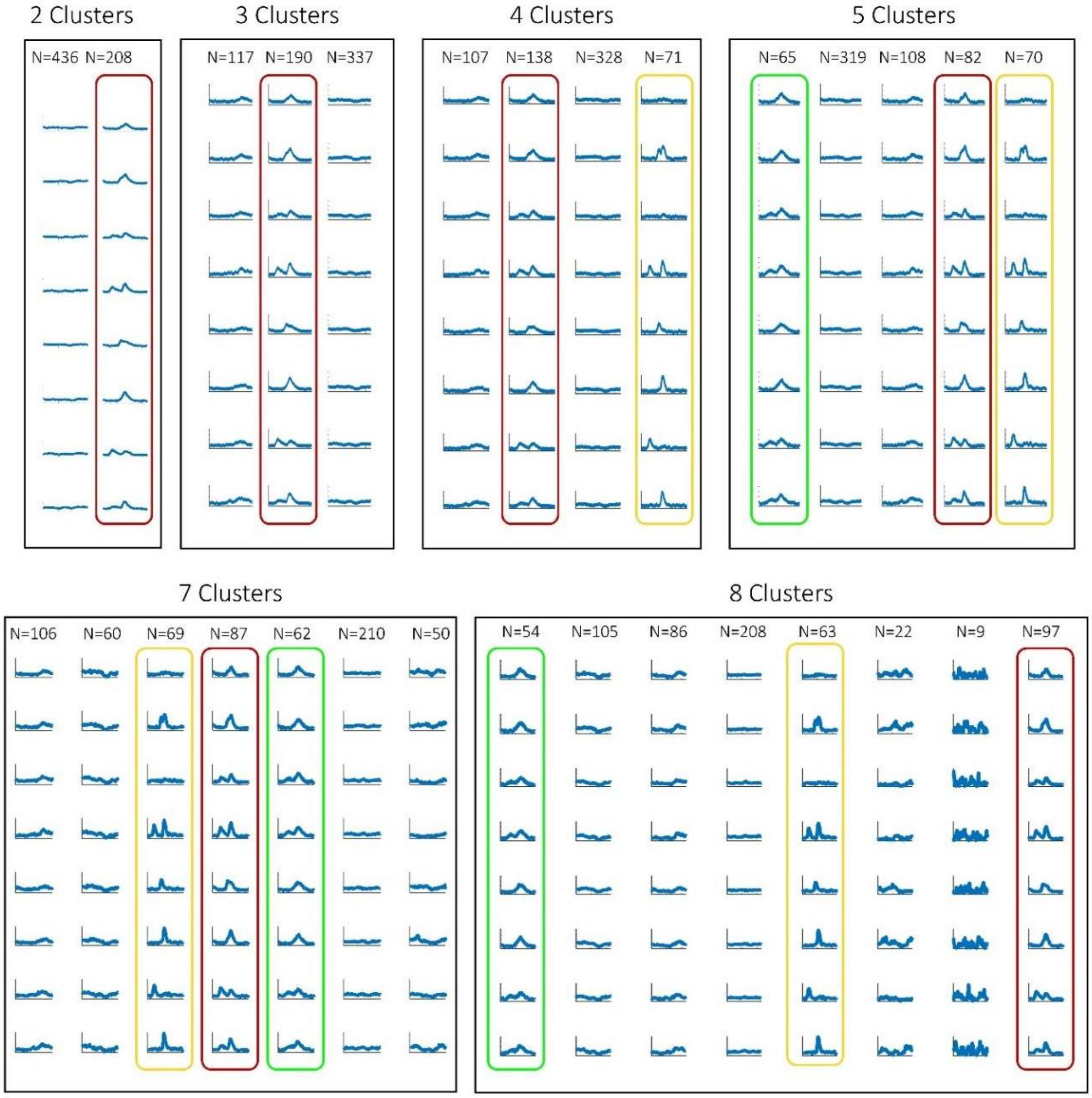

Figure S3 – Trajectory k-means solution for different number of clusters. The three target-locked clusters analyzed in this study: The Cluster 1 (yellow), the Cluster 2 (red) and the Cluster 3 (green) are present from 5-cluster solution onward, based on a contingency tables analysis showing a significant strong correspondence between each of the k-solutions and the 6-cluster solution (see Table S1 for details).

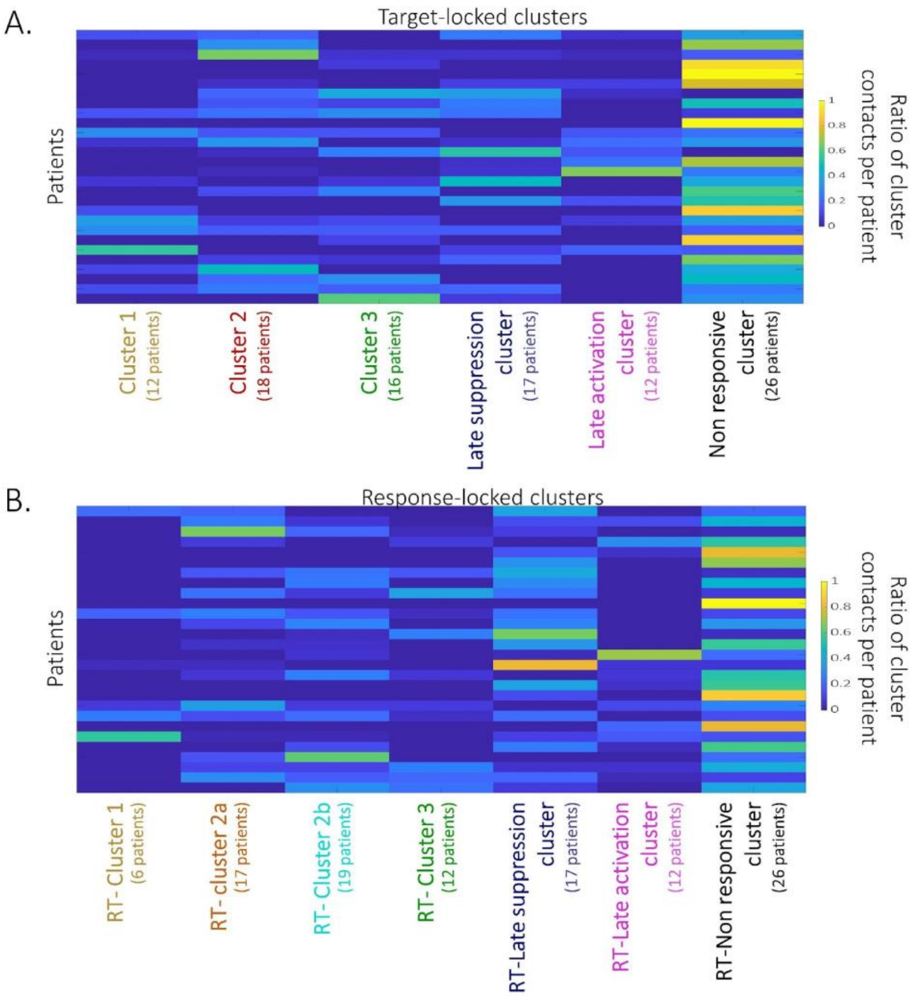

Figure S4 – Distribution of the cluster contacts within participants. (A) The distribution of participants' contributions to target-locked clusters. (B) The distribution of participants' contributions to response-locked clusters. Each row represents one participant. Color code denotes the ratio of contacts in each cluster per participant.

Out of the chosen 6-cluster solution (Fig. 2A-B, S2C-E), we focused on three clusters of contacts who were stable across different k-solutions and whose activity patterns changed across the experimental conditions (Fig. 2B) and were positively correlated to one another, whereas their correlation with the other three clusters was negative or near zero, indicating that these clusters form a distinct group (Fig. S5).

The first cluster (Cluster 1; 68 contacts from 12 patients; Fig. 2B left, S4) showed early responses only to contralateral cues and targets. A second cluster (Cluster 2; 97 contacts from 18 patients; Fig. 2B middle) showed later ipsilateral and contralateral responses, with stronger responses to contralateral stimuli, demonstrating the spatial sensitivity of this cluster. The third cluster (Cluster 3; 67 contacts from 16 patients; Fig. 2B right) was the last to react, with stronger responses to bilateral targets than to cues, hence suggesting a sensitivity to task-relevance. Importantly, the response in Clusters 2 and 3 was sensitive to the cue-target delay. For the short-SOA, cue and target responses summed together, but they were segregated for the long-SOA. Activity in the three remaining clusters did not seem to vary across experimental conditions, with one cluster showing late inhibition, one showing late activation and one showing no prototypical response (see Fig. S2D).

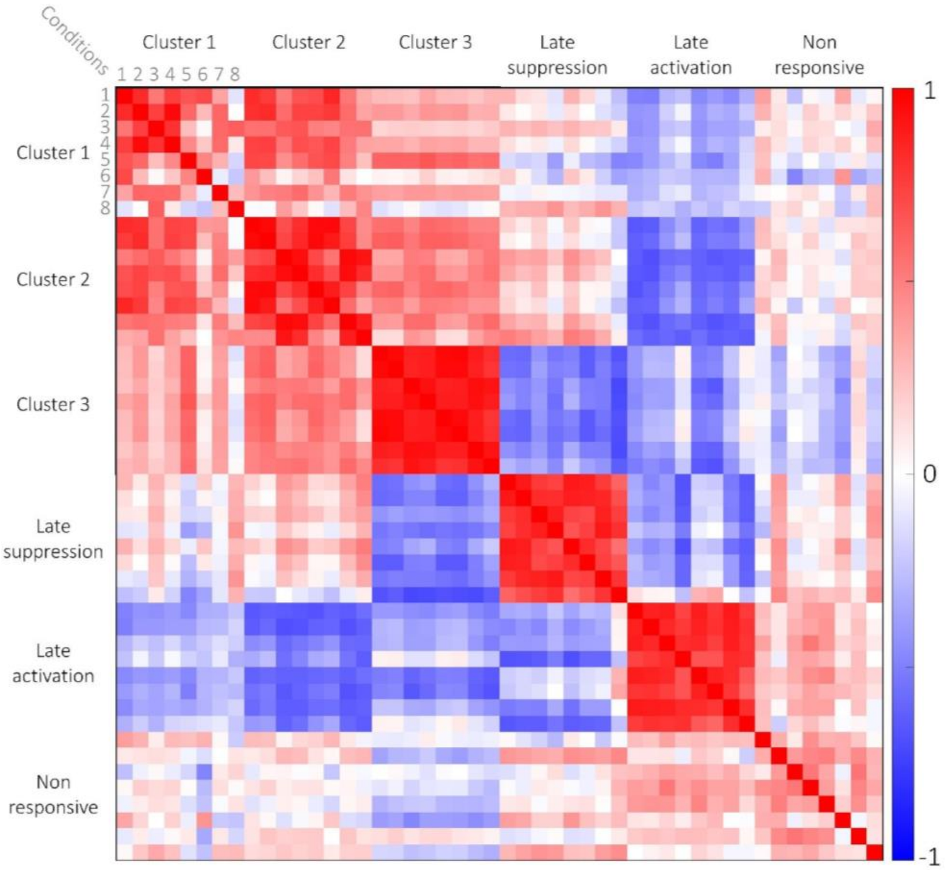

Figure S5 – Clusters 1, 2 & 3 form a distinct group among all clusters. Pearson correlations between condition centroid time-series across target-locked clusters reveal that the correlations of – Clusters 1, 2 & 3 vary across experimental conditions within each cluster and positively correlate between these clusters. The correlation pattern within the three other clusters is more uniform, and negatively correlated across clusters. Color bar represents the r coefficient (negative correlation – blue; positive correlation-red); Numbers correspond to the experimental conditions (1- Contralateral target short-SOA Congruent; 2- Contralateral target short-SOA Incongruent; 3-'Contralateral target long-SOA Congruent; 4-Contralateral long-SOA Incongruent; 5-Ipsilateral target short-SOA Congruent; 6-Ipsilateral target short-SOA Incongruent; 7-Ipsilateral target long-SOA Congruent; 8-Ipsilateral target long-SOA Incongruent).

Next, we examined the temporal relationships between the clusters. The three target-locked clusters formed a temporal gradient (Fig. 2C-D). The earliest activity emerged at Cluster 1, which peaked around 182±78ms post-target. Then followed Cluster 2 (262±75ms post-target), and finally Cluster 3 (383±141ms post-target; (Mixed 2-way ANOVA with Cluster and Congruence as factors; Cluster main effect $F(2,229)=102.7$, $p<0.001$, $\eta^2=0.378$; linear polynomial contrast: $p\leq0.001$).

Having established a neural latency gradient between the three clusters, we then examined the spatial relationships between the clusters. Notably, the clustering was blind to the localization of the contacts. We thus hypothesized that meaningful clusters will tend to group anatomically. Cluster 1 mainly consisted of contacts in the bilateral occipitotemporal cortex and in the prefrontal cortex, around the FEF (Fig. 3A top, S2G and Movie S1), consistently with its visual-like responses. Cluster 2 contacts were mainly in the caudal portion of the TPJ, around the angular gyrus, posterior temporal cortex and prefrontal cortex (Fig. 3A middle, S2G and Movie S1). The cluster was lateralized to the right hemisphere (See Supplementary Results and Fig. S2F, H). Cluster 3 was located mainly in the rostral TPJ region (around the supramarginal gyrus), posterior temporal cortex and prefrontal cortex (Fig. 3A bottom, S2G and Movie S1), and was lateralized to the left hemisphere (See Supplementary Results and Fig. S2F). Notably, the two latter clusters divided between them portions of known frontoparietal attention networks [19,56].

We next asked if the contacts within each cluster were structurally connected. We divided each cluster's contacts into pre rolandic contacts, located in the occipital, parietal and temporal lobes, and post rolandic contacts, located in the frontal lobe, using the central sulcus as a landmark. A fiber tracking analysis paired with probability maps in 176 healthy individuals from the Human Connectome Project database [57] revealed that white matter tracts significantly connected pre-rolandic and post-rolandic contacts in the three clusters, suggesting these clusters' long-range contacts formed structural networks (Fig. 3D; threshold-free cluster enhancement-based non-parametric t-test, p<0.05). We then examined the overlap of the connecting pre and post rolandic fibers with the three branches of the superior longitudinal fasciculus (SLF I; SLF II; SLF II), which connect the ventral and dorsal attention networks [19,35,58,59]. A probability cut-off of 50% was used for the SLF maps and the resulting overlap was normalized to the number of cluster contacts per hemisphere. In Cluster 1, the connecting tracts mainly overlapped with SLF II in both hemispheres (Left hemisphere: SLF II 76.98%, SLF I 22.31%, SLF III 7.22%; Right hemisphere: SLF II 96.80%, SLF I 23.03%, SLF III 2.56%). In the right hemisphere of the right-lateralized Cluster 2 there was a major overlap with SLF II, a smaller overlap with SLF III, and a minimal overlap with SLF I (SLF II 45.67%; SLF III 23.80%; SLF I 3.05%). An opposite pattern was found in the left hemisphere, where tracts overlapped with SLF III and had a smaller overlap with SLF II (SLF III 43.35%, SLF II 35.11%, SLF I 0.03%). In the left-lateralized Cluster 3, connecting tract in the left hemisphere overlapped mainly with SLF III and had a small overlap with SLF II and a minimal overlap with SLF I (SLF III 36.78%; SLF II 28.45%; SLF I 0.65%). In the right hemisphere, Cluster 3 fibers were mainly associated with the SLF II and only minimally overlapped with SLF III and SLF I (SLF II 53.66%; SLF III 4.96%; SLF I 9.50%). These results suggest that the functional clusters identified solely based on their temporal responses, correspond to well-defined structural networks.

We further asked if the clusters' anatomical localizations were ordered across large-scale cortical organization. We therefore explored how cluster localizations relate to the cortical gradient [49]. The position of a region along the gradient reflects its anatomical and functional cortical features [49,50], and can be described using a 2-dimensional coordinate system that represents location along the early sensory and motor Periphery to the high-level multisensory Core [51]. Two main components define this 2-dimensional coordinate system: Dimension 1 extends from primary unimodal to transmodal regions, and Dimension 2 separates somatomotor and auditory cortices from visual cortex [51]. Cluster 1 contacts were the most peripheral and closest to the visual end of Dimension 2; contacts in the Cluster 3 were the closest to the core, extending from the somatomotor end to transmodal regions (Dimension 1 electrode values: 1-way ANOVA: $F(2,229)=7.74$; $p<0.001$, $\eta^2=0.06$; linear polynomial contrast: $p\leq0.001$; Dimension 2 electrode values: 1-way ANOVA: $F(2,229)=77.79$; $p<0.001$, $\eta^2=0.28$; linear polynomial contrast: $p\leq0.001$; Fig. 3B-C). Thus, the clusters were embedded in the cortical gradient topography, forming a spatiotemporal gradient.

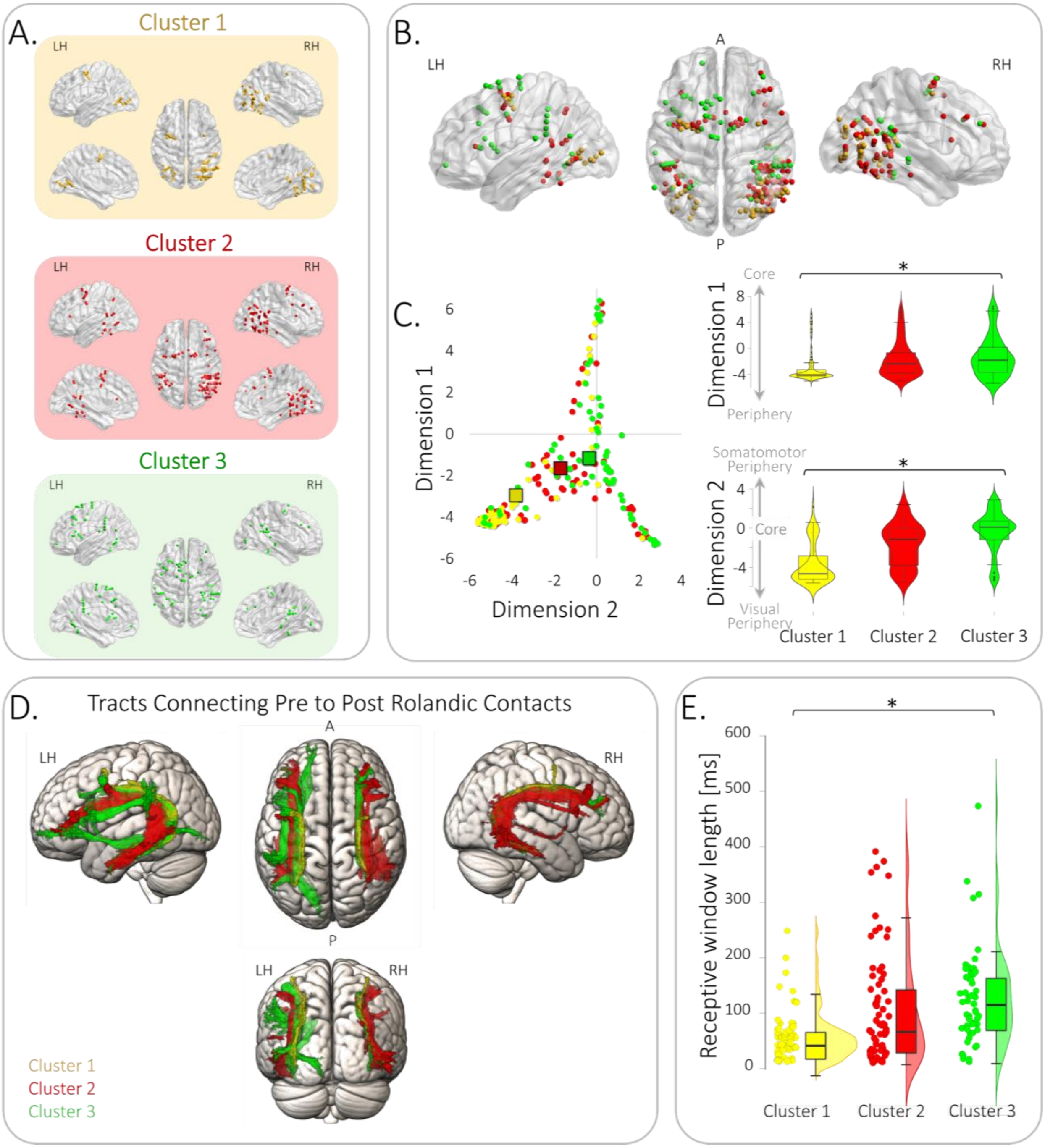

Figure 3 – Clusters exhibit a spatiotemporal gradient. (A) Clusters' spatial profile. Illustration of the localization of the contacts composing each cluster: Cluster 1 (yellow), Cluster 2 (red), Cluster 3 (green). For each cluster, dots represent contacts' localization in dorsal (middle), lateral (top) and medial (bottom) views of the right hemisphere (RH; right) and of the left hemisphere (LH; left). (B) Core-Periphery gradient: Clusters' anatomical localization follows Core-Periphery gradients [51], where the Cluster 1's contacts are the most peripheral and the Cluster 3's contacts are closest to core regions. (C) Left: Scatter plot of contacts localization along core-periphery gradients (Cluster 1 - yellow circles, n=62 independent contacts; Cluster 2 - red circles, n=97 independent contacts; Cluster 3 – green circles, n=67 independent contacts; rectangles represent clusters' mean). Right: Violin plots of contacts localization along Core-Periphery gradients for Cluster 1 (yellow), Cluster 2 (red) and Cluster 3 (green), showing a significant core-periphery gradient (Gradient 1: 1-way ANOVA, $p<0.001$, $\eta^2=0.06$; linear polynomial contrast: $p\leq0.001$; Gradient 2: 1-way ANOVA, $p<0.001$, $\eta^2=0.28$; linear polynomial contrast: $p\leq0.001$; n=232 independent contacts in total). The box centerlines depict the medians, the bounds of the box depict the 75%/25% quartiles and the whiskers depict the top & bottom 25% percentiles. (D)

Cluster contacts are structurally connected: Corrected tractography t-maps, showing the significant white matter voxels, which connect pre and post rolandic contacts within each cluster (Cluster 1 – yellow; Cluster 2 - red, Cluster 3 - green), derived from a fiber tracking analysis of 176 healthy individuals. (E) Contacts' receptive windows lengthen along the cluster gradient: Raincloud plots of individual contacts' receptive window length (circles), showing a significant linear lengthening from Cluster 1 (yellow, n=62 independent contacts), to Cluster 2 (red, n=97 independent contacts), to Cluster 3 (green, n=67 independent contacts; 1-way ANOVA*:* $p<0.001$, $\eta^2=0.11$; linear polynomial contrast: $p\leq0.001$; n=232 independent contacts in total). The box centerlines depict the medians, the bounds of the box depict the 75%/25% quartiles and the whiskers depict the top & bottom 25% percentiles.

We then went on to study the way neural activity in the cluster gradient relates to attentional, visual and response aspects of the Posner task. We first explored how our experimental manipulation of attentional events influenced the clusters' target-locked neural activity. Specifically, we examined the neural correlates of the behaviorally significant IOR effect, by comparing long-SOA Congruent and Incongruent trials in the cue time-window (-600-0ms) and in the target time-window (0-800ms; time-resolved 3-way ANOVA with Congruence, Target Laterality and Contact Hemisphere as factors; Fig. 4, See Tables S1 & S2 for full results).

In the cue time-window, Congruent and Incongruent trials did not significantly differ overall (no significant main Congruence effect; Fig. S6), reflecting the fact that the cue location did not predict the congruence of the upcoming target. Instead, there were mainly neural effects reflecting the differential lateralization of cues preceding Congruent and Incongruent targets (See Supplementary material).

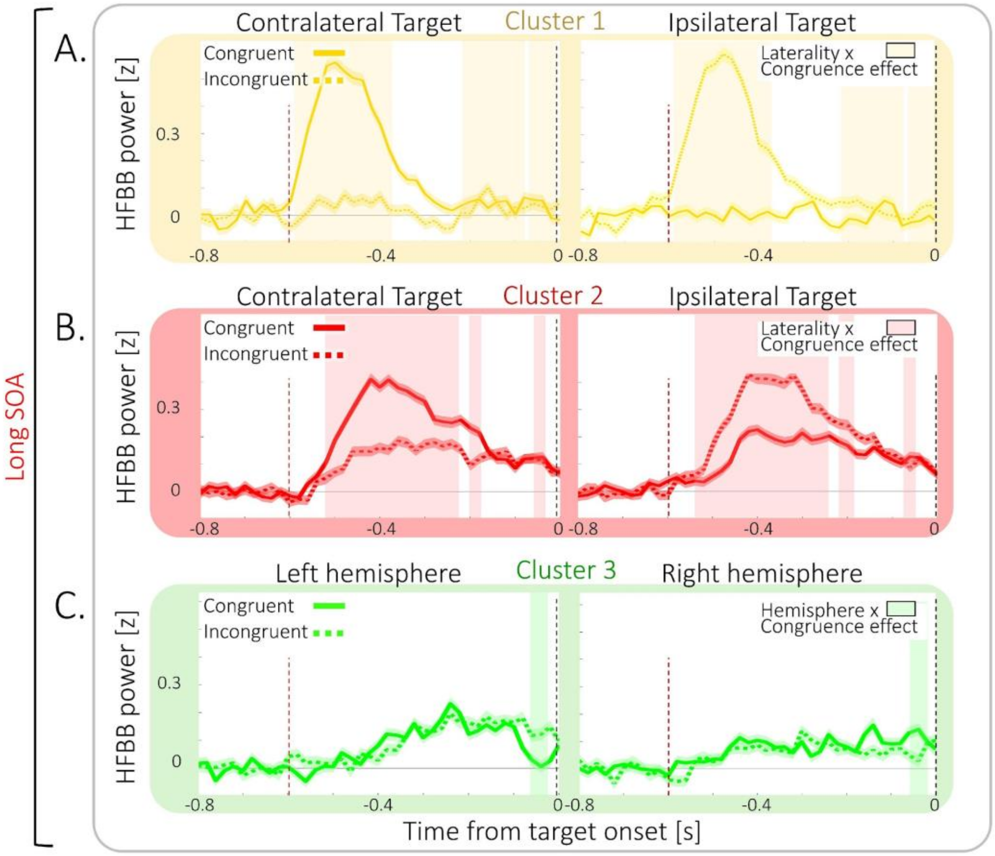

Figure S6 – Congruence-related neural activity in the Cue time-window. Mean target-locked long-SOA activity in Cluster 1 (yellow), Cluster 2 (red) and Cluster 3 (green), computed over trials pooled across all cluster contacts, for Congruent trials (full lines) and Incongruent trials (dashed lines) in the long-SOA. (A) In Cluster 1 a significant Laterality x Target-congruence effect was observed (yellow shaded area; largest *p*=0.018) showing it responds only to contralateral cues. (B) In Cluster 2 responses were stronger to contralateral cues than to ipsilateral ones, as shown by a significant Laterality x Target-congruence effect (shaded red areas; largest *p*=0.038). (C) Cluster 3 showed a significant Hemisphere x Target-congruence (green shaded area; largest *p*=0.045). (A)-(C) Shaded areas around traces depict SEM; Dashed vertical lines represent Target onset (black) and Cue onset (red).

In the target time-window, cluster 2 showed a Congruence main effect at the offset of the target-related activity (240-300ms post target; largest *p*=0.002; see Fig. 4D for examples of single contacts). Moreover, in the contacts of this cluster in the right hemisphere, the response peaked 22ms later in the Congruent than in the Incongruent trials (140-220ms post target onset; Hemisphere x Congruence interaction: largest *p*=0.03; post hoc tests: largest *p*=0.014), mirroring behavioral IOR. There were no congruence effects in Cluster 1 (Fig. 4A) and in Cluster 3 there was only a late Congruence effect at 660-680ms post-target (largest *p*=0.003). Therefore, IOR-related activity was mainly restricted to the Cluster 2, thus attentional events corresponded to the neural dynamics of this cluster.

Despite the lack of a significant behavioral effect of RT facilitation, the effect might be masked by other processes, as is often the case [6,8,11]. Current theories postulate that even when masked, the facilitation effect nevertheless exists [6,8,11]. We therefore performed an exploratory time-resolved ANOVA analysis with the factors Congruence, Target-side and Hemisphere, to test the attentional neural effect in Cluster 2 also in the short-SOA. In the target time-window, cluster 2 showed a significant Congruence X Target-side interaction effect (-60-140ms post target; largest *p*=0.022) and a main Target-side effect (160-300ms; 320-360ms; 440-460ms post Target onset; largest *p*=0.012; see Fig. S7). This reflects a combination of stronger responses for contralateral stimuli (Cue or Target) which are summed together, leading to a faster and stronger activation for contralateral congruent compared to contralateral incongruent cues and targets, and compared to ipsilateral ones. This differential summed activity translates to a neural preference for stimuli repeating in the same specific spatial (contralateral) location, dovetailing the behavioral RT facilitation effect, in which RT is faster for repeated stimuli in a specific location.

The observed differences between SOA and Congruence conditions across clusters could be explained by different theta phases at target onset, as the neural activity at the short-SOA and Long-SOA could fall into opposite phase bins. A control mixed ANOVA analysis revealed that theta phase could not explain these effects, either across the entire sample of contacts or when looking at particular clusters of contacts (See Supplementary Results). A Bayesian ANOVA with confirmed these negative findings, which are consistent with a recent paper that found no evidence for rhythmic sampling in inhibition of return behavioural effects [60].

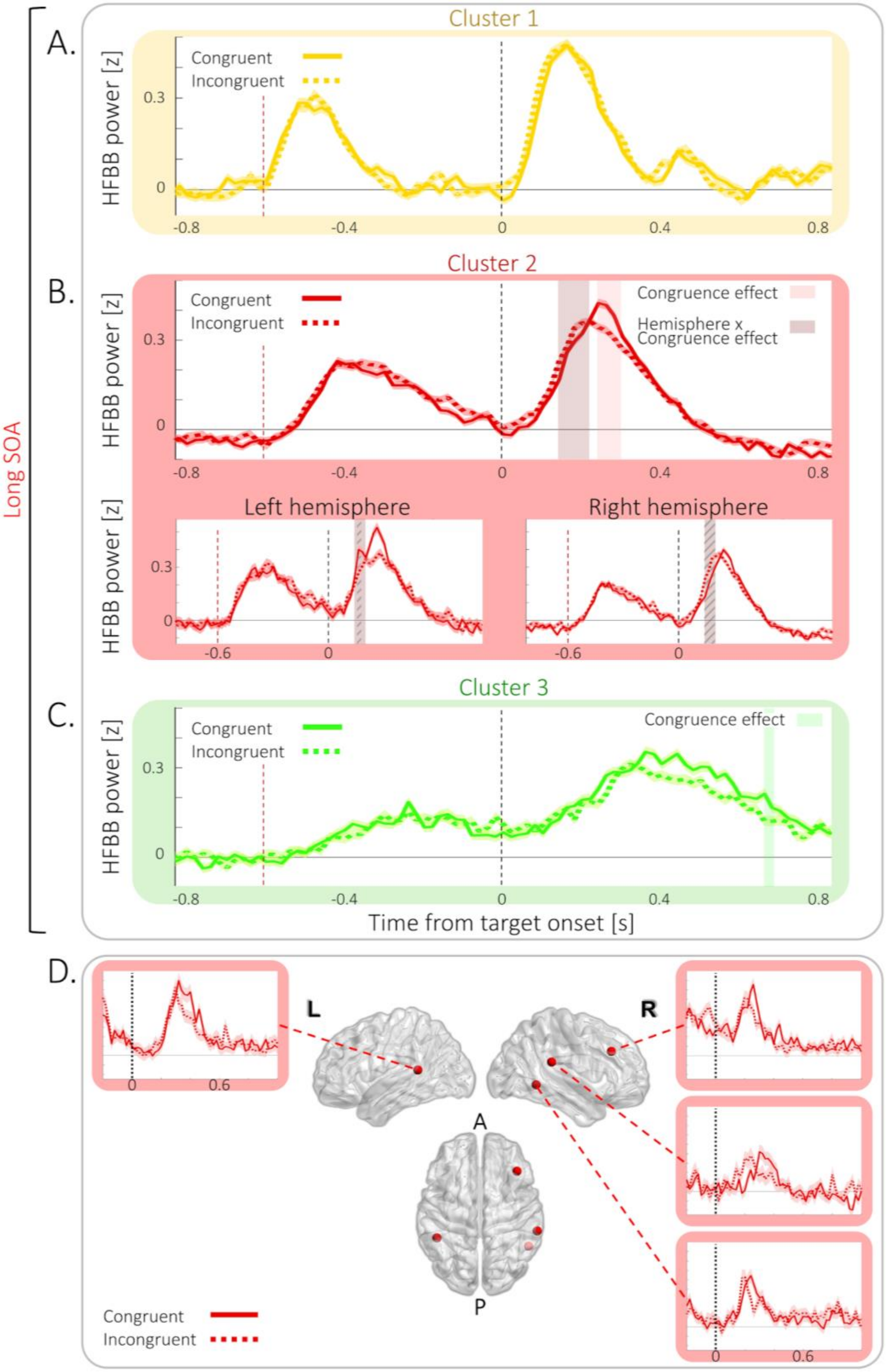

Figure 4 - IOR-related neural activity. Mean target-locked long-SOA activity in Cluster 1 (yellow), Cluster 2 (red) and Cluster 3 (green), computed over trials pooled across all cluster contacts, for Congruent trials (full lines) and Incongruent trials (dashed lines). (A) In the Cluster 1, no significant Congruence effect was observed in a 3-way ANOVA with Holm multiple comparisons correction. (B) In Cluster 2 activity in Congruent and Incongruent trials (IOR-related) differed significantly in a 3-way ANOVA with Holm multiple

comparisons correction at 0.24-0.3s post target (shaded red areas; Congruence main effect: largest *p*=0.002), and a significant hemispheric difference between IOR-related responses was observed at 0.14-.022s post target (shaded brown area; Hemisphere x Congruence interaction: largest *p*=0.03; Diagonally striped areas represent significant Congruence x Hemisphere post hoc comparisons (*p*<0.05)). (C) In Cluster 3 activity in Congruent and Incongruent trials differed significantly in a 3-way ANOVA with Holm multiple comparisons correction at 0.66-0.68s post target (green shaded area; Congruence main effect: largest *p*=0.003). A-C. Shaded areas around traces depict SEM; Dashed vertical lines represent Target onset (black) and Cue onset (red) at the long-SOA Condition. (D) Representative examples of HFBB power IOR-related activity in the Congruent (full line) & Incongruent (dashed line) long-SOA conditions of individual contacts of the Cluster 2, shaded areas around traces depict SEM. p values are Holm corrected.

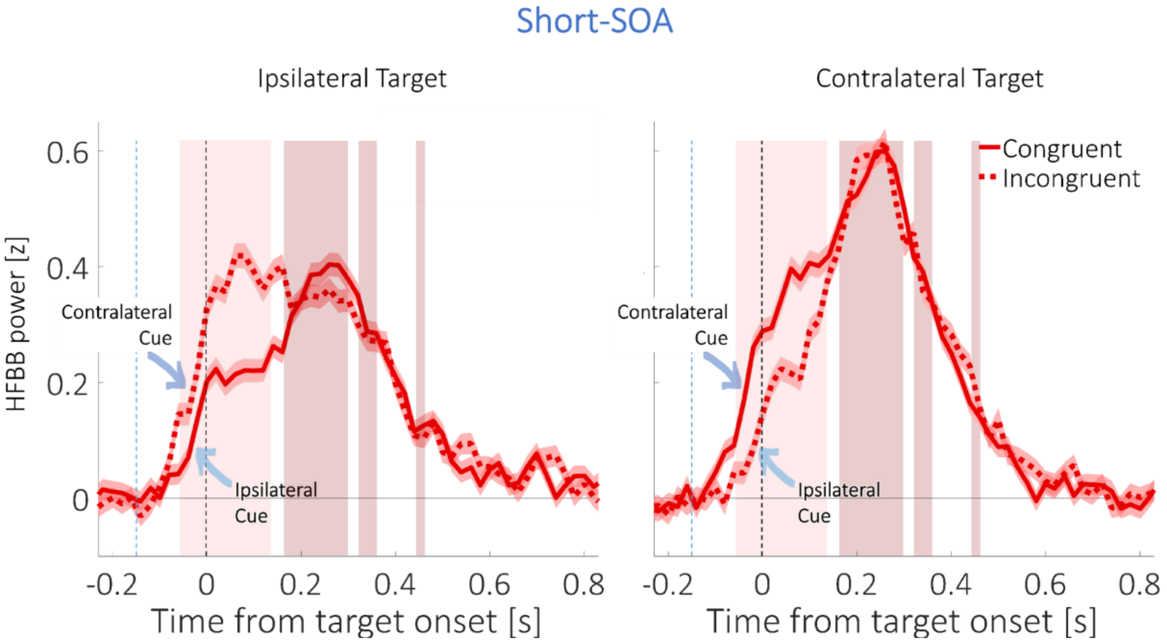

Figure S7 – Exploratory analysis of short-SOA congruence-related neural activity in the target time-window in Cluster 2. Mean target-locked short-SOA activity in Cluster 2 (red), computed over trials pooled across all cluster contacts, for Congruent trials (full lines) and Incongruent trials (dashed lines), when targets were ipsilateral (left) or contralateral to the recording contact (right). Note, that when targets were ipsilateral, Incongruent cues were contralateral (dark blue arrow), and Congruent cues were ipsilateral (light blue arrow), and conversely for contralateral targets. Responses were stronger to contralateral cues and targets than to ipsilateral ones, as shown by a significant Target-side x Congruence effect (shaded light red areas; -60-140ms post Target onset; largest *p*=0.022) and a main Target-side effect (shaded dark red areas; 160-300ms; 320-360ms; 440-460ms post Target onset; largest *p*=0.012). Shaded areas around traces depict SEM; Dashed vertical lines represent Target onset (black) and Cue onset (blue).

How do these clusters of neural activity relate to the manual response? We examined whether cluster neural dynamics relate to motor response timing, across experimental conditions, reflecting the significant RT differences between SOAs in the Congruent and Incongruent conditions. In each cluster, we divided the trials (pooled across conditions) into 20 quantiles according to their RT (Fig. 5A), and tested the relation of RT-bins with the neural activity using a time-resolved 1-way repeated measures ANOVA (See Fig. 5A-B for results and examples of single contacts). In Cluster 2, the offset of the target-related activity differed across RT bins (300-560ms post target; largest *p*=0.028), with a faster decay at faster RT-bins, just before the motor response. In Cluster 3, a RT-bin effect occurred around the peak of target-related activity and button-press time (280-300 and 400-420ms post target; largest *p*=0.007). In Cluster 1, a RT-bin effect occurred at 500-540 and 560-680ms post target onset (*p*<0.002), suggesting a RT-related late modulation after response offset and button press time. RT-related target-locked activity in Clusters 2 and 3 was confirmed by cross-correlation analysis (See Supplementary Results and Fig. S9), which revealed that only in these clusters, did the temporal dynamics of neural activity shift according to RTs, and that this shift correlated with RTs. Thus, neural activity in Clusters 2 and 3 was related to the timing of the upcoming motor response, reflecting the behavioral outcome of the task and its associated neural processes.

We next studied the neural correlates of the visual aspects of the Posner task, by adopting a complementary approach and examining visual modulation of response-locked activity. To avoid biases, we applied the trajectory k-means clustering analysis to response-locked activity (Fig. S10 A-C and Movie S2) instead of using the clusters obtained based on the Target-locked activity. To map the correspondence of the seven response-locked clusters to the previously identified target-locked clusters, we performed a contingency analysis that revealed four corresponding response-locked clusters ($\chi^2_{(30)}$=1442; *p* <0.001; Contingency coefficient 0.83; Fig. 5 and S10D). Specifically, this locking-activity to the response further separated the clusters: RT-Cluster 1 (46 contacts; 60.3% of target-locked Cluster 1), RT-Cluster 2a (85 contacts; 35.3% of target-locked Cluster 1 and 49.5% Cluster 2), RT-Cluster 2b (79 contacts; 46.4% of target-locked cluster 1 and 31.3% of Cluster 2), and RT-Cluster 3 (39 contacts; 50.7% of target-locked Cluster 3). We repeated the RT-binning analysis, as described above (Fig. S8B), and tested the RT-bin effect on the neural activity using a time-resolved 1-way repeated measures ANOVA (See Fig. 5C-D for results and examples of individual contacts). The response-locked clusters showed a spatiotemporal gradient and mapped onto the cortical gradient topography, similarly to the target-locked and response-locked clusters. (Fig. S11). Notably, locking activity to the response allowed separating the peripheral RT-Cluster 2a contacts from the RT-Cluster 2b contacts, which were closer to the core (Fig. S11D). Because RT is defined as the time from target onset to the response, this procedure sorted the response-locked trials according to target onset, and thus could unveil visual modulation of response-locked activity. The onset of the response-locked activity was modulated by target onset only in RT-Cluster 1 (120-100ms pre-response; largest *p*=0.04) and RT-Cluster 2a (700-680ms, 520-500ms, 300-200ms pre-response; largest *p*=0.004). In RT-Cluster 2b and RT-Cluster 3, neural activity peak was aligned to the response without significant visual modulation. The visual modulation of response-locked activity in RT-Cluster 1 and RT-Cluster 2a was confirmed by a cross-correlation analysis (See Supplementary Results and Fig. S12), which revealed that only for contralateral targets in these clusters the temporal dynamics of neural activity was shifted according to target-onset and this shift correlated with target-onset time. Thus, response-locked activity revealed that only the clusters with early response-locked activity showed visual modulation, while clusters with later activity were only sensitive to the timing of the motor response.

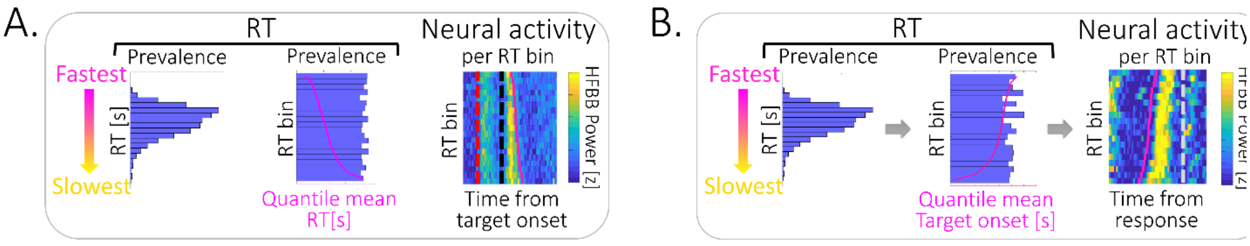

Figure S8 - (A) Computation of neural activity across RT bins: Within each cluster, the trial distribution of RTs across all conditions (left) was divided into 20 quantiles (RT bins; middle), ordered by mean RT (magenta line). The quantile's mean target-locked neural activity pooled across cluster contacts was computed (right; Vertical dashed lines denote cue (red) & target (black) onset; magenta line represent mean RT). (B) Computation of neural response-locked activity across RT bins: Within each cluster, the trial distribution of RTs in each condition (left) was divided into 20 quantiles (RT bins; middle), ordered by mean RT, here corresponding to target onset time (magenta line). The mean Response-locked neural activity across all cluster contacts for each quantile was computed (right; Vertical grey dashed line denote RT (black) onset; magenta line represent mean target onset time).

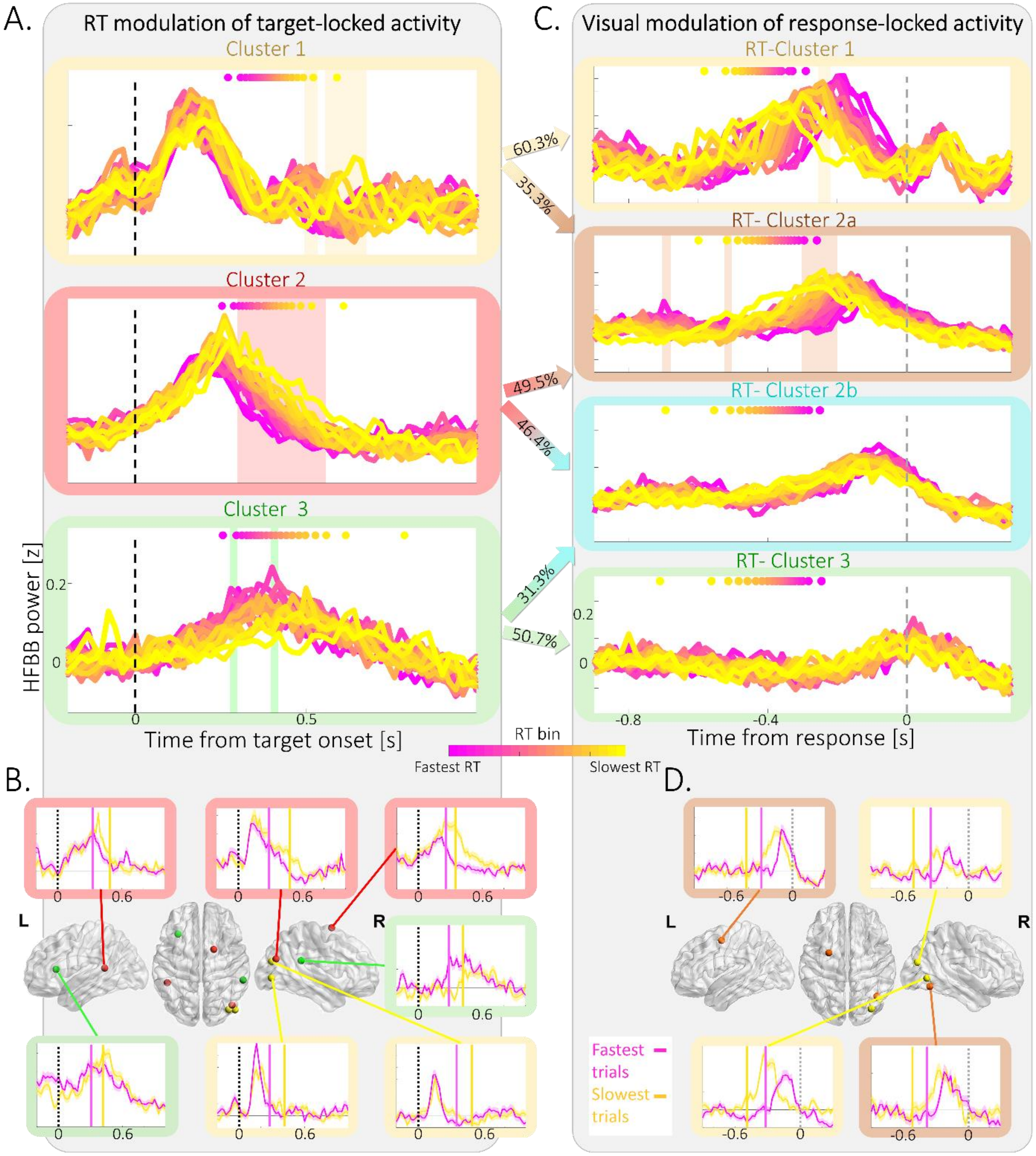

Figure 5 - RT & visual modulation of Target-locked & Response-locked neural activity. (A) RT modulates target-locked neural activity, pooled across conditions and color coded from fastest (Magenta) to slowest (yellow) RT bin. Dashed vertical black line represents target onset; Color-coded dots at the top of each panel represent mean RT for each bin (pink – fastest RT to yellow – slowest RT); 1-way repeated measures ANOVA, Holm multiple comparisons correction. Top: Late RT modulation of activity in Cluster 1 (yellow): Main effect of RT bin at 0.5-0.54 & 0.56-0.68s post-target (shaded yellow area;, largest p=0.002). Middle: RT modulation of neural response offset in Cluster 2 (red): Main effect of RT bin at 0.3-0.56s post target (shaded red area; largest p=0.028). Bottom: RT modulation of response in Cluster 3 (green): Main effect of RT bin at 0.28-0.3 and 0.4-0.42s post target (shaded green area; largest p=0.007). (B) Examples of single contact neural activity in the fastest (pink) & slowest (yellow) thirds of trials for the three target-

locked clusters. Vertical dashed black lines represent target onset; Vertical full lines denote mean RT for fastest (magenta) & slowest (yellow) trials, shaded areas around traces depict SEM. (C) Visual modulation of response-locked neural activity pooled across conditions, color-coded from fastest (Magenta) to slowest (yellow) bin. Dashed vertical grey line represents RT; Color-coded dots at the top of each panel represent mean target onset time for each bin (pink – earliest onset to yellow – latest onset); 1-way repeated measures ANOVA, Holm multiple comparisons correction. Top: Target onset time modulates activity in the RT-Cluster 1 (yellow): Main effect of RT-bin at 0.12-0.10s pre-response (shaded yellow area; largest p=0.04). Target onset time modulates activity in the RT-Cluster 2a (orange): Main effect of RT bin at 0.70-0.68s, 0.52-0.50s & 0.30-0.20s pre-response (shaded orange area; largest p=0.004). No significant modulation in RT-Cluster 2b (turquoise) & RT-Cluster 3 (green). Arrows between panels (A) & (C) denote the contingency between Target-locked & Response-locked clusters (see Fig. S9). (D) Examples of single contact neural activity in the fastest (pink) & slowest (yellow) thirds of trials for RT-Cluster 1 and RT-Cluster 2a. Vertical dashed grey lines represent RT; Vertical full lines denote mean target onset time for fastest (magenta) & slowest (yellow) trials, shaded areas around traces depict SEM. p values are Holm corrected.

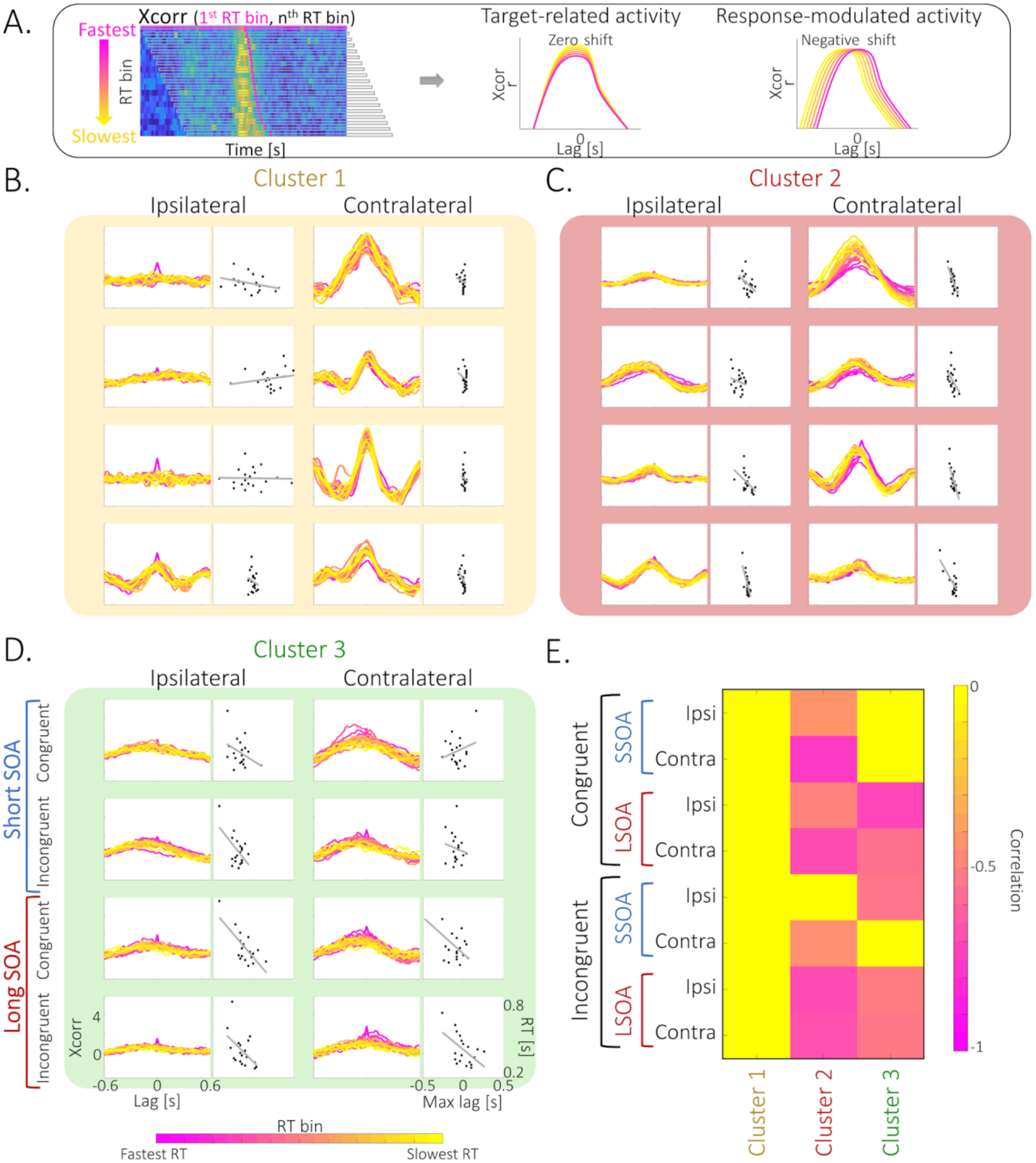

Figure S9 – Cluster neural target-locked activity timing is correlated with behavior. (A) Schematic illustration of the procedure for computing the cross-correlation (Xcorr) of neural activity across RT bins: Cross-correlation between target-locked activity at the fastest RT bin and all subsequent bins was computed (left). If cluster activity is target-associated, maximal cross-correlation will be centered on target onset, resulting in a zero shift across all RT bins (middle). If cluster activity is response-associated, maximal cross-correlation will follow the RT, resulting in a negative shift of cross-correlation lag (right). (B)-(D). Cross-correlogram of neural activity at different RT bins (pink- fastest RT; yellow - slowest RT) as a function of cross-correlation lag (left columns) and Pearson correlation (grey line) between maximal cross-correlation lags (Max lag) and bin's mean RTs (right columns), across the 8 conditions (Congruent / Incongruent X short-SOA / long-SOA X Ipsilateral target / contralateral target) in Cluster 1 (yellow), Cluster 2 (red) and Cluster 3 (green). (B) Cluster 1 activity is target-associated: Cross-correlation plots are centered on zero, especially for contralateral targets. (C) Activity in Cluster 2 is response-associated: Cross-correlation plots show a negative shifted lag that is generally correlated with RT. (D) Cluster 3 activity is response-associated: Cross-correlation plots show a negative shifted lag, correlated with RT under certain conditions. (E) Significant negative correlation between cross-correlation maximal lag and bin mean RT in Clusters 2 & 3: significant ($p<0.05$) negative correlations were found only in these two clusters.

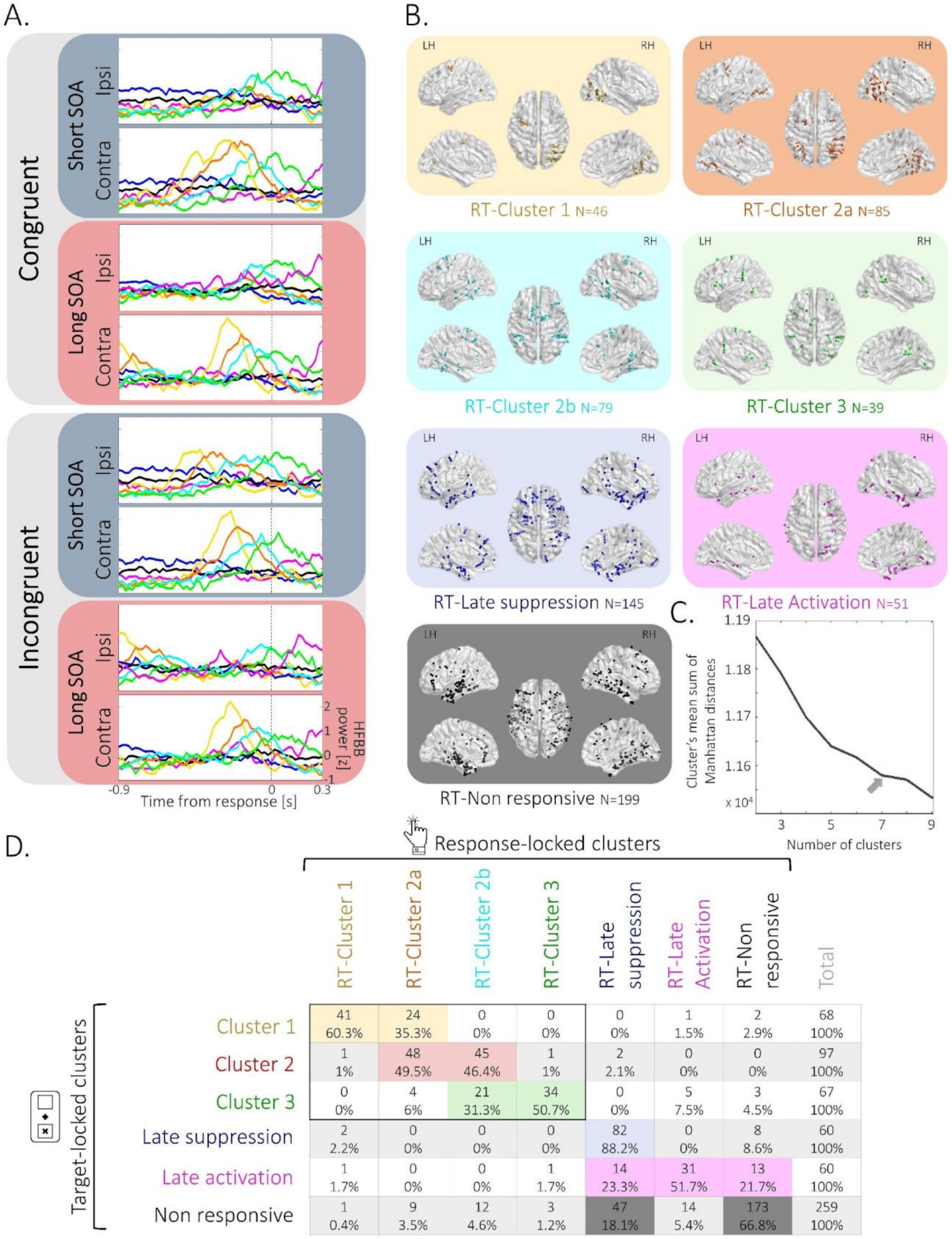

	RT-Cluster 1	RT-Cluster 2a	RT-Cluster 2b	RT-Cluster 3	RT-Late suppression	RT-Late Activation	RT-Non responsive	Total
Cluster 1	41 60.3%	24 35.3%	0 0%	0 0%	0 0%	1 1.5%	2 2.9%	68 100%
Cluster 2	1 1%	48 49.5%	45 46.4%	1 1%	2 2.1%	0 0%	0 0%	97 100%
Cluster 3	0 0%	4 6%	21 31.3%	34 50.7%	0 0%	5 7.5%	3 4.5%	67 100%
Late suppression	2 2.2%	0 0%	0 0%	0 0%	82 88.2%	0 0%	8 8.6%	60 100%
Late activation	1 1.7%	0 0%	0 0%	1 1.7%	14 23.3%	31 51.7%	13 21.7%	60 100%
Non responsive	1 0.4%	9 3.5%	12 4.6%	3 1.2%	47 18.1%	14 5.4%	173 66.8%	259 100%

Figure S10 – Response-locked clusters' spatiotemporal profile. (A) Trimmed-mean Response-locked activity profiles of the seven contact clusters across the 8 conditions (Congruent / Incongruent X short-SOA / long-SOA X Ipsilateral target / contralateral target): RT-Cluster 1 (yellow); RT-Cluster 2a (orange); RT- Cluster 2b (turquoise); RT-Cluster 3 (green); RT-Late suppression cluster (blue); RT-Late activation cluster (magenta); RT-Non responsive cluster (black). Dashed vertical line represents motor response time. (B) Response-locked clusters' spatial location. Illustration of the localization of the contacts composing each cluster (colors as in A). For each cluster, dots represent contacts' localization, computed as the mean coordinates of the two contacts composing each contact's bipolar montage, depicted in normalized space (MNI152) in dorsal (middle), lateral (top) and medial (bottom) views in the right hemisphere (RH) and the left hemisphere (LH). (C) Elbow method. Mean sum of Manhattan distances between each contact trajectory and its assigned cluster trajectory for 2-9 clusters' solution. Maximal elbow (grey arrow) is observed at 7-cluster solution. (D) Contingency tables analysis showing the mapping between target-locked and response-locked clusters. The distribution of target-locked clusters' contacts (rows; number of contacts & % within row) across the different response-locked clusters (columns) was significantly different than chance (*p*<0.001; Contingency coefficient =0.83).

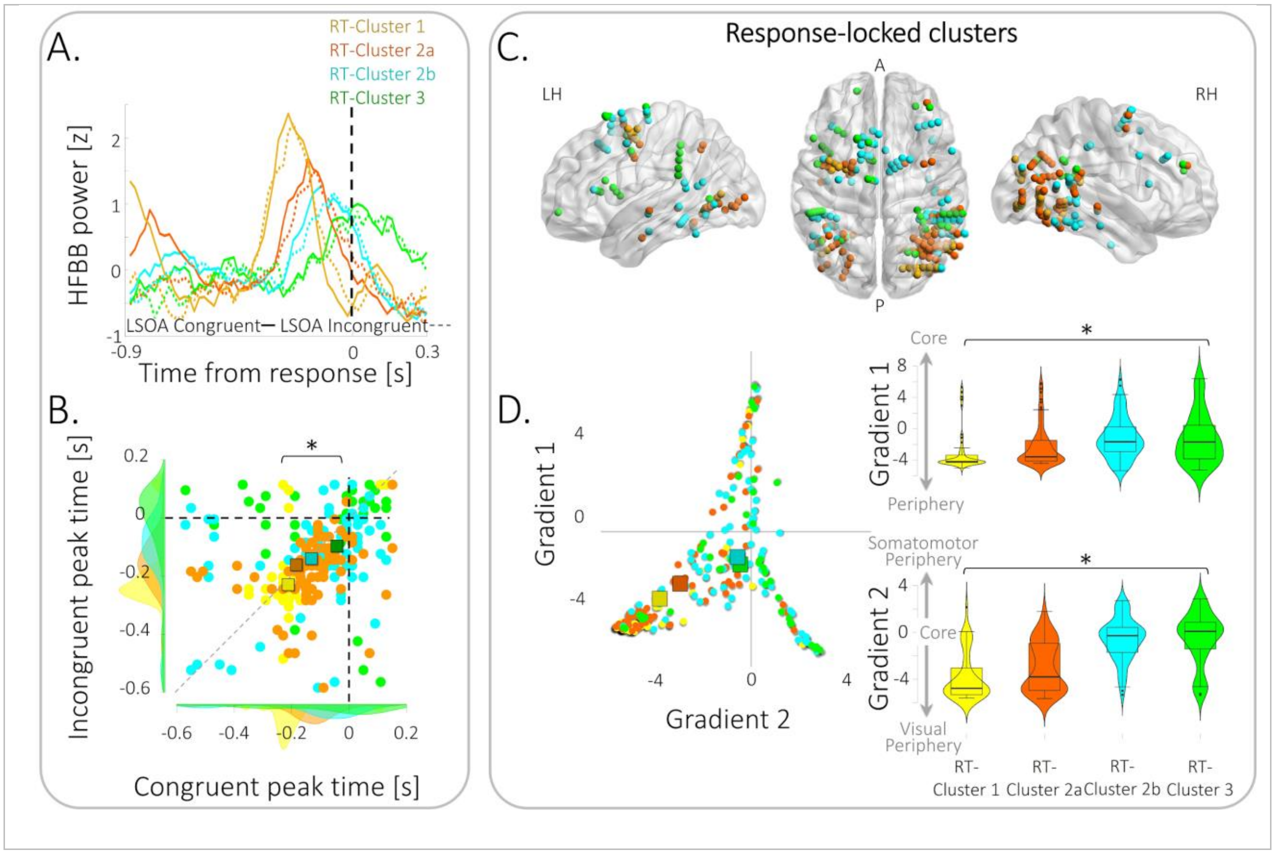

Figure S11 – Response-locked clusters exhibit a spatiotemporal gradient. (A) Temporal gradient of activity in response-locked clusters: Trimmed-mean response-locked response of the RT-Cluster 1, RT-Cluster 2a, RT-Cluster 2b and Cluster 3. Black dashed line depicts RT. (B) Scatter plot of peak times of mean response-locked activity of the contacts of RT-Cluster 1 (yellow circles), RT-Cluster 2a (orange circles), RT-Cluster 2b (turquoise circles) and RT-Cluster 3 (green circles) clusters, in the Congruent (x axis) and Incongruent (y-axis) long-SOA conditions, showing a significant temporal gradient (Mixed ANOVA: Cluster main effect $F(3,245)=12.57$, $p<0.001$, $\eta^2=0.086$; linear polynomial contrast: $p\leq0.001$). Squares represent mean peak time; Dotted grey line denotes the equity line; Shaded areas represent peak time distributions. (C) Core-Periphery gradient: Clusters' anatomical localization follows Core-Periphery gradients (Margulies et al., 2016), where RT-Cluster 1's contacts are the most peripheral and RT-Cluster 3's contacts are closest to core regions. (D) Left: Scatter plot of contacts localization along core-periphery gradients (RT-Cluster 1 - yellow circles; RT-Cluster 2a - orange circles; RT-Cluster 2b – turquoise circles; RT-Cluster 3 - green circles). Top & bottom right: Violin plots of contacts localization along Core-Periphery gradients for RT-Cluster 1 (yellow), RT-Cluster 2a (orange), RT-Cluster 2b (turquoise) and RT-Cluster 3 (green) clusters, showing a significant core-periphery gradient (Gradient 1: $p=0.001$, $\eta^2=0.06$; linear polynomial contrast: $p\leq0.001$; Gradient 2: $p<0.001$, $\eta^2=0.32$; linear polynomial contrast: $p\leq0.001$).

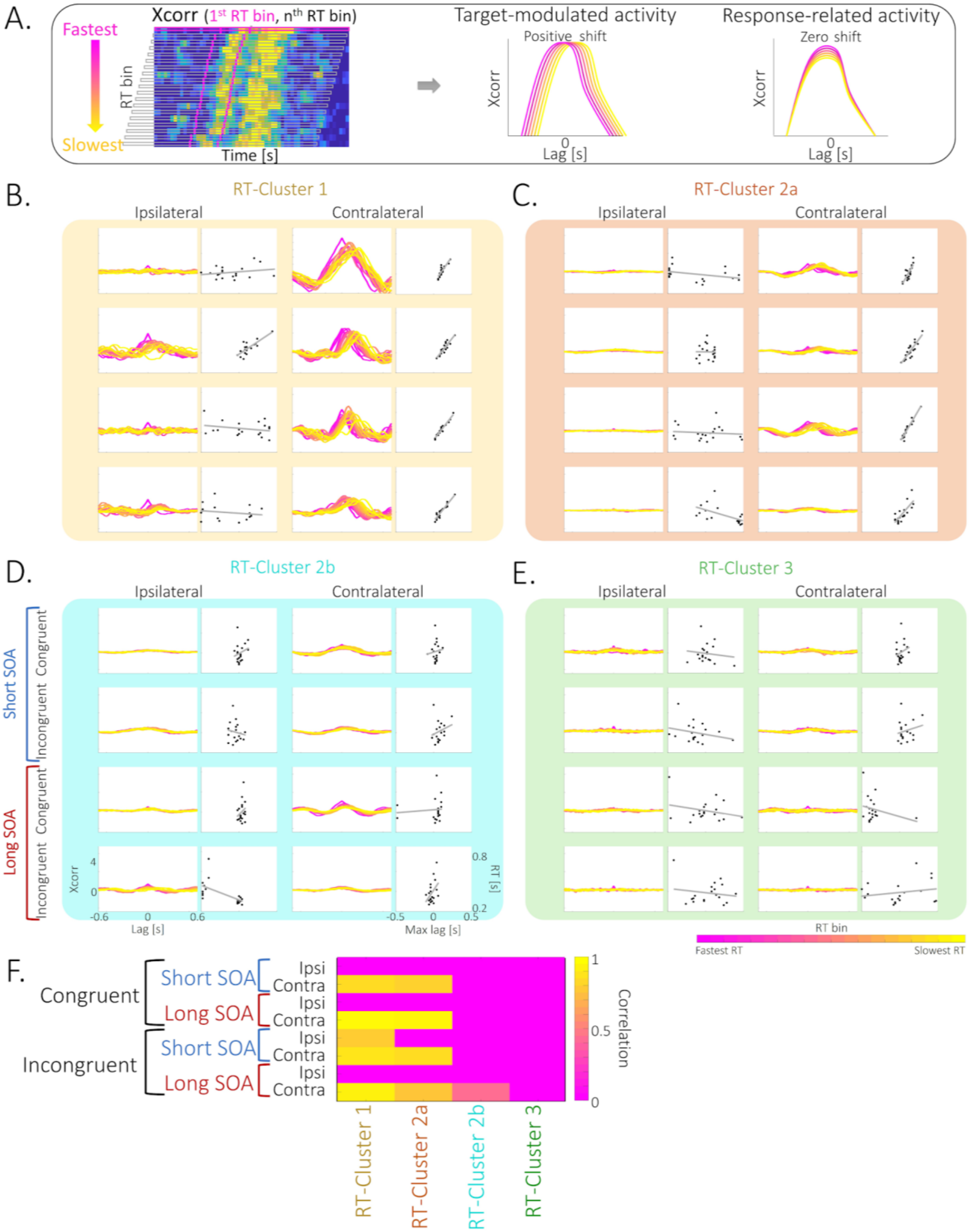
A.
Xcorr (1st RT bin, nth RT bin)
Fastest
Slowest
RT bin
Time [s]
Target-modulated activity
Positive shift
Xcorr
0
Lag [s]
Response-related activity
Zero shift
Xcorr
0
Lag [s]
B.
RT-Cluster 1
Ipsilateral
Contralateral
C.
RT-Cluster 2a
Ipsilateral
Contralateral
D.
RT-Cluster 2b
Ipsilateral
Contralateral
Short SOA
Long SOA
Congruent
Incongruent
Congruent
Incongruent
Xcorr
4
0
-0.6
0
0.6
Lag [s]
-0.5
0
0.5
Max lag [s]
0.8
0.2
RT [s]
E.
RT-Cluster 3
Ipsilateral
Contralateral
RT bin
Fastest RT
Slowest RT
F.
Congruent
Incongruent
Short SOA
Long SOA
Short SOA
Long SOA
Ipsi
Contra
Ipsi
Contra
Ipsi
Contra
Ipsi
Contra
1
0.5
0
Correlation
RT-Cluster 1
RT-Cluster 2a
RT-Cluster 2b
RT-Cluster 3

Figure S12 – Correlation of cluster response-locked neural activity with visual processing. (A) Schematic illustration of the procedure for computing the cross-correlation (Xcorr) between response-locked neural activity across RT bins: Cross-correlation between response-locked activity at the fastest RT bin and all subsequent bins was computed (left; magenta lines depict mean Cue and Target onset times). If cluster activity is target-associated, maximal cross-correlation will follow the RT (here indicative of quantile's mean target-onset time), resulting in a positive shift of cross-correlation lag (middle). If cluster activity is response-associated, maximal cross-correlation will be centered on target onset, resulting in a zero shift across all RT bins (right). Fastest bin- magenta; slowest bin– yellow. (B)-(E) Cross-correlogram of response-locked neural activity at different RT bins (pink- fastest RT; yellow - slowest RT) as a function of cross-correlation lag (left columns), and Pearson correlation (grey line) between maximal cross-correlation lags (Max lag) and bin's mean target onsets (right columns), across the 8 conditions (Congruent / Incongruent X short-SOA / long-SOA X Ipsilateral target / contralateral target) for RT-Cluster 1 (yellow), RT- Cluster 2a (orange), RT- Cluster 2b (turquoise) and RT- Cluster 3 (green). (B)-(C) Activity in RT-Cluster 1 & RT-Cluster 2a is target-associated: Cross-correlation plots are positively shifted in a spatially sensitive manner, i.e. only for contralateral targets. (D)-(E). Activity in RT-Cluster 2b & RT-Cluster 3 is response-associated: Cross-correlation plots show no shift. (F) Significant positive correlation between cross-correlation maximal lag and bin mean RT in the RT-Cluster 1 & RT-Cluster 2a: significant ($p<0.05$) positive correlations were found mainly in these two clusters, only for contralateral targets.

Finally, we investigated whether the embedding of the cluster gradient in the cortical gradient extends beyond spatial topography and shares a functional hierarchy with it. Importantly, one of the features that changes along the cortical gradient is the length of temporal receptive windows (TRW, i.e. the time window in which previously presented information can affect the processing of a newly arriving stimulus), which lengthen and integrate over longer durations when moving up the gradient [49,50,61,62]. Temporal integration was suggested as a potential mechanistic computation underlying RT facilitation and IOR. Therefore, we asked if TRWs also lengthen along the cluster gradient. We estimated TRW length by calculating the decay time constant of the autocorrelation function applied to the non-filtered neural time series for each contact in the three clusters [62,63]. TRW length increased when moving up the cluster gradient (Fig. 3E; TRW length: Cluster 1 to 54.33±44.96; Cluster 2 to 102.56±99.15; Cluster 3 to 124.91±87.13; 1-way ANOVA: $F(2,103.98)=17.83$; $p<0.001$, $\eta^2=0.113$; linear polynomial contrast: $p\leq0.001$), suggesting that along this trajectory, integration is over longer durations [49,64,65]. Hence, the cluster gradient shares a similar temporal integration hierarchy with the cortical gradient, [6,42], mirroring the pattern of integration/segregation of Cue-Target neural responses observed along the cluster gradient.

Discussion

Here we aimed to establish how attention-capturing events modulate visual, attentional and response-associated neural processing in the human brain, and how the involved brain networks map onto the large-scale cortical topography. Overall, we provide a high-resolution, comprehensive depiction of the cortical dynamics underlying human exogenous attention. Our findings reveal that attentional events differentially define neural activity along a series of clusters, which form a spatiotemporal gradient, extending from the visual cortex to frontoparietal regions. This gradient is embedded in the periphery-core cortical topography, which is a primary organizing axis of the human cerebral cortex [49,51,53]. Cluster neural activity at one end of the gradient is modulated by visual attributes, while activity at the gradient's other end reflects the timing of the upcoming response, with attentional modulations occurring at the intersection of visual and response signals. Notably, temporally-close stimuli elicit discrete neural responses at the visual end of the gradient, yet at its frontoparietal end, they elicit a single pooled neural response. Moreover, TRWs lengthen along the cluster gradient, like the hierarchy of timescales along the cortical topography in which the clusters are embedded. These findings stress the importance of studying fast and dynamic cognitive processes with high-resolution methods, and suggest that attention is not a discrete multi-step operation, but rather arises over large neural gradients embedded in the cortical topography, along which perceptual and response-related signals integrate.

We identified three key components along exogenous attention's cortical gradient. The first, Cluster 1, is situated at the peripheral end of the cortical gradient, encompassing the occipito-temporal cortex [66], and the vicinity of the FEFs [67], where ultra-fast visual activation was reported [68]. Its occipital and FEF-adjacent contacts were structurally connected mainly by the middle branch of the SLF (SLF II). Functionally, it only responded to contralateral visual stimuli, and its neural responses to the cue and target were segregated, even at the short cue-target delay.

Clusters 2 and 3 are located closer to core regions of the cortical gradient, and overlap with known frontoparietal attention networks [19,56,69]. The neural activity in Cluster 2, occurring midway along the gradient, is sensitive to cue-target spatial positions and delays, and exhibits IOR-related onset and offset. Both visual processing of the target and manual response preparation shape the neural activity in this cluster, which is lateralized to the right hemisphere, consistent with lesion and neurostimulation data on IOR [28–30,33,34]. Despite the fact that we did not find a significant behavioral effect of RT facilitation, the involvement of Cluster 2 neural activity in attentional computation in the short-SOA condition is plausible. First, RT facilitation is an elusive effect, easily masked by other processes [6,8,11]. Our design was not optimal for unmasking the behavioral effect because of the lack of temporal overlap between cue and target, which is one of the conditions that favors the appearance of RT facilitation in detection tasks [8]. In addition, the Poffenberger effect we observed further masked the RT facilitation effect. Yet, current theories postulate that facilitation exists [6,11] even when it is behaviorally offset by IOR, which is always present with peripheral cues, even at short SOAs. Our exploratory analysis revealed in Cluster 2 at the short-SOA a differential cue-target summed activity, which translates to a neural preference for stimuli repeating in the same specific spatial contralateral location. This neural effect dovetails with the behavioral RT facilitation effect, in which RT is faster for repeated stimuli in a specific location. Therefore, our results suggest that the activity in Cluster 2 represents a key attentional processing of exogenous cueing effects in both short and long SOAs, associating perception and action signals.

On the other hand, neural activity in Cluster 3 shows sensitivity to stimulus identity, with stronger activation for response-requiring targets than for cues. It is lateralized to the left hemisphere, contralateral to the responding hand, and its response-locked activity peaks at the time of the motor response, which also modulates its target-locked activity. Furthermore, this cluster is anatomically situated between the somatomotor end and transmodal core regions of the core-periphery gradients. Because the patients only responded with their right hand, we cannot completely rule out that the left hemisphere response is simply stronger, and thus the cluster's activity is not related to response aspects of the task. However, this cluster contains right hemisphere contacts as well, and its contacts are also localized in non-motor regions, such as the posterior temporal lobe and supramarginal gyrus. This fact, together with the entire line of evidence mentioned above, supports the suggestion that Cluster 3 encodes decisional and response aspects.

Responses were only made using the right hand in order to avoid RT effects related to congruence between the responding hand and the side of the presented target. Despite the fact we cannot completely rule out that the left hemisphere response is simply stronger, our interpretation is based on an entire line of evidence, and not solely on the asymmetry towards the left hemisphere of Cluster 3 contacts. Importantly, this Cluster contains right hemisphere contacts as well, and its contacts are localized also in non-motor regions, such as the posterior temporal lobe and supramarginal gyrus. Additionally, we found that Cluster 3 responses are stronger for the response–demanding Target than for the Cue. This preference is spatially invariant and is observed in both right and left hemispheres. Moreover, this Cluster's contacts are mapped to the somatomotor periphery and to the high-level core regions of the cortical gradient. Therefore, we suggest the interpretation that this cluster activity is associated with response aspects, but not to motor planning per se.

Along all this gradient of clusters, neural activity shows spatial sensitivity, sensitivity to cue-target delay, sensitivity to task relevance, and association with RT, therefore encoding the information necessary to underlie exogenous attention RT effects such as IOR, which depend on the delay and co-localization of attentional events.

Importantly, these findings depart from traditional attention models of multi-step processing across visual areas. Instead, exogenous attentional effects seem to emerge along a continuous neural trajectory of large-scale cortical gradient, which bridges perceptual and response processing. These findings reconcile long debated theories about the perceptual-motor (or input-output) dichotomy of attentional processes [10,11,70]. We find both perceptual and motor effects; however, they form a gradient rather than a dichotomy. These findings dovetail the idea that attention organizes the activity of sensory and motor networks, generating alternating states for sampling sensory information versus shifting attention and responding [71].

Despite the overlap of Clusters 2 and 3 with known frontoparietal attention networks, their anatomy and function diverge from neurophysiological models of human attention (e.g. Corbetta and Shulman, 2002). First, in the TPJ, which constitutes a single node of the right-lateralized ventral attention network [19], these clusters occupy distinct portions, which differ in their functional and structural connectivity [41,58,72,73]. The caudal TPJ portion (Cluster 2) connects to the superior frontal gyrus/FEF of the dorsal attention network [41,58,73] through the middle branch of the SLF (SLF II), and thus provides direct communication between the ventral and dorsal attention networks.

In contrast, the rostral TPJ (Cluster 3) is connected to the middle and inferior frontal gyri through the ventral branch of the SLF (SLF III), thus linking nodes of the ventral attention network. Both SLF II and SLF III show anatomical or functional lateralization to the right hemisphere [58] and their inactivation or disconnection was associated with signs of left spatial neglect [33,35]. Indeed, our findings demonstrate that temporo-parietal and prefrontal contacts in Clusters 2 and 3 are connected by the SLF, and our overlap analysis suggests that in the right hemisphere the right-lateralized Cluster 2 is more connected by the SLF II, while the left-lateralized Cluster 3 is more connected by the SLF III in the left hemisphere. Yet because of the overlap between probabilistic maps of SLF II and III templates, these latter findings should be validated in future studies, exploring neural activity and tractography in the same sample of participants.

Similarly, Clusters 1, 2 and 3 encompass contacts in the dorsolateral prefrontal cortex, indicating that when examining in sufficient spatiotemporal resolution, this region, which constitutes a single node of the dorsal attention network [19], can be dissociated into distinct networks.

Furthermore, our findings localizing contacts from Cluster 2 and 3 to the posterior temporal lobe, a region outside the scope of hallmark attention models [19,56], suggest that this area may contribute to exogenous attention processing, dovetailing recent studies in humans and non-human primates [74,75].

Functionally, our findings suggest that contrary to these models, not only do the prefrontal nodes of the dorsal attention network process information pertaining to the contralateral visual field [41,76], but rather respond to stimuli in both contralateral and ipsilateral visual fields. Conversely, the activity recorded in contacts in the TPJ belonging to Cluster 2 presented spatial sensitivity, contrary to assumption of some models that this functional region lacks spatial mapping [19]. Additionally, our findings concerning the TPJ are not completely consistent with the prominent Corbetta and Shulman model [19]. Based on fMRI data, this model postulates that exogenous orienting does not activate the TPJ, which only responds to reorienting to response-relevant targets. Corbetta and Shulman [19] suggest that when an important stimulus appears outside the current focus of attention, fast-latency signals from the ventral network initiate reorienting by sending a ''circuit-breaking'' or interrupt signal to dorsal regions, which change the locus of attention. In other words, according to this model, TPJ should not respond to peripheral non-informative cues, only to unexpected incongruent targets. However, we found that TPJ contacts were activated also in response to cues, and also in congruent trials, when target location corresponded to the location of the preceding cue, aligning with previous causal evidence from a TMS studies [77]. Therefore, our findings suggest that the TPJ is not just a circuit breaker responding when unexpected and pertinent targets appear and reorienting of attention is needed [19].

What are the cortical characteristics that favor the localization of attentional processing to a particular extent of the cluster gradient? Beside the convergence of perceptual and response signals, a potential factor may be the temporal integration properties of the involved regions. This trait changes in a continuous manner along the temporal hierarchy of TRWs, a key feature of the core-periphery gradient, analogous to the spatial hierarchy of receptive fields [49,50,61,64,65,78,79]. Thus, along this gradient, integration is over longer durations, and selectivity for coherent temporal structures increases [49,61,64,65]. TRW length is intrinsically determined by a region's cytoarchitecture, and macro- and micro-circuit connectivity [50,65]. Such a hierarchy of TRWs could enable a dynamical interaction with a continuously changing environment, with fast fluctuations associated with sensory processing at the bottom of the hierarchy, and slow fluctuations, which reflect contextual changes in the environment, at the hierarchy top [65]. Moreover, a hierarchy of TRWs can serve as a scaffold for putative recurrent temporal computations that support neuronal sensitivity to sequential events, and boost robustness to changes in input gain and timing, such as temporal pooling, i.e. the integration of prior information across the TRW [64]. Indeed, recent evidence showed that TRWs could serve cognitive functions [50,80,81]. For example, prefrontal cortex TRWs expanded during working memory maintenance and predicted individual performance [50]. Correspondingly, our finding that TRWs lengthen along the cluster gradient reveal potential temporal operations at the basis of exogenous attention. Furthermore, the integration of cue-target responses in Clusters 2 and 3 in the long-SOA could reflect temporal pooling [64]. In Cluster 1, situated lower on the gradient, TRWs are shorter, allowing for segregation of activity even at short delays. In upstream frontoparietal clusters where TRWs are longer, cue- and target-induced responses resulted in a single activity peak. This temporal pooling might group the cue and target in a single event [6,48,82], leading to RT facilitation at short cue-target delays [6,42,82]. These findings dovetail with the hypothesis that RT facilitation results from a summation of cue-related and target-related responses, thus reflecting hard-wired limitations of the neural system that cannot respond separately to rapidly repeated stimuli, and processes them as a single event [6,42,82]. According to Cue-target event integration-segregation hypothesis [6,42], RT facilitation arises when the net effect of facilitatory processes, such as exogenous spatial attention orienting and binding-associated spatial selection benefit, is larger than the detection cost the binding might cause due to the difficulty to detect the onset of the second bound stimulus [6]. Longer cue-target delays could instead provide the system with enough time to segregate cue- and target-related responses [6,42]. Hence, our results contribute to resolving the longstanding debate surrounding the nature of IOR. In Clusters 2 and 3, IOR was linked to a segregation of neural responses, with distinct peaks corresponding to cues and targets. Notably, in Cluster 2 (encompassing the angular gyrus and lateral prefrontal cortex), the timing of these distinct peaks, as well as their decay, mirrored behavioral IOR. Consequently, our findings provide a refined anatomical and functional specification of earlier results obtained from studies involving brain-damaged patients [33,83] and those employing transcranial magnetic stimulation (TMS) on the parietal cortex [28,29,84]. This more detailed insight contributes to a better understanding of the precise temporal mechanisms underpinning cognitive processes.

TRWs may be linked to another neural temporal phenomenon: oscillations. The relationship between the temporal integration hierarchy and oscillations is still unclear. A gradient of oscillatory frequencies, similar to the timescales gradient [50], has been described along the posterior-anterior cortical axis [85]. Gao and colleagues [50] suggested that the gradients of oscillations and neural receptive windows may (at least in part) share circuit mechanisms at different spatial scales, based on the similarity of these gradients and on known mechanisms of asynchronous and oscillatory population dynamics, analogous to the relationship between characteristic frequency and decay constant in a damped harmonic oscillator model. In the context of attention, theta rhythms from frontoparietal attentional networks have been proposed to rhythmically sample and temporally organize sensorimotor functions, creating alternating periods of attentional focus or shift [69,71]. Thus, conceptually, neural oscillations may serve as 'broadcasted' attentional signals affecting other brain regions. Similarly, TRWs can be thought of as 'receivers' of oscillatory attentional signals, determining how attentional modulation is processed. For example, the length of the TRW can determine how much of the oscillation's period will be summed together, thus generating a differential modulatory effect of the same oscillation frequency along different parts of the attentional gradient. Although we did not find evidence for the involvement of theta phase in the observed attentional effects, further research is needed to explore the relationship between these phenomena, and test the hypothesis that they interact and influence each other along the attentional gradient and together dynamically contribute to attentional processing.

iEEG provides robust direct signals with unparalleled spatiotemporal resolution in humans, but it also has limitations [86–88]. Although contacts with epileptic activity are discarded from the analysis, iEEG data is collected from a pathological population, which might not be a valid model for neurotypical cognition. However, the fact that our participants demonstrated a neurotypical pattern of behavioral responses is reassuring in this respect. In addition, iEEG has a limited and inhomogeneous spatial coverage, determined solely by medical needs. We mitigated this limitation by collecting a large set of data from 28 patients thus achieving a comprehensive coverage, and by considering the coverage in our analyses when needed, i.e. when comparing cluster hemispheric lateralization. As a result, some parts of the puzzle might be missing, yet the high signal-to-noise ratio and the excellent resolution in the covered regions ensure that the activity recorded from them is robust.

Our findings challenge traditional attention models of multi-step processing across visual areas. They indicate that exogenous attentional effects follow a continuous neural trajectory across large-scale spatiotemporal gradients, where distinct processes of segregation and integration of attentional events occur. These neural dynamics provide the mechanisms through which the timing of attentional events shape neural processing and consequently our behavior. Our findings suggest that the circuits for attention form a dynamic network, in which attentional effects are properties of the overall network, not separate functions assigned to different parts [89], and thus place exogenous attention processing in the context of the larger topographical organization of the human brain.

Methods

Participants and recordings

Thirty one patients (aged 31.8 ± 8.3 years, 16 women; See Table 1 for full details) with drug-resistant focal epilepsy, hospitalized at the Pitié-Salpêtrière Hospital in Paris, participated in this study after giving their informed consent (CPP Paris VI, Pitié-Salpêtrière Hospital, INSERM C11-16). Three patients were excluded post hoc because of severe cognitive impairments and abnormally long response times (1 patient) or because of the presence of wide-spread brain lesions (2 patients), leaving a total of 28 included patients. For medical reasons, patients underwent intracerebral recordings by means of stereotactically implanted, multilead intracerebral depth electrodes (iEEG). Patients' experimental recordings were performed 4-14 days post implantation, while their antiepileptic medication was gradually decreased and/or stopped. Patients were implanted with 5–12 platinum electrodes (AdTech®, Wisconsin) endowed with 4-12 contacts with a diameter of 1.12 mm and length of 2.41 mm, with nickel-chromium wiring. The distance between the centers of two contacts is 5 mm. Electrode placement was uniquely determined by clinical criteria. In 13 patients neuronal recordings were performed using an audio–video–EEG monitoring system (Micromed), which allowed simultaneous recording of 128 depth-EEG channels sampled at 1024 Hz (0.18 to 220 Hz bandwidth). In 18 patients the recording was done with a Neuralynx system (ATLAS, Neuralynx, Inc.), allowing to record up to 160 depth-EEG channels sampled at 4 KHz (0.1 to 1000 Hz bandwidth). The least active electrode (preferably in white matter) was defined as the reference electrode. Before analysis, all signals were down-sampled to 512Hz and re-referenced to their nearest neighbor on the same electrode, yielding a bipolar montage. Bipolar montage helps eliminate signal artifacts common to adjacent electrode contacts (such as 50Hz line artifact) and achieves a high local specificity by cancelling out effects of distant sources that spread equally to both adjacent sites through volume conduction.

Spatial localization of the electrode was automatically computed in native space using the Epiloc toolbox [90] developed by the STIM engineering facility at the Paris Brain Institute (https://icm-institute.org/fen/cenir-stim//) using co-registered pre-implantation 1.5T or 3T MR scans and post-implantation CT scans. Each contact localization was automatically labeled according to the Desikan-Killiany-Tourville atlas parcellation [91] in patients' native space, using Freesurfer image analysis suite (http://surfer.nmr.mgh.harvard.edu/) that is embedded in Epiloc. In 10 participants with low quality MRI scans for which automatic contact labelling was not possible, two experimenters labeled manually and independently the contacts (inter-rater reliability *R*=0.99) based on anatomical landmarks in the patients' native space, according to the parcellation of the Desikan-Killiany-Tourville atlas [91].

Experimental task

A PC Dell Latitude D600 running E-prime 3.0 software (Psychology Software Tools, Pittsburgh, PA) controlled the presentation of stimuli, timing operations, and data collection. Stimuli were presented on a black background. Two grey empty boxes (3° long and 2.5° large) were horizontally arranged around a central fixation point, located at the center of the screen. The distance between the center of the fixation point and the center of each box was 7.7°. The fixation point consisted of a grey plus sign (0.5° x 0.5°). Cues consisted of a 100-ms thickening (from 1 mm to 3 mm) of the contour of one lateral box. The target was a white "X" (1° in height), appearing at the center of one of the lateral boxes, with equal probability. Patients sat in front of the computer screen at a distance of approximately 57 cm. Fig. 1A illustrates the experimental procedure. Each trial began with the appearance of the fixation point and the two placeholder boxes for 1,000 ms. The cue followed for a duration of 100 ms. After a stimulus-onset asynchrony (SOA) of either 150 ms or 600 ms, the target appeared and remained visible for 150 ms. The placeholder boxes disappeared when a response was detected or after 3000 ms if no response was made. The experiment consisted of a total of 3 blocks of 112 trials, comprising 50 short SOA trials, 50 long SOA trials, and 12 catch trials, in which no target appeared after the cue, all randomly interleaved. Cues were non-informative, i.e. they indicated the target location on 50% of trials (Congruent location), and the opposite location (Incongruent location) on the remaining 50% of the trials. Patients were instructed to maintain their gaze at the central fixation point throughout the test, and to respond to the target as fast and accurately as possible, by pressing the right mouse button with their right index finger. Gaze position was verified by confrontation. The mouse was placed in an approximately central position with respect to the patient's body midline. It was stressed that the position of cues was useless for predicting the target position, and should not be taken into account when responding. Before the first experimental block, patients performed 10 practice trials.

Behavioral analysis

For each participant, trials with response time (RT) exceeding 3 std or faster than 100 ms were excluded from analysis. Participants' mean RT were compared using a 2-way repeated measures ANOVA, with Congruence and SOA as factors, using JASP software (version 0.14.1) [92]. All post hoc comparisons were corrected for multiple comparisons using the Holm correction.

iEEG preprocessing

Data preprocessing was done using the FieldTrip toolbox for EEG/MEG-analysis (Donders Institute for Brain, Cognition and Behaviour, Radboud University, the Netherlands. See http://fieldtriptoolbox.org [91]) and Matlab (Matlab R2016b and R2020a, The MathWorks, Inc.). Continuous iEEG signals were visually inspected. Electrodes with excessive epileptic spikes, located at or near the epileptic focus, were rejected. Then, time windows showing epileptic transient activity were identified and excluded from further analysis. Next, epochs were extracted, between 1 s before target onset and 1.5 s after target onset. Additionally, epochs were extracted, between 1 s before the response time and 0.4 s after it. A second artefact rejection procedure was then performed on the epoched data, and trials with excessive variance, maximal signal or kurtosis of their signal distribution were semi-automatically rejected. After epileptic artifact removal, 1403 of the bipolar contacts were usable for analysis, 671 of them were in the left hemisphere and 732 in the right hemisphere (see Fig. 2A and Table 2 for the localization of the usable contacts). According to the Desikan-Killiany-Tourville atlas parcellation [91], 336 (23.9%) of the contacts were located in the frontal lobe, 689 (49.1%) in the temporal lobe, 48 (3.4%) in the occipital lobe, 138 (9.8%) in the parietal lobe, 46 (3.2%) in subcortical regions and 146 (10.4%) in white matter.

A pseudo-whole-brain analysis approach was selected, focusing on high-frequency broadband (HFBB) activity (55–145 Hz a-priori range), a marker for multi-unit neural activity [93], which was associated with various cognitive processes [69,94]. HFBB power was extracted from each bipolar contact time series, by convolving the signal with a set of complex Morlet wavelets (with 8 cycles), in 20 logarithmically spaced center frequency bands. Every trace was separately baseline-corrected by means of a z-score relative to the trials' baseline distribution in the 700 ms prior to cue onset, separately for each of the frequency bands. This approach accounts for the 1/f signal drop off in the high-frequency band with increasing frequencies. Finally, we discarded the edges to avoid filter artifacts and extracted individual non-overlapping trials relative to either target onset (−0.9 to 1.36 s) or relative to the response time (−0.9 to 0.3 s). HFBB signals were down-sampled to 50 Hz for further analysis.

Trajectory k-means clustering

In order to reveal contacts' prototypical temporal patterns of activity across experimental conditions, we developed a custom-made clustering approach based on k-means clustering, implemented through Matlab (Matlab R2016b and R2020a, The MathWorks, Inc.). Clustering was done on responsive contacts, defined as having a target-locked significant effect ($p\leq0.05$ uncorrected) of at least 100 ms in one or more of the eight experimental conditions compared to baseline. For each condition in a given contact, a time-resolved independent samples t-test was performed, in which each time point across trials was compared to the distribution of all the baseline samples pooled over all that condition's trials (-0.2-0 s prior to cue onset). This yielded 644 contacts (See Table 2 for their spatial localization), and their mean target-locked or response-locked activity time series were transformed into an 8D matrix, where each dimension corresponded to one of the eight experimental conditions (short/long SOA x congruent/incongruent x contralateral/ipsilateral target relative to the recording contact; see Figure S2A-B for an illustration and example). The trajectories, consisting of the mean target-locked or response-locked HFBB power across the 8-dimensional condition space, were entered into the clustering algorithm. Activity across conditions was z-scored relative to the distribution of the trials' entire duration. Trajectories were iteratively partitioned (10,000 iterations) into 2-9 clusters, in which each contact was assigned to the cluster with the nearest centroid trajectory. This was achieved by minimizing the sum of the Manhattan distances, time-point-by-time point to quantify trajectories similarity while preserving temporal order. Based on the elbow method [94] the 6-cluster solution was chosen for the clustering of target-locked activity (See Fig. S2). Figure S6 shows the clustering of target-locked activity for 2-8 cluster solutions, demonstrating the stability across different k solutions of the three clusters further analyzed. The stability was assessed using contingency tables analysis performed using JASP [92], estimating the correspondence between the contacts assigned to these three clusters and specific clusters from each k solution. There was a strong significant correspondence between the assignment of contacts to clusters in the 6-cluster solution and in the other k solutions (Table S1). A k-solution cluster was marked as stable if the main group of contacts composing it could be mapped to one of the three further analyzed clusters, which in turn shared most of its contacts with that cluster (Fig S6, Table S1). Based on the elbow method [95], for the clustering of response-locked activity, a 7-cluster solution was chosen (See Fig. S4). In order to identify the correspondence between target-locked and response-locked clusters, a contingency tables analysis was performed using JASP [92]. The distribution of the 28 participants' contacts across target-locked and response-locked clusters is shown in Fig. S4, demonstrating that clusters did not result from any single participant's temporal activity, but rather reflected temporal patterns across many participants. The linear correlation between the centroid time-series of all conditions across target-locked clusters revealed that out of the six target-locked clusters, three had a dynamic temporal profile across the different experimental conditions. These clusters were positively correlated among themselves, forming a distinct cluster group (See Fig. S5). The correlation pattern within the remaining three clusters was more uniform, and negatively correlated across clusters. Clusters 1, 2 and 3 were used as a type of functional region of interest for further analyses. We chose to focus on these clusters because of their stability across clustering solutions and their variable responses across experimental conditions (Figure S5). Conversely, even if the remaining clusters might contribute to the processing of the different attentional conditions, they could not explain the differences between them, given that their correlation pattern across experimental conditions was uniform (Figure S5).

Cluster hemispheric lateralization

The hemispheric lateralization of the clusters was tested on a subgroup of contacts localized in cortical volumes that were sampled in both hemispheres. This was done to overcome the confound of unequal coverage within the hemispheres. To identify similarly-covered contacts, a 3mm radius sphere (corresponding to the assumed volume recorded by iEEG contacts [88]) was fit around each contact using SPM12 [96], and the overlap between each of the spheres and the entire covered volume in the other hemisphere was calculated. The cluster-distribution of the 309 resulting contacts (148 in the left hemisphere and 161 in the right hemisphere) across the hemispheres was compared using a contingency table analysis in JASP [92], and post hoc binomial test with Holm correction were conducted to identify the clusters with significant hemispheric lateralization.

iEEG statistical analyses

All statistical analyses were performed using statistical toolbox in Matlab (Matlab, R2020a, The MathWorks, Inc.) and JASP version 0.14.1 [92].

IOR-related neural activity

In order to test in which of the clusters neural activity was IOR-related, we compared between Congruent and Incongruent trials in the long SOA condition, For each cluster, we performed a time resolved 3-way ANOVA (Fig. 4) with Congruence, Contact's Hemisphere and Target Laterality (relative to the contact), on the target-locked HFBB signal in each time point (between 0-0.8 s post target onset), across all the cluster's trials (pooled over contacts and participants). Holm multiple comparisons correction was applied over all the time points within each main effect and interaction. Post hoc comparisons were performed on time points in which the Congruence*Hemisphere interaction was significant, with Holm correction for multiple comparisons. Detailed ANOVA corrected p-values for each cluster are shown in Table S2.

RT-modulation of target-locked neural activity and visual modulation of response-locked neural activity

In order to test in which of the clusters neural activity was modulated by the RT, we sorted in each cluster all the trials pooled over the conditions according to their RT. We then binned them into 20 quantiles (Fig. S8A). Within each cluster, we tested the effect of the RT-bin using a time-resolved 1-way repeated measures ANOVA, on mean target-locked HFBB signal across conditions, in each time point (between 0-0.8 s post target onset; pooled over contacts and participants). Holm multiple comparisons correction was applied over all the time points. Similar analysis was performed on the response-locked clusters. Because RT is defined as the time from target onset to the response, this procedure sorted the response-locked trials according to target onset, and thus could unveil visual modulation of response-locked activity.

Temporal gradient analysis

Within each target-locked cluster, contacts' time of the maximal HFBB power (between 0-0.6s post target onset) was identified, separately for Congruent and Incongruent long SOA conditions. Contacts' peak times were compared across the three clusters using a mixed-repeated measures ANOVA, with Congruence as a within subjects factor and Clusters as a between subjects factor. A linear post-hoc polynomial contrast was used to test if peak time was linearly ordered across clusters. Similar analysis was performed on the response-locked clusters.

Core-Periphery gradient analysis

In order to test if the clusters' anatomical localization followed the Core-Periphery gradients, the MNI coordinates of target-locked clusters' contacts were assigned the closest voxel's gradient value on the two principle gradients described by Margulies et al. [51]. The distances between contacts and the closest voxels did not differ across clusters (1-way ANOVA, $F_{(2,230)}=0.064$, $p=0.94$). Contacts' gradients' values along the two gradients were compared using a 1-way ANOVA with Clusters as a factor. A linear post-hoc polynomial contrast was used to test if clusters were linearly ordered along the two gradients. Similar analysis was performed on the response-locked clusters. Here too, the distances between contacts and the closest voxels did not differ across clusters (1-way ANOVA, $F_{(3,246)}$=1.23, p=0.30).

Estimation of temporal receptive window length

TRW length was assessed by computing the across-trial autocorrelation [62,97] of the non-filtered iEEG signal (down-sampled to 100Hz; 350-1150ms post target), for each of the contacts in the three target-locked clusters. An exponential decay function (e^(−t/τ)) was fit to the contacts autocorrelation coefficient across time-lags. TRW length for each contact was defined as the time constant (τ) of the contact's fitted exponential decay function, i.e., the time it takes for the autocorrelation to decrease by a factor of e [62,97].

Structural connectivity of pre and post rolandic contacts

To determine the connectional anatomy of the three clusters we used fiber tracking in a sample of 176 healthy controls from the Human Connectome Project database [57] and used a threshold-free cluster enhancement (TFCE)-based non-parametric t-test to determine the significant tracts. Contacts of each cluster were fitted with a 3mm radius sphere around them as described above, and labeled as pre or post rolandic, using the central sulcus as a reference point in patients native space (Number of pre and post rolandic contacts per cluster: Cluster 1 - 8:60, Cluster 2 - 23:74, Cluster 3 - 34:33). The resulting pre and post rolandic contact spheres were used as region-of-interests (ROIs) to identify white matter fibers connecting them. This fiber-tracking analysis was done on the high-resolution 7T MRI scans of 176 healthy individuals from the Human Connectome Project database [57] using TrackVis 0.6.1 (http://trackvis.org/). The resulting tractography maps were binarized and significant tracts across individuals were determined using a threshold-free cluster enhancement (TFCE)-based non-parametric t-test in FSL 6.0 (1000 permutations, height threshold of 0.95 to control significance level at p<0.05; https://fsl.fmrib.ox.ac.uk/fsl/fslwiki/FSL). The corrected t-maps were then used to identify the number of white matter voxels that overlapped with the SLF tracts templates of the white-matter probability maps of the BCBtoolkit (http://toolkit.bcblab.com/). In order to identify the tracks overlapping with the three branches of the SLF, probability maps were thresholded at 50%, yet the large overlap between the tracts of SLF II and SLF III templates (present even with a 90% probability threshold) made the differentiation between them difficult. The number of significant overlapping voxels between corrected t-maps and SLF maps was calculated per hemisphere. The corresponding voxels were then normalized for the number of significant voxels in the corrected t-maps [(Nr of overlapping voxels per SLF tract/ Nr of significant voxels in the corrected t-maps in the respective hemisphere)*100].

Data availability

Raw iEEG and patients' MRI and CT data cannot be shared due to ethics committee restrictions. Intermediate as well as final processed data that support the findings of this study are available from the corresponding author (T.S.M.) upon request. The diffusion MRI data used in this study are available in the HCP database https://www.humanconnectome.org/study/hcp-young-adult/document/1200-subjects-data-release.

Code Availability

The custom codes used to generate the figures and statistics are available from the lead contact (T.S.M.) upon request.

References

1. Carrasco, M. Visual attention: the past 25 years. *Vision Res.* **51**, 1484–1525 (2011).
2. Zhaoping, L. From the optic tectum to the primary visual cortex: migration through evolution of the saliency map for exogenous attentional guidance. *Curr. Opin. Neurobiol.* **40**, 94–102 (2016).
3. Lev-Ari, T., Zahar, Y., Agarwal, A. & Gutfreund, Y. Behavioral and neuronal study of inhibition of return in barn owls. *Sci. Rep.* **10**, 7267 (2020).
4. Gabay, S., Leibovich, T., Ben-Simon, A., Henik, A. & Segev, R. Inhibition of return in the archer fish. *Nat. Commun.* **4**, 1657 (2013).
5. Patel, G. H. *et al.* Functional evolution of new and expanded attention networks in humans. *Proc. Natl. Acad. Sci. U. S. A.* **112**, 9454–9459 (2015).
6. Lupiáñez, J. Inhibition of return. in *Attention and Time* (eds. Nobre, A. C. & Coulle, J. T.) 17–34 (Oxford University Press, 2010).
7. Posner, M. I. & Cohen, Y. Components of visual orienting. in *Attention and performance X: Control of language processes* (eds. Bouma, H. & Bouwhuis, D.) 531–56. (Erlbaum, 1984).
8. Chica, A. B., Martín-Arévalo, E., Botta, F. & Lupiánez, J. The Spatial Orienting paradigm: How to design and interpret spatial attention experiments. *Neurosci. Biobehav. Rev.* **40**, 35–51 (2014).
9. Shallice, T. A Theory of Consciousness: Chronometric Explorations of Mind . Michael I. Posner. Erlbaum, Hillsdale, N.J., 1978 (distributor, Halsted [Wiley], New York). xvi, 272 pp., illus. $14.95. The Experimental Psychology Series. *Science* **204**, 827–827 (1979).
10. Lupiáñez, J., Klein, R. M. & Bartolomeo, P. Inhibition of return: Twenty years after. *Cogn. Neuropsychol.* **23**, 1003–1014 (2006).
11. Martín-Arévalo, E., Chica, A. B. & Lupiáñez, J. No single electrophysiological marker for facilitation and inhibition of return: A review. *Behav. Brain Res.* **300**, 1–10 (2016).

12. VanRullen, R. Visual Saliency and Spike Timing in the Ventral Visual Pathway. *Neurobiology of Attention* 272–278 Preprint at https://doi.org/10.1016/b978-012375731-9/50049-5 (2005).
13. Moore, T. & Zirnsak, M. Neural Mechanisms of Selective Visual Attention. *Annu. Rev. Psychol.* **68**, 47–72 (2017).
14. Burrows, B. E. & Moore, T. Influence and limitations of popout in the selection of salient visual stimuli by area V4 neurons. *J. Neurosci.* **29**, 15169–15177 (2009).
15. Wang, F., Chen, M., Yan, Y., Zhaoping, L. & Li, W. Modulation of Neuronal Responses by Exogenous Attention in Macaque Primary Visual Cortex. *J. Neurosci.* **35**, 13419–13429 (2015).
16. Hegdé, J. & Felleman, D. J. How selective are V1 cells for pop-out stimuli? *J. Neurosci.* **23**, 9968–9980 (2003).
17. Itti, L. & Koch, C. Computational modelling of visual attention. *Nat. Rev. Neurosci.* **2**, 194–203 (2001).
18. Balan, P. F. & Gottlieb, J. Integration of exogenous input into a dynamic salience map revealed by perturbing attention. *J. Neurosci.* **26**, 9239–9249 (2006).
19. Corbetta, M. & Shulman, G. L. Control of goal-directed and stimulus-driven attention in the brain. *Nat. Rev. Neurosci.* **3**, 201–215 (2002).
20. Goldberg, M. E., Bisley, J. W., Powell, K. D. & Gottlieb, J. Saccades, salience and attention: the role of the lateral intraparietal area in visual behavior. *Prog. Brain Res.* **155**, 157–175 (2006).
21. Soltani, A. & Koch, C. Visual saliency computations: mechanisms, constraints, and the effect of feedback. *J. Neurosci.* **30**, 12831–12843 (2010).
22. Buschman, T. J. & Miller, E. K. Top-down versus bottom-up control of attention in the prefrontal and posterior parietal cortices. *Science* **315**, 1860–1862 (2007).
23. Moore, T. & Armstrong, K. M. Selective gating of visual signals by microstimulation of frontal cortex. *Nature* **421**, 370–373 (2003).

24. Thompson, K. G. & Bichot, N. P. A visual salience map in the primate frontal eye field. *Prog. Brain Res.* **147**, 251–262 (2005).
25. Veale, R., Hafed, Z. M. & Yoshida, M. How is visual salience computed in the brain? Insights from behaviour, neurobiology and modelling. *Philos. Trans. R. Soc. Lond. B Biol. Sci.* **372**, (2017).
26. Mirpour, K., Arcizet, F., Ong, W. S. & Bisley, J. W. Been there, seen that: a neural mechanism for performing efficient visual search. *J. Neurophysiol.* **102**, 3481–3491 (2009).
27. Mirpour, K., Bolandnazar, Z. & Bisley, J. W. Neurons in FEF Keep Track of Items That Have Been Previously Fixated in Free Viewing Visual Search. *J. Neurosci.* **39**, 2114–2124 (2019).
28. Bourgeois, A., Chica, A. B., Valero-Cabre, A. & Bartolomeo, P. Cortical control of inhibition of return: Causal evidence for task-dependent modulations by dorsal and ventral parietal regions. *Cortex* **49**, 2229–2238 (2013).
29. Bourgeois, A., Chica, A. B., Valero-Cabre, A. & Bartolomeo, P. Cortical control of Inhibition of Return: Exploring the causal contributions of the left parietal cortex. *Cortex* **49**, 2927–2934 (2013).
30. Ro, T., Farnè, A. & Chang, E. Inhibition of return and the human frontal eye fields. *Exp. Brain Res.* **150**, 290–296 (2003).
31. Sapir, A., Soroker, N., Berger, A. & Henik, A. Inhibition of return in spatial attention: direct evidence for collicular generation. *Nat. Neurosci.* **2**, 1053–1054 (1999).
32. Dorris, M. C., Klein, R. M., Everling, S. & Munoz, D. P. Contribution of the primate superior colliculus to inhibition of return. *J. Cogn. Neurosci.* **14**, 1256–1263 (2002).
33. Bourgeois, A., Chica, A. B., Migliaccio, R., Thiebaut de Schotten, M. & Bartolomeo, P. Cortical control of inhibition of return: evidence from patients with inferior parietal damage and visual neglect. *Neuropsychologia* **50**, 800–809 (2012).
34. Siéroff, E., Decaix, C., Chokron, S. & Bartolomeo, P. Impaired orienting of attention in left unilateral neglect: A componential analysis. *Neuropsychology* **21**, 94–113 (2007).

35. Thiebaut de Schotten, M. *et al.* Direct evidence for a parietal-frontal pathway subserving spatial awareness in humans. *Science* **309**, 2226–2228 (2005).

36. Lupiáñez, J., Martín-Arévalo, E. & Chica, A. B. Is Inhibition of Return due to attentional disengagement or to a detection cost? The Detection Cost Theory of IOR. *Psicologica: International Journal of Methodology and Experimental Psychology* **34**, 221–252 (2013).

37. Berlucchi, G. Inhibition of return: a phenomenon in search of a mechanism and a better name. *Cogn. Neuropsychol.* **23**, 1065–1074 (2006).

38. Bartolomeo, P. & Lupiáñez, J. Inhibitory after-effects in spatial processing: Experimental and theoretical issues on Inhibition of Return. in 80 (Psychology Press, 2006).

39. Klein, R. M. Inhibition of return. *Trends Cogn. Sci.* **4**, 138–147 (2000).

40. Klein, R. Inhibitory tagging system facilitates visual search. *Nature* **334**, 430–431 (1988).

41. Bartolomeo, P. & Seidel Malkinson, T. Hemispheric lateralization of attention processes in the human brain. *Curr Opin Psychol* **29**, 90–96 (2019).

42. Seidel Malkinson, T. & Bartolomeo, P. Fronto-parietal organization for response times in inhibition of return: The FORTIOR model. *Cortex* **102**, 176–192 (2018).

43. Klein, R. M. & Redden, R. S. Two “inhibitions of return” bias orienting differently. *Spatial biases in perception and cognition* 295–306 (2018).

44. Lim, A., Janssen, S. M. J. & Satel, J. Exploring the temporal dynamics of inhibition of return using steady-state visual evoked potentials. *Cogn. Affect. Behav. Neurosci.* **20**, 1349–1364 (2020).

45. Dukewich, K. R. Reconceptualizing inhibition of return as. *Psychon. Bull. Rev.* **16**, 238–251 (2009).

46. Redden, R. S., MacInnes, W. J. & Klein, R. M. Inhibition of return: An information processing theory of its natures and significance. *Cortex* (2020).

47. Lupiáñez, J. Inhibition of return. *Attention and time* 17–34 (2010).

48. Kahneman, D., Treisman, A. & Gibbs, B. J. The reviewing of object files: object-specific integration of information. *Cogn. Psychol.* **24**, 175–219 (1992).

49. Huntenburg, J. M., Bazin, P.-L. & Margulies, D. S. Large-Scale Gradients in Human Cortical Organization. *Trends Cogn. Sci.* **22**, 21–31 (2018).

50. Gao, R., van den Brink, R. L., Pfeffer, T. & Voytek, B. Neuronal timescales are functionally dynamic and shaped by cortical microarchitecture. *Elife* **9**, (2020).

51. Margulies, D. S. *et al.* Situating the default-mode network along a principal gradient of macroscale cortical organization. *Proc. Natl. Acad. Sci. U. S. A.* **113**, 12574–12579 (2016).

52. Sydnor, V. J. *et al.* Neurodevelopment of the association cortices: Patterns, mechanisms, and implications for psychopathology. *Neuron* **109**, 2820–2846 (2021).

53. Mesulam, M. M. *Principles of behavioral and cognitive neurology*. (Oxford University Press, 2000).

54. Poffenberger, A. T. Reaction time to retinal stimulation: with special reference to the time lost in conduction through nerve centers. (1912).

55. Anzola, G. P., Bertoloni, G., Buchtel, H. A. & Rizzolatti, G. Spatial compatibility and anatomical factors in simple and choice reaction time. *Neuropsychologia* **15**, 295–302 (1977).

56. Buschman, T. J. & Kastner, S. From Behavior to Neural Dynamics: An Integrated Theory of Attention. *Neuron* **88**, 127–144 (2015).

57. Vu, A. T. *et al.* High resolution whole brain diffusion imaging at 7T for the Human Connectome Project. *Neuroimage* **122**, 318–331 (2015).

58. Thiebaut de Schotten, M. *et al.* A lateralized brain network for visuospatial attention. *Nat. Neurosci.* **14**, 1245–1246 (2011).

59. Bartolomeo, Thiebaut de Schotten, M. & Chica, A. B. Brain networks of visuospatial attention and their disruption in visual neglect. *Front. Hum. Neurosci.* **6**, 110 (2012).

60. Michel, R. & Busch, N. A. No evidence for rhythmic sampling in inhibition of return. *Atten. Percept. Psychophys.* (2023) doi:10.3758/s13414-023-02745-x.
61. Hasson, U., Yang, E., Vallines, I., Heeger, D. J. & Rubin, N. A hierarchy of temporal receptive windows in human cortex. *J. Neurosci.* **28**, 2539–2550 (2008).
62. Murray, J. D. *et al.* A hierarchy of intrinsic timescales across primate cortex. *Nat. Neurosci.* **17**, 1661–1663 (2014).
63. Honey, C. J. *et al.* Slow cortical dynamics and the accumulation of information over long timescales. *Neuron* **76**, 423–434 (2012).
64. Himberger, K. D., Chien, H.-Y. & Honey, C. J. Principles of Temporal Processing Across the Cortical Hierarchy. *Neuroscience* **389**, 161–174 (2018).
65. Kiebel, S. J., Daunizeau, J. & Friston, K. J. A hierarchy of time-scales and the brain. *PLoS Comput. Biol.* **4**, e1000209 (2008).
66. Rosenke, M., van Hoof, R., van den Hurk, J., Grill-Spector, K. & Goebel, R. A Probabilistic Functional Atlas of Human Occipito-Temporal Visual Cortex. *Cereb. Cortex* **31**, 603–619 (2021).
67. Vernet, M., Quentin, R., Chanes, L., Mitsumasu, A. & Valero-Cabré, A. Frontal eye field, where art thou? Anatomy, function, and non-invasive manipulation of frontal regions involved in eye movements and associated cognitive operations. *Front. Integr. Neurosci.* **8**, 66 (2014).
68. Kirchner, H., Barbeau, E. J., Thorpe, S. J., Régis, J. & Liégeois-Chauvel, C. Ultra-rapid sensory responses in the human frontal eye field region. *J. Neurosci.* **29**, 7599–7606 (2009).
69. Helfrich, R. F. *et al.* Neural Mechanisms of Sustained Attention Are Rhythmic. *Neuron* **99**, 854-865.e5 (2018).
70. Taylor, T. L. & Klein, R. M. Visual and motor effects in inhibition of return. *J. Exp. Psychol. Hum. Percept. Perform.* **26**, 1639–1656 (2000).
71. Fiebelkorn, I. C. & Kastner, S. A Rhythmic Theory of Attention. *Trends Cogn. Sci.* **23**, 87–101 (2019).

72. Mars, R. B. *et al.* Connectivity-based subdivisions of the human right "temporoparietal junction area": evidence for different areas participating in different cortical networks. *Cereb. Cortex* **22**, 1894–1903 (2012).

73. Hattori, T. *et al.* Structural connectivity in spatial attention network: reconstruction from left hemispatial neglect. *Brain Imaging Behav.* **12**, 309–323 (2018).

74. Sani, I. *et al.* The human endogenous attentional control network includes a ventro-temporal cortical node. *Nat. Commun.* **12**, 360 (2021).

75. Stemmann, H. & Freiwald, W. A. Evidence for an attentional priority map in inferotemporal cortex. *Proc. Natl. Acad. Sci. U. S. A.* **116**, 23797–23805 (2019).

76. Szczepanski, S. M. & Kastner, S. Shifting attentional priorities: control of spatial attention through hemispheric competition. *Journal of Neuroscience* **33**, 5411–5421 (2013).

77. Chica, A. B., Bourgeois, A. & Bartolomeo, P. On the role of the ventral attention system in spatial orienting. *Front. Hum. Neurosci.* **8**, 235 (2014).

78. Stigliani, A., Jeska, B. & Grill-Spector, K. Encoding model of temporal processing in human visual cortex. *Proc. Natl. Acad. Sci. U. S. A.* **114**, E11047–E11056 (2017).

79. Zhou, J., Benson, N. C., Kay, K. N. & Winawer, J. Compressive Temporal Summation in Human Visual Cortex. *J. Neurosci.* **38**, 691–709 (2018).

80. Wasmuht, D. F., Spaak, E., Buschman, T. J., Miller, E. K. & Stokes, M. G. Intrinsic neuronal dynamics predict distinct functional roles during working memory. *Nat. Commun.* **9**, 3499 (2018).

81. Kim, R. & Sejnowski, T. J. Strong inhibitory signaling underlies stable temporal dynamics and working memory in spiking neural networks. *Nat. Neurosci.* **24**, 129–139 (2021).

82. Krüger, H. M., MacInnes, W. J. & Hunt, A. R. Perceptual merging contributes to cueing effects. *J. Vis.* **14**, (2014).

83. Bartolomeo, P., Chokron, S. & Siéroff, E. Facilitation instead of inhibition for repeated right-sided events in left neglect. *Neuroreport* **10**, 3353–3357 (1999).
84. Chica, A. B., Bartolomeo, P. & Valero-Cabré, A. Dorsal and ventral parietal contributions to spatial orienting in the human brain. *Journal of Neuroscience* **31**, 8143–8149 (2011).
85. Mahjoory, K., Schoffelen, J.-M., Keitel, A. & Gross, J. The frequency gradient of human resting-state brain oscillations follows cortical hierarchies. *Elife* **9**, (2020).
86. Lachaux, J. P., Rudrauf, D. & Kahane, P. Intracranial EEG and human brain mapping. *J. Physiol. Paris* **97**, 613–628 (2003).
87. Parvizi, J. & Kastner, S. Promises and limitations of human intracranial electroencephalography. *Nat. Neurosci.* **21**, 474–483 (2018).
88. Mukamel, R. & Fried, I. Human intracranial recordings and cognitive neuroscience. *Annu. Rev. Psychol.* **63**, 511–537 (2012).
89. Krauzlis, R. J., Wang, L., Yu, G. & Katz, L. N. What is attention? *Wiley Interdiscip. Rev. Cogn. Sci.* e1570 (2021).
90. Pérez-García, F., Lehongre, K., Bardinet, E., Jannin, P. & Fernandez-Vidal, S. Automatic Segmentation Of Depth Electrodes Implanted In Epileptic Patients: A Modular Tool Adaptable To Multicentric Protocols. **56**, (2015).
91. Desikan, R. S. *et al.* An automated labeling system for subdividing the human cerebral cortex on MRI scans into gyral based regions of interest. *Neuroimage* **31**, 968–980 (2006).
92. Team, Jasp. *JASP (Version 0.14.1)[Computer software]*. (2020).
93. Ray, S. & Maunsell, J. H. R. Different origins of gamma rhythm and high-gamma activity in macaque visual cortex. *PLoS Biol.* **9**, e1000610 (2011).
94. Helfrich, R. F. & Knight, R. T. Chapter 3 - Cognitive neurophysiology of the prefrontal cortex. in *Handbook of Clinical Neurology* (eds. D'Esposito, M. & Grafman, J. H.) vol. 163 35–59 (Elsevier, 2019).

95. Kodinariya, T. M. & Makwana, P. R. Review on determining number of Cluster in K-Means Clustering. *Aquat. Microb. Ecol.* **1**, 90–95 (2013).

96. Friston, K. J., Ashburner, J. T., Kiebel, S. J., Nichols, T. E. & Penny, W. D. *Statistical parametric mapping: The analysis of functional brain images: The analysis of functional brain images*. (Academic Press, 2010).

97. Golesorkhi, M., Tumati, S., Gomez-Pilar, J., Stamatakis, E. A. & Northoff, G. Time meets space – brain dynamics drive spatial topography. 2020.06.11.106476 (2020) doi:10.1101/2020.06.11.106476.

98. van den Bergh, D. *et al.* A tutorial on conducting and interpreting a Bayesian ANOVA in JASP. *PsyArXiv* (2019) doi:10.31234/osf.io/spreb.

Acknowledgments

We would like to thank Pietro Avanzini, Danilo Bzdok, Florence Bouhali, and the PICNIC lab at the Paris Brain Institute (ICM) for invaluable discussions and assistance. This work was funded by Israel Science Foundation postdoctoral fellowship number 57/15 (TSM), Marie Sklodowska Curie fellowship 702577-DynamAtt (TSM), and Agence Nationale de la Recherche BRANDY grant ANR-16-CE37-0005 (TSM, DJB, VN, SFV, PB).

Author contributions Statement

Conceptualization: TSM, DJB, PB

Data curation: KL

Formal analysis: TSM

Methodology: TSM, JDS, BCK, JL

Investigation: TSM, DJB

Visualization: TSM, BCK

Funding acquisition: TSM, PB

Project administration: TSM

Resources: KL, SFV, VN, CA, VL, DSM

Software: TSM, DJB, AB, JDS, SFV, DSM

Supervision: PB

Writing – original draft: TSM

Writing – review & editing: TSM, DJB, BCK, AB, KL, SFV, VN, CA, VL, DSM, JDS, PB

Competing interests Statement

Authors declare that they have no competing interests.

Tables

Patient #	Gender	Handedness	Number of electrodes (total 243)	Total number of contacts per patient (total 1,884)	Implanted hemisphere
1	M	R	10	104	RH
2	F	R	12	96	LH+RH
3	M	R	12	82	RH
4	F	R	10	82	LH
5	M	R	9	58	RH
6	M	R	11	90	LH
7	F	R	9	54	LH

8	M	R	9	63	LH
9	M	L+R	10	44	LH+RH
10	M	R	9	48	LH
11	F	R	10	88	LH
12	F	R	10	58	RH
13	F	R	8	76	LH
14	F	R	7	62	LH
15	M	R	10	70	LH+RH
16	F	R	9	78	LH+RH
17	F	R	8	61	RH
18	M	R	7	65	RH
19	M	R	7	31	RH
20	M	R	8	53	LH
21	F	L	8	56	LH
22	M	L	5	48	LH
23	F	R	8	63	RH
24	F	R	9	77	RH
25	F	R	9	67	LH+RH
26	F	R	9	54	LH+RH
27	F	R	12	93	RH
28	M	R	11	62	LH
Mean	**54% F**	**89% R**	**9.1**	**67.3**	**57% RH**

Table 1 – Implanted patients demographic details

Region name	Responsive Electrodes N	Cluster 1 N	Cluster 2 N	Cluster 3 N
Banks superior temporal sulcus	9	1	4	1
Caudal anterior-cingulate cortex	3	0	0	0
Caudal middle frontal gyrus	12	2	2	1
Entorhinal cortex	6	0	0	0
Fusiform gyrus Posterior	33	7	8	3
Fusiform gyrus Med	14	2	2	0
Fusiform gyrus Anterior	10	0	0	0
Inferior parietal cortex	51	19	14	5
Inferior temporal gyrus Posterior	28	1	8	1
Inferior temporal gyrus Middle	14	0	3	0
Inferior temporal gyrus Antrior	13	0	0	0

Lateral occipital cortex	20	6	5	2
Lingual gyrus	17	1	0	3
Medial orbital frontal cortex	4	0	0	0
Middle temporal gyrus Posterior	37	10	12	1
Middle temporal gyrus Middle	19	0	2	0
Middle temporal gyrus Anterior	35	0	0	0
Parahippocampal gyrus	8	0	0	0
Paracentral lobule	1	0	0	0
Pars opercularis	8	0	0	1
Pars orbitalis	36	0	0	0
Pars triangularis	9	0	0	4
Pericalcarine cortex	1	0	0	0
Postcentral gyrus dorsal	1	0	0	0
Postcentral gyrus ventral	1	0	0	0
Posterior-cingulate cortex	3	0	1	1
Precentral gyrus dorsal	16	6	3	4
Precentral gyrus ventral	5	0	3	1
Precuneus cortex	1	0	0	0
Rostral middle frontal gyrus	16	0	4	2
Superior frontal gyrus	46	0	8	16
Superior parietal cortex	10	1	3	1
Superior temporal gyrus Posterior	19	2	1	3
Superior temporal gyrus Middle	17	0	0	0
Superior temporal gyrus Anterior	13	0	0	3
Supramarginal gyrus	22	0	3	9
Temporal pole	14	0	0	0
White matter	49	10	10	5
hippocampus	18	0	1	0
amygdala	5	0	0	0

Table 2 – Responsive electrodes localization according to the Desikan-Killiany-Tourville atlas [89]

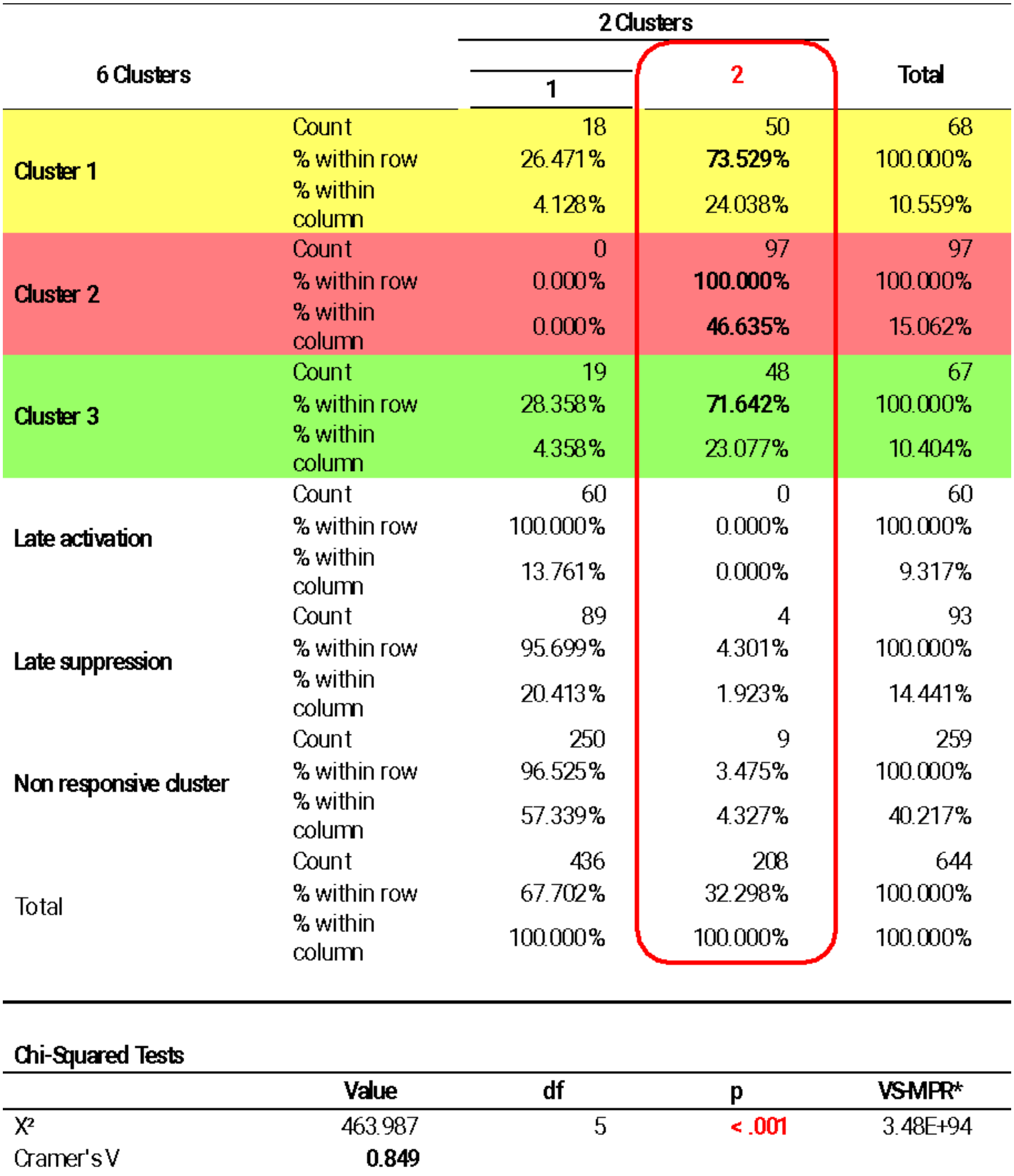

6 Clusters		2 Clusters		Total
		1	2	
Cluster 1	Count	18	50	68
	% within row	26.471%	**73.529%**	100.000%
	% within column	4.128%	24.038%	10.559%
Cluster 2	Count	0	97	97
	% within row	0.000%	**100.000%**	100.000%
	% within column	0.000%	**46.635%**	15.062%
Cluster 3	Count	19	48	67
	% within row	28.358%	**71.642%**	100.000%
	% within column	4.358%	23.077%	10.404%
Late activation	Count	60	0	60
	% within row	100.000%	0.000%	100.000%
	% within column	13.761%	0.000%	9.317%
Late suppression	Count	89	4	93
	% within row	95.699%	4.301%	100.000%
	% within column	20.413%	1.923%	14.441%
Non responsive cluster	Count	250	9	259
	% within row	96.525%	3.475%	100.000%
	% within column	57.339%	4.327%	40.217%
Total	Count	436	208	644
	% within row	67.702%	32.298%	100.000%
	% within column	100.000%	100.000%	100.000%

Chi-Squared Tests

	Value	df	p	VS-MPR*
X^2	463.987	5	< .001	3.48E+94
Cramer's V	**0.849**			

		3 Clusters			
6 Clusters		**1**	**2**	**3**	**Total**
Cluster 1	Count	4	48	16	68
	% within row	5.882%	**70.588%**	23.529%	100.000%
	% within column	3.419%	25.263%	4.748%	10.559%
Cluster 2	Count	0	94	3	97
	% within row	0.000%	**96.907%**	3.093%	100.000%
	% within column	0.000%	**49.474%**	0.890%	15.062%
Cluster 3	Count	18	45	4	67
	% within row	26.866%	**67.164%**	5.970%	100.000%
	% within column	15.385%	23.684%	1.187%	10.404%
Late activation	Count	53	0	7	60
	% within row	88.333%	0.000%	11.667%	100.000%
	% within column	45.299%	0.000%	2.077%	9.317%
Late suppression	Count	0	0	93	93
	% within row	0.000%	0.000%	100.000%	100.000%
	% within column	0.000%	0.000%	27.596%	14.441%
Non responsive Cluster	Count	42	3	214	259
	% within row	16.216%	1.158%	82.625%	100.000%
	% within column	35.897%	1.579%	63.501%	40.217%
Total	Count	117	190	337	644
	% within row	18.168%	29.503%	52.329%	100.000%
	% within column	100.000%	100.000%	100.000%	100.000%

Chi-Squared Tests

	Value	df	p	VS-MPR*
X^2	730.26	10	< .001	5E+146
Cramer's V	**0.753**			

		4 Clusters				
6 Clusters		**1**	**2**	**3**	**4**	**Total**
Cluster 1	Count	0	5	0	63	68
	% within row	0.000%	7.353%	0.000%	**92.647%**	100.000%
	% within column	0.000%	3.623%	0.000%	**88.732%**	10.559%
Cluster 2	Count	0	86	4	7	97
	% within row	0.000%	**88.660%**	4.124%	7.216%	100.000%
	% within column	0.000%	**62.319%**	1.220%	9.859%	15.062%
Cluster 3	Count	17	47	3	0	67
	% within row	25.373%	**70.149%**	4.478%	0.000%	100.000%
	% within column	15.888%	34.058%	0.915%	0.000%	10.404%
Late activation	Count	53	0	7	0	60
	% within row	88.333%	0.000%	11.667%	0.000%	100.000%
	% within column	49.533%	0.000%	2.134%	0.000%	9.317%
Late suppression	Count	0	0	92	1	93
	% within row	0.000%	0.000%	98.925%	1.075%	100.000%
	% within column	0.000%	0.000%	28.049%	1.408%	14.441%
Non responsive Cluster	Count	37	0	222	0	259
	% within row	14.286%	0.000%	85.714%	0.000%	100.000%
	% within column	34.579%	0.000%	67.683%	0.000%	40.217%
Total	Count	107	138	328	71	644
	% within row	16.615%	21.429%	50.932%	11.025%	100.000%
	% within column	100.000%	100.000%	100.000%	100.000%	100.000%

Chi-Squared Tests

	Value	df	p	VS-MPR*
X^2	1295.54	15	< .001	1E+263
Cramer's V	**0.819**			

		5 Clusters					
6 Clusters		**1**	**2**	**3**	**4**	**5**	**Total**
Cluster 1	Count	0	0	2	1	65	68
	% within row	0.000%	0.000%	2.941%	1.471%	**95.588%**	100.000%
	% within column	0.000%	0.000%	1.852%	1.220%	**92.857%**	10.559%
Cluster 2	Count	12	1	0	81	3	97
	% within row	12.371%	1.031%	0.000%	**83.505%**	3.093%	100.000%
	% within column	18.462%	0.313%	0.000%	**98.780%**	4.286%	15.062%
Cluster 3	Count	53	1	11	0	2	67
	% within row	**79.104%**	1.493%	16.418%	0.000%	2.985%	100.000%
	% within column	**81.538%**	0.313%	10.185%	0.000%	2.857%	10.404%
Late activation	Count	0	6	54	0	0	60
	% within row	0.000%	10.000%	90.000%	0.000%	0.000%	100.000%
	% within column	0.000%	1.881%	50.000%	0.000%	0.000%	9.317%
Late suppression	Count	0	93	0	0	0	93
	% within row	0.000%	100.000%	0.000%	0.000%	0.000%	100.000%
	% within column	0.000%	29.154%	0.000%	0.000%	0.000%	14.441%
Non responsive Cluster	Count	0	218	41	0	0	259
	% within row	0.000%	84.170%	15.830%	0.000%	0.000%	100.000%
	% within column	0.000%	68.339%	37.963%	0.000%	0.000%	40.217%
Total	Count	65	319	108	82	70	644
	% within row	10.093%	49.534%	16.770%	12.733%	10.870%	100.000%
	% within column	100.000%	100.000%	100.000%	100.000%	100.000%	100.000%

Chi-Squared Tests

	Value	**df**	**p**	**VS-MPR***
X^2	1789.51	20	< .001	∞
Cramer's V	**0.833**			

		7 Clusters							
6 Clusters		**1**	**2**	**3**	**4**	**5**	**6**	**7**	**Total**
Cluster 1	Count	0	0	66	2	0	0	0	68
	% within row	0.000%	0.000%	**97.059%**	2.941%	0.000%	0.000%	0.000%	100.000%
	% within column	0.000%	0.000%	**95.652%**	2.299%	0.000%	0.000%	0.000%	10.559%
Cluster 2	Count	0	1	0	85	9	2	0	97
	% within row	0.000%	1.031%	0.000%	**87.629%**	9.278%	2.062%	0.000%	100.000%
	% within column	0.000%	1.667%	0.000%	**97.701%**	14.516%	0.952%	0.000%	15.062%
Cluster 3	Count	10	0	2	0	53	2	0	67
	% within row	14.925%	0.000%	2.985%	0.000%	**79.104%**	2.985%	0.000%	100.000%
	% within column	9.434%	0.000%	2.899%	0.000%	**85.484%**	0.952%	0.000%	10.404%
Late activation	Count	51	1	0	0	0	1	7	60
	% within row	85.000%	1.667%	0.000%	0.000%	0.000%	1.667%	11.667%	100.000%
	% within column	48.113%	1.667%	0.000%	0.000%	0.000%	0.476%	14.000%	9.317%
Late suppression	Count	0	55	1	0	0	19	18	93
	% within row	0.000%	59.140%	1.075%	0.000%	0.000%	20.430%	19.355%	100.000%
	% within column	0.000%	91.667%	1.449%	0.000%	0.000%	9.048%	36.000%	14.441%
Non responsive Cluster	Count	45	3	0	0	0	186	25	259
	% within row	17.375%	1.158%	0.000%	0.000%	0.000%	71.815%	9.653%	100.000%
	% within column	42.453%	5.000%	0.000%	0.000%	0.000%	88.571%	50.000%	40.217%
Total	Count	106	60	69	87	62	210	50	644
	% within row	16.460%	9.317%	10.714%	13.509%	9.627%	32.609%	7.764%	100.000%
	% within column	100.000%	100.000%	100.000%	100.000%	100.000%	100.000%	100.000%	100.000%

Chi-Squared Tests

	Value	df	p	VS-MPR*
X^2	2128.58	30	< .001	∞
Cramer's V	**0.813**			

6 Clusters		8 Clusters								
		1	2	3	4	5	6	7	8	Total
Cluster 1	Count	0	0	0	0	62	0	0	6	68
	% within row	0.000%	0.000%	0.000%	0.000%	**91.176%**	0.000%	0.000%	8.824%	100.000%
	% within column	0.000%	0.000%	0.000%	0.000%	**98.413%**	0.000%	0.000%	6.186%	10.559%
Cluster 2	Count	1	1	0	2	0	2	0	91	97
	% within row	1.031%	1.031%	0.000%	2.062%	0.000%	2.062%	0.000%	**93.814%**	100.000%
	% within column	1.852%	0.952%	0.000%	0.962%	0.000%	9.091%	0.000%	**93.814%**	15.062%
Cluster 3	Count	53	0	1	13	0	0	0	0	67
	% within row	**79.104%**	0.000%	1.493%	19.403%	0.000%	0.000%	0.000%	0.000%	100.000%
	% within column	**98.148%**	0.000%	1.163%	6.250%	0.000%	0.000%	0.000%	0.000%	10.404%
Late activation	Count	0	0	60	0	0	0	0	0	60
	% within row	0.000%	0.000%	100.000%	0.000%	0.000%	0.000%	0.000%	0.000%	100.000%
	% within column	0.000%	0.000%	69.767%	0.000%	0.000%	0.000%	0.000%	0.000%	9.317%
Late suppression	Count	0	85	0	4	1	3	0	0	93
	% within row	0.000%	91.398%	0.000%	4.301%	1.075%	3.226%	0.000%	0.000%	100.000%
	% within column	0.000%	80.952%	0.000%	1.923%	1.587%	13.636%	0.000%	0.000%	14.441%
Non responsive Cluster	Count	0	19	25	189	0	17	9	0	259
	% within row	0.000%	7.336%	9.653%	72.973%	0.000%	6.564%	3.475%	0.000%	100.000%
	% within column	0.000%	18.095%	29.070%	90.865%	0.000%	77.273%	100.000%	0.000%	40.217%
Total	Count	54	105	86	208	63	22	9	97	644
	% within row	8.385%	16.304%	13.354%	32.298%	9.783%	3.416%	1.398%	15.062%	100.000%
	% within column	100.000%	100.000%	100.000%	100.000%	100.000%	100.000%	100.000%	100.000%	100.000%

Chi-Squared Tests

	Value	df	p	VS-MPR*
X^2	2451.55	35	< .001	∞
Cramer's V	**0.873**			

Table S1 – Cluster stability across 2-8 k-cluster solutions. Contingency tables analyses showing a strong significant correspondence (all p<0.001, all Cramer's V ≥0.75) between the assignments of contacts to clusters in the 6-cluster solution and the other k-cluster solutions (Top table: *k*=2, Bottom table: *k*=8). The Contingency tables show the distribution of contacts belonging to each of the three further analyzed clusters (Cluster 1- yellow, Cluster 2 – red, Cluster 3 – green) in each of the other solutions' clusters (% within row), and the composition of each of the other solutions' clusters (% within column). A k-solution cluster was marked as stable (colored frame) if the main group of contacts composing it could be mapped to one of the three further analyzed clusters, which in turn shared most of its contacts with that cluster.

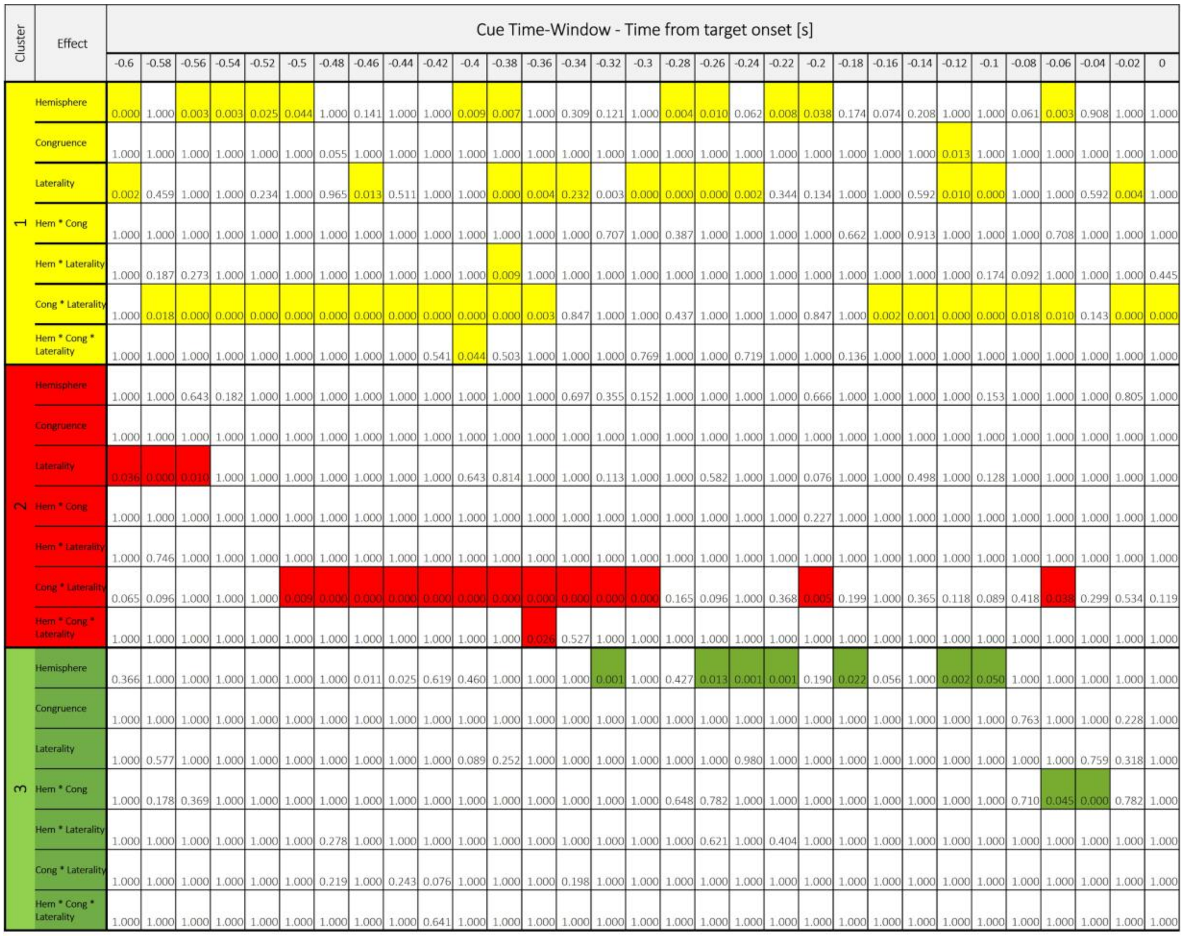

Cluster	Effect	Cue Time-Window - Time from target onset [s]																													
		-0.6	-0.58	-0.56	-0.54	-0.52	-0.5	-0.48	-0.46	-0.44	-0.42	-0.4	-0.38	-0.36	-0.34	-0.32	-0.3	-0.28	-0.26	-0.24	-0.22	-0.2	-0.18	-0.16	-0.14	-0.12	-0.1	-0.08	-0.06	-0.04	-0.02	0
1	Hemisphere	0.000	1.000	0.003	0.003	0.025	0.044	1.000	0.141	1.000	1.000	0.009	0.007	1.000	0.309	0.121	1.000	0.004	0.010	0.062	0.008	0.038	0.174	0.074	0.208	1.000	1.000	0.061	0.003	0.908	1.000	1.000
	Congruence	1.000	1.000	1.000	1.000	1.000	1.000	0.055	1.000	1.000	1.000	1.000	1.000	1.000	1.000	1.000	1.000	1.000	1.000	1.000	1.000	1.000	1.000	1.000	1.000	0.013	1.000	1.000	1.000	1.000	1.000	1.000
	Laterality	0.002	0.459	1.000	1.000	0.234	1.000	0.965	0.013	0.511	1.000	1.000	0.000	0.004	0.232	0.003	0.000	0.000	0.000	0.002	0.344	0.134	1.000	1.000	0.592	0.010	0.000	1.000	1.000	0.592	0.004	1.000
	Hem * Cong	1.000	1.000	1.000	1.000	1.000	1.000	1.000	1.000	1.000	1.000	1.000	1.000	1.000	1.000	0.707	1.000	0.387	1.000	1.000	1.000	1.000	0.662	1.000	0.913	1.000	1.000	1.000	0.708	1.000	1.000	1.000
	Hem * Laterality	1.000	0.187	0.273	1.000	1.000	1.000	1.000	1.000	1.000	1.000	1.000	0.009	1.000	1.000	1.000	1.000	1.000	1.000	1.000	1.000	1.000	1.000	1.000	1.000	1.000	0.174	0.092	1.000	1.000	1.000	0.445
	Cong * Laterality	1.000	0.018	0.000	0.000	0.000	0.000	0.000	0.000	0.000	0.000	0.000	0.000	0.003	0.847	1.000	1.000	0.437	1.000	1.000	1.000	0.847	1.000	0.002	0.001	0.000	0.000	0.018	0.010	0.143	0.000	0.000
	Hem * Cong * Laterality	1.000	1.000	1.000	1.000	1.000	1.000	1.000	1.000	1.000	0.541	0.044	0.503	1.000	1.000	1.000	0.769	1.000	1.000	0.719	1.000	1.000	0.136	1.000	1.000	1.000	1.000	1.000	1.000	1.000	1.000	1.000
2	Hemisphere	1.000	1.000	0.643	0.182	1.000	1.000	1.000	1.000	1.000	1.000	1.000	1.000	1.000	0.697	0.355	0.152	1.000	1.000	1.000	1.000	0.666	1.000	1.000	1.000	1.000	0.153	1.000	1.000	1.000	0.805	1.000
	Congruence	1.000	1.000	1.000	1.000	1.000	1.000	1.000	1.000	1.000	1.000	1.000	1.000	1.000	1.000	1.000	1.000	1.000	1.000	1.000	1.000	1.000	1.000	1.000	1.000	1.000	1.000	1.000	1.000	1.000	1.000	1.000
	Laterality	0.036	0.000	0.010	1.000	1.000	1.000	1.000	1.000	1.000	1.000	0.643	0.814	1.000	1.000	0.113	1.000	1.000	0.582	1.000	1.000	0.076	1.000	1.000	0.498	1.000	0.128	1.000	1.000	1.000	1.000	1.000
	Hem * Cong	1.000	1.000	1.000	1.000	1.000	1.000	1.000	1.000	1.000	1.000	1.000	1.000	1.000	1.000	1.000	1.000	1.000	1.000	1.000	1.000	0.227	1.000	1.000	1.000	1.000	1.000	1.000	1.000	1.000	1.000	1.000
	Hem * Laterality	1.000	0.746	1.000	1.000	1.000	1.000	1.000	1.000	1.000	1.000	1.000	1.000	1.000	1.000	1.000	1.000	1.000	1.000	1.000	1.000	1.000	1.000	1.000	1.000	1.000	1.000	1.000	1.000	1.000	1.000	1.000
	Cong * Laterality	0.065	0.096	1.000	1.000	1.000	0.009	0.000	0.000	0.000	0.000	0.000	0.000	0.000	0.000	0.000	0.000	0.165	0.096	1.000	0.368	0.005	0.199	1.000	0.365	0.118	0.089	0.418	0.038	0.299	0.534	0.119
	Hem * Cong * Laterality	1.000	1.000	1.000	1.000	1.000	1.000	1.000	1.000	1.000	1.000	1.000	1.000	0.026	0.527	1.000	1.000	1.000	1.000	1.000	1.000	1.000	1.000	1.000	1.000	1.000	1.000	1.000	1.000	1.000	1.000	1.000
3	Hemisphere	0.366	1.000	1.000	1.000	1.000	1.000	1.000	0.011	0.025	0.619	0.460	1.000	1.000	1.000	0.001	1.000	0.427	0.013	0.001	0.001	0.190	0.022	0.056	1.000	0.002	0.050	1.000	1.000	1.000	1.000	1.000
	Congruence	1.000	1.000	1.000	1.000	1.000	1.000	1.000	1.000	1.000	1.000	1.000	1.000	1.000	1.000	1.000	1.000	1.000	1.000	1.000	1.000	1.000	1.000	1.000	1.000	1.000	1.000	0.763	1.000	1.000	0.228	1.000
	Laterality	1.000	0.577	1.000	1.000	1.000	1.000	1.000	1.000	1.000	1.000	0.089	0.252	1.000	1.000	1.000	1.000	1.000	1.000	0.980	1.000	1.000	1.000	1.000	1.000	1.000	1.000	1.000	1.000	0.759	0.318	1.000
	Hem * Cong	1.000	0.178	0.369	1.000	1.000	1.000	1.000	1.000	1.000	1.000	1.000	1.000	1.000	1.000	1.000	1.000	0.648	0.782	1.000	1.000	1.000	1.000	1.000	1.000	1.000	1.000	0.710	0.045	0.000	0.782	1.000
	Hem * Laterality	1.000	1.000	1.000	1.000	1.000	1.000	0.278	1.000	1.000	1.000	1.000	1.000	1.000	1.000	1.000	1.000	1.000	0.621	1.000	0.404	1.000	1.000	1.000	1.000	1.000	1.000	1.000	1.000	1.000	1.000	1.000
	Cong * Laterality	1.000	1.000	1.000	1.000	1.000	1.000	0.219	1.000	0.243	0.076	1.000	1.000	1.000	0.198	1.000	1.000	1.000	1.000	1.000	1.000	1.000	1.000	1.000	1.000	1.000	1.000	1.000	1.000	1.000	1.000	1.000
	Hem * Cong * Laterality	1.000	1.000	1.000	1.000	1.000	1.000	1.000	1.000	1.000	0.641	1.000	1.000	1.000	1.000	1.000	1.000	1.000	1.000	1.000	1.000	1.000	1.000	1.000	1.000	1.000	1.000	1.000	1.000	1.000	1.000	1.000

Table S2 – IOR-related neural activity in the cue time-window. Holm corrected p-values for the 3-way ANOVA testing the effects of Congruence, Hemisphere and Target-side on the HFBB signal in the long-SOA condition in Cluster 1 (yellow), Cluster 2 (red) and Cluster 3 (green). Significant effects in shaded color.

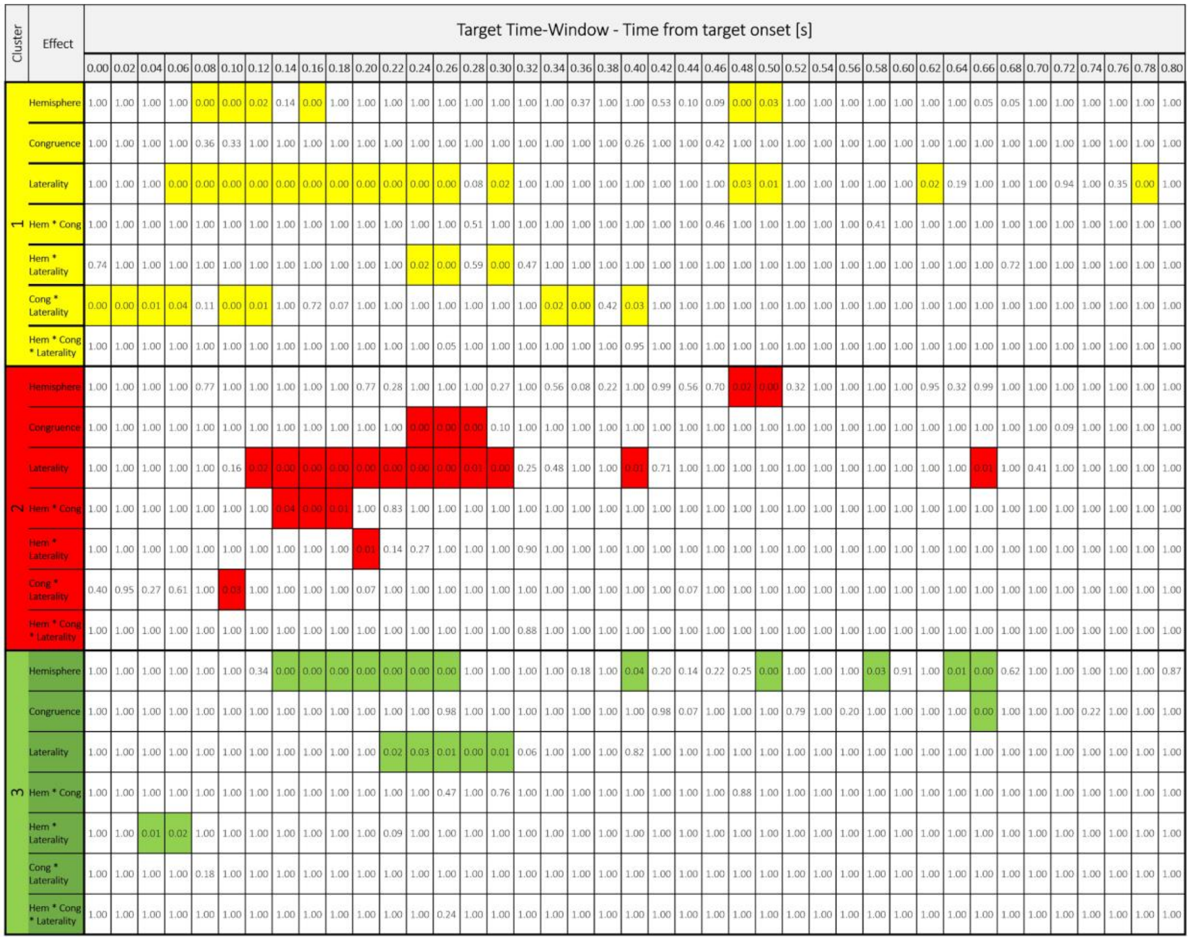

Cluster	Effect	Target Time-Window - Time from target onset [s]																																								
		0.00	0.02	0.04	0.06	0.08	0.10	0.12	0.14	0.16	0.18	0.20	0.22	0.24	0.26	0.28	0.30	0.32	0.34	0.36	0.38	0.40	0.42	0.44	0.46	0.48	0.50	0.52	0.54	0.56	0.58	0.60	0.62	0.64	0.66	0.68	0.70	0.72	0.74	0.76	0.78	0.80
1	Hemisphere	1.00	1.00	1.00	1.00	0.00	0.00	0.02	0.14	0.00	1.00	1.00	1.00	1.00	1.00	1.00	1.00	1.00	1.00	0.37	1.00	1.00	0.53	0.10	0.09	0.00	0.03	1.00	1.00	1.00	1.00	1.00	1.00	1.00	0.05	0.05	1.00	1.00	1.00	1.00	1.00	1.00
	Congruence	1.00	1.00	1.00	1.00	0.36	0.33	1.00	1.00	1.00	1.00	1.00	1.00	1.00	1.00	1.00	1.00	1.00	1.00	1.00	1.00	0.26	1.00	1.00	0.42	1.00	1.00	1.00	1.00	1.00	1.00	1.00	1.00	1.00	1.00	1.00	1.00	1.00	1.00	1.00	1.00	1.00
	Laterality	1.00	1.00	1.00	0.00	0.00	0.00	0.00	0.00	0.00	0.00	0.00	0.00	0.00	0.00	0.08	0.02	1.00	1.00	1.00	1.00	1.00	1.00	1.00	1.00	0.03	0.01	1.00	1.00	1.00	1.00	1.00	0.02	0.19	1.00	1.00	1.00	0.94	1.00	0.35	0.00	1.00
	Hem * Cong	1.00	1.00	1.00	1.00	1.00	1.00	1.00	1.00	1.00	1.00	1.00	1.00	1.00	1.00	0.51	1.00	1.00	1.00	1.00	1.00	1.00	1.00	1.00	0.46	1.00	1.00	1.00	1.00	1.00	0.41	1.00	1.00	1.00	1.00	1.00	1.00	1.00	1.00	1.00	1.00	1.00
	Hem * Laterality	0.74	1.00	1.00	1.00	1.00	1.00	1.00	1.00	1.00	1.00	1.00	1.00	0.02	0.00	0.59	0.00	0.47	1.00	1.00	1.00	1.00	1.00	1.00	1.00	1.00	1.00	1.00	1.00	1.00	1.00	1.00	1.00	1.00	1.00	0.72	1.00	1.00	1.00	1.00	1.00	1.00
	Cong * Laterality	0.00	0.00	0.01	0.04	0.11	0.00	0.01	1.00	0.72	0.07	1.00	1.00	1.00	1.00	1.00	1.00	1.00	0.02	0.00	0.42	0.03	1.00	1.00	1.00	1.00	1.00	1.00	1.00	1.00	1.00	1.00	1.00	1.00	1.00	1.00	1.00	1.00	1.00	1.00	1.00	1.00
	Hem * Cong * Laterality	1.00	1.00	1.00	1.00	1.00	1.00	1.00	1.00	1.00	1.00	1.00	1.00	1.00	0.05	1.00	1.00	1.00	1.00	1.00	1.00	0.95	1.00	1.00	1.00	1.00	1.00	1.00	1.00	1.00	1.00	1.00	1.00	1.00	1.00	1.00	1.00	1.00	1.00	1.00	1.00	1.00
2	Hemisphere	1.00	1.00	1.00	1.00	0.77	1.00	1.00	1.00	1.00	1.00	0.77	0.28	1.00	1.00	1.00	0.27	1.00	0.56	0.08	0.22	1.00	0.99	0.56	0.70	0.02	0.00	0.32	1.00	1.00	1.00	1.00	0.95	0.32	0.99	1.00	1.00	1.00	1.00	1.00	1.00	1.00
	Congruence	1.00	1.00	1.00	1.00	1.00	1.00	1.00	1.00	1.00	1.00	1.00	1.00	0.00	0.00	0.00	0.10	1.00	1.00	1.00	1.00	1.00	1.00	1.00	1.00	1.00	1.00	1.00	1.00	1.00	1.00	1.00	1.00	1.00	1.00	1.00	1.00	0.09	1.00	1.00	1.00	1.00
	Laterality	1.00	1.00	1.00	1.00	1.00	0.16	0.02	0.00	0.00	0.00	0.00	0.00	0.00	0.00	0.01	0.00	0.25	0.48	1.00	1.00	0.01	0.71	1.00	1.00	1.00	1.00	1.00	1.00	1.00	1.00	1.00	1.00	1.00	0.01	1.00	0.41	1.00	1.00	1.00	1.00	1.00
	Hem * Cong	1.00	1.00	1.00	1.00	1.00	1.00	1.00	0.04	0.00	0.01	1.00	0.83	1.00	1.00	1.00	1.00	1.00	1.00	1.00	1.00	1.00	1.00	1.00	1.00	1.00	1.00	1.00	1.00	1.00	1.00	1.00	1.00	1.00	1.00	1.00	1.00	1.00	1.00	1.00	1.00	1.00
	Hem * Laterality	1.00	1.00	1.00	1.00	1.00	1.00	1.00	1.00	1.00	1.00	0.01	0.14	0.27	1.00	1.00	1.00	0.90	1.00	1.00	1.00	1.00	1.00	1.00	1.00	1.00	1.00	1.00	1.00	1.00	1.00	1.00	1.00	1.00	1.00	1.00	1.00	1.00	1.00	1.00	1.00	1.00
	Cong * Laterality	0.40	0.95	0.27	0.61	1.00	0.03	1.00	1.00	1.00	1.00	0.07	1.00	1.00	1.00	1.00	1.00	1.00	1.00	1.00	1.00	1.00	1.00	0.07	1.00	1.00	1.00	1.00	1.00	1.00	1.00	1.00	1.00	1.00	1.00	1.00	1.00	1.00	1.00	1.00	1.00	1.00
	Hem * Cong * Laterality	1.00	1.00	1.00	1.00	1.00	1.00	1.00	1.00	1.00	1.00	1.00	1.00	1.00	1.00	1.00	1.00	0.88	1.00	1.00	1.00	1.00	1.00	1.00	1.00	1.00	1.00	1.00	1.00	1.00	1.00	1.00	1.00	1.00	1.00	1.00	1.00	1.00	1.00	1.00	1.00	1.00
3	Hemisphere	1.00	1.00	1.00	1.00	1.00	1.00	0.34	0.00	0.00	0.00	0.00	0.00	0.00	0.00	1.00	1.00	1.00	1.00	0.18	1.00	0.04	0.20	0.14	0.22	0.25	0.00	1.00	1.00	1.00	0.03	0.91	1.00	0.01	0.00	0.62	1.00	1.00	1.00	1.00	1.00	0.87
	Congruence	1.00	1.00	1.00	1.00	1.00	1.00	1.00	1.00	1.00	1.00	1.00	1.00	1.00	0.98	1.00	1.00	1.00	1.00	1.00	1.00	1.00	0.98	0.07	1.00	1.00	1.00	0.79	1.00	0.20	1.00	1.00	1.00	1.00	0.00	1.00	1.00	1.00	0.22	1.00	1.00	1.00
	Laterality	1.00	1.00	1.00	1.00	1.00	1.00	1.00	1.00	1.00	1.00	1.00	0.02	0.03	0.01	0.00	0.01	0.06	1.00	1.00	1.00	0.82	1.00	1.00	1.00	1.00	1.00	1.00	1.00	1.00	1.00	1.00	1.00	1.00	1.00	1.00	1.00	1.00	1.00	1.00	1.00	1.00
	Hem * Cong	1.00	1.00	1.00	1.00	1.00	1.00	1.00	1.00	1.00	1.00	1.00	1.00	1.00	0.47	1.00	0.76	1.00	1.00	1.00	1.00	1.00	1.00	1.00	1.00	0.88	1.00	1.00	1.00	1.00	1.00	1.00	1.00	1.00	1.00	1.00	1.00	1.00	1.00	1.00	1.00	1.00
	Hem * Laterality	1.00	1.00	0.01	0.02	1.00	1.00	1.00	1.00	1.00	1.00	1.00	0.09	1.00	1.00	1.00	1.00	1.00	1.00	1.00	1.00	1.00	1.00	1.00	1.00	1.00	1.00	1.00	1.00	1.00	1.00	1.00	1.00	1.00	1.00	1.00	1.00	1.00	1.00	1.00	1.00	1.00
	Cong * Laterality	1.00	1.00	1.00	1.00	0.18	1.00	1.00	1.00	1.00	1.00	1.00	1.00	1.00	1.00	1.00	1.00	1.00	1.00	1.00	1.00	1.00	1.00	1.00	1.00	1.00	1.00	1.00	1.00	1.00	1.00	1.00	1.00	1.00	1.00	1.00	1.00	1.00	1.00	1.00	1.00	1.00
	Hem * Cong * Laterality	1.00	1.00	1.00	1.00	1.00	1.00	1.00	1.00	1.00	1.00	1.00	1.00	1.00	0.24	1.00	1.00	1.00	1.00	1.00	1.00	1.00	1.00	1.00	1.00	1.00	1.00	1.00	1.00	1.00	1.00	1.00	1.00	1.00	1.00	1.00	1.00	1.00	1.00	1.00	1.00	1.00

Table S3 – IOR-related neural activity in the Target time-window. Holm corrected p-values for the 3-way ANOVA testing the effects of Congruence, Hemisphere and Target-side on the HFBB signal in the long-SOA condition in Cluster 1 (yellow), Cluster 2 (red) and Cluster 3 (green). Significant effects in shaded color.

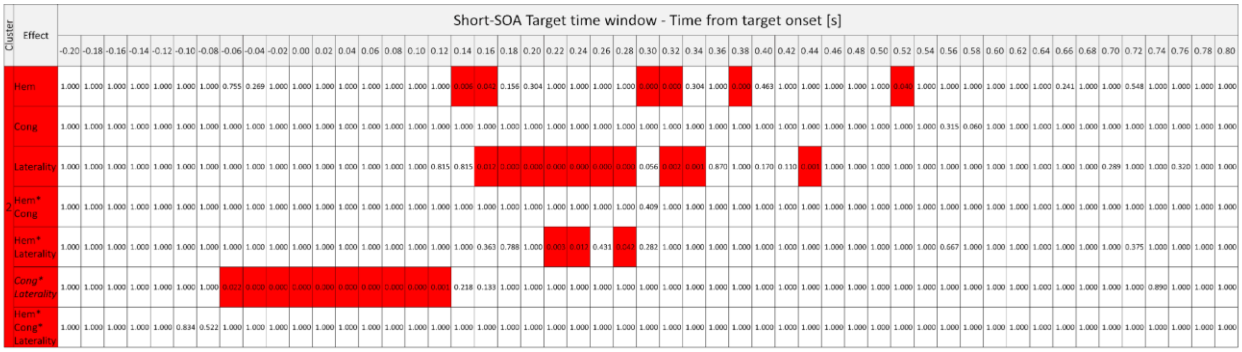

Cluster	Effect	Short-SOA Target time window - Time from target onset [s]																
		-0.20	-0.18	-0.16	-0.14	-0.12	-0.10	-0.08	-0.06	-0.04	-0.02	0.00	0.02	0.04	0.06	0.08	0.10	0.12
2	Hem	1.000	1.000	1.000	1.000	1.000	1.000	1.000	0.755	0.269	1.000	1.000	1.000	1.000	1.000	1.000	1.000	1.000
	Cong	1.000	1.000	1.000	1.000	1.000	1.000	1.000	1.000	1.000	1.000	1.000	1.000	1.000	1.000	1.000	1.000	1.000
	Laterality	1.000	1.000	1.000	1.000	1.000	1.000	1.000	1.000	1.000	1.000	1.000	1.000	1.000	1.000	1.000	1.000	0.815
	Hem* Cong	1.000	1.000	1.000	1.000	1.000	1.000	1.000	1.000	1.000	1.000	1.000	1.000	1.000	1.000	1.000	1.000	1.000
	Hem* Laterality	1.000	1.000	1.000	1.000	1.000	1.000	1.000	1.000	1.000	1.000	1.000	1.000	1.000	1.000	1.000	1.000	1.000
	Cong Laterality*	1.000	1.000	1.000	1.000	1.000	1.000	1.000	0.022	0.000	0.000	0.000	0.000	0.000	0.000	0.000	0.000	0.001
	Hem* Cong* Laterality	1.000	1.000	1.000	1.000	1.000	0.834	0.522	1.000	1.000	1.000	1.000	1.000	1.000	1.000	1.000	1.000	1.000

Cluster	Effect	0.14	0.16	0.18	0.20	0.22	0.24	0.26	0.28	0.30	0.32	0.34	0.36	0.38	0.40	0.42	0.44	0.46
2	Hem	0.006	0.042	0.156	0.304	1.000	1.000	1.000	1.000	0.000	0.000	0.304	1.000	0.000	0.463	1.000	1.000	1.000
	Cong	1.000	1.000	1.000	1.000	1.000	1.000	1.000	1.000	1.000	1.000	1.000	1.000	1.000	1.000	1.000	1.000	1.000
	Laterality	0.815	0.012	0.000	0.000	0.000	0.000	0.000	0.000	0.056	0.002	0.001	0.870	1.000	0.170	0.110	0.001	1.000
	Hem* Cong	1.000	1.000	1.000	1.000	1.000	1.000	1.000	1.000	0.409	1.000	1.000	1.000	1.000	1.000	1.000	1.000	1.000
	Hem* Laterality	1.000	0.363	0.788	1.000	0.003	0.012	0.431	0.042	0.282	1.000	1.000	1.000	1.000	1.000	1.000	1.000	1.000
	Cong Laterality*	0.218	0.133	1.000	1.000	1.000	1.000	1.000	1.000	1.000	1.000	1.000	1.000	1.000	1.000	1.000	1.000	1.000
	Hem* Cong* Laterality	1.000	1.000	1.000	1.000	1.000	1.000	1.000	1.000	1.000	1.000	1.000	1.000	1.000	1.000	1.000	1.000	1.000

Cluster	Effect	0.48	0.50	0.52	0.54	0.56	0.58	0.60	0.62	0.64	0.66	0.68	0.70	0.72	0.74	0.76	0.78	0.80
2	Hem	1.000	1.000	0.040	1.000	1.000	1.000	1.000	1.000	1.000	0.241	1.000	1.000	0.548	1.000	1.000	1.000	1.000
	Cong	1.000	1.000	1.000	1.000	0.315	0.060	1.000	1.000	1.000	1.000	1.000	1.000	1.000	1.000	1.000	1.000	1.000
	Laterality	1.000	1.000	1.000	1.000	1.000	1.000	1.000	1.000	1.000	1.000	1.000	0.289	1.000	1.000	0.320	1.000	1.000
	Hem* Cong	1.000	1.000	1.000	1.000	1.000	1.000	1.000	1.000	1.000	1.000	1.000	1.000	1.000	1.000	1.000	1.000	1.000
	Hem* Laterality	1.000	1.000	1.000	1.000	0.667	1.000	1.000	1.000	1.000	1.000	1.000	1.000	0.375	1.000	1.000	1.000	1.000
	Cong Laterality*	1.000	1.000	1.000	1.000	1.000	1.000	1.000	1.000	1.000	1.000	1.000	1.000	1.000	0.890	1.000	1.000	1.000
	Hem* Cong* Laterality	1.000	1.000	1.000	1.000	1.000	1.000	1.000	1.000	1.000	1.000	1.000	1.000	1.000	1.000	1.000	1.000	1.000

Table S4 – Short-SOA Congruence-related neural activity in the Target time-window in Cluster 2. Holm corrected p-values for the 3-way ANOVA testing the effects of Congruence, Hemisphere and Target-side on the HFBB signal in the short-SOA condition. Significant effects in shaded red.

Figure Legends

Figure 1 - Neurotypical performance of implanted patients in the Posner task. (A) Illustration of the Posner cued detection task. After 1000ms of fixation, a cue (thickened placeholder) appeared for 100ms at either side of the screen. On short SOA trials (short-SOA), the target (the letter X) occurred 150ms after cue onset; on long SOA trials (long-SOA) the target appeared 600ms after cue onset. The target appeared either on the same side of the screen as the cue (Congruent condition), or on the opposite site (Incongruent condition). Patients were required to press a central button with their right hand, as soon as the target appeared, while maintaining central fixation throughout stimuli presentation. Catch trials (n=24) had the same duration and cue presentation, but no target followed the cue. All trial types (n=336) were equiprobable and randomly interleaved. Stimuli are not drawn to scale. (B) Patients' performance is neurotypical. 2-way-ANOVA, * p=0.047; ** p=0.008; *** p<0.001. Error bars represent normalized SEM. n=28 independent participants.

Figure 2 - Contact localization and trajectory clustering. (A) Left: Illustration of the localization in normalized space (MNI152) of the contacts included in the analysis (black circles; n=1,403) in the left hemisphere (LH; n=671) and in the right hemisphere (RH, n=732), pooled across patients. Each localization is the mean coordinates of the two contacts composing the contact's bipolar montage. To reveal prototypical temporal patterns simultaneously across all conditions, the trajectories across the 8 condition dimensions of the mean high-frequency broadband (HFBB) target-locked activity of 664 significantly responsive contacts (significant time-point-by-time-point t-test for at least 100ms in one of the experimental conditions compared to baseline), were clustered using a custom-made trajectory K-means approach. Right: Example of target-locked mean normalized HFBB responses of one contact in the right angular gyrus in Congruent (full lines) and Incongruent (dashed lines) trials, at short-SOA (blue) and long-SOA (red), with targets contralateral or ipsilateral to the contact. Dashed vertical lines represent onsets of target (black), and short-SOA (blue) and long-SOA (red) cues. Shaded areas represent SEM across trials. (B) Prototypical temporal profiles of contact clusters across conditions: Trimmed-mean target-locked activity profiles of three contact clusters, across the 8 conditions (Congruent / Incongruent Trial X short-SOA / long-SOA X Ipsilateral target (Ipsi) / contralateral target (Contra)). Cluster 1 (yellow) shows contralateral fast responses, with cue-target activity segregation at both SOAs; Cluster 2 (red) shows bilateral slower responses with spatial sensitivity, with cue-target activity segregation at long-SOA but response integration in short-SOA; and Cluster 3 (green) shows bilateral slowest responses with stimulus-type sensitivity, with cue-target activity segregation at long-SOA but response integration at short-SOA. Dashed vertical lines represent target onset (black) and cue onset at short-SOA (blue) and long-SOA (red). (C) Temporal gradient of target-locked activity (trimmed-mean) of the three clusters. Black dashed line depicts target onset. (D) Scatter plot of peak times of mean target-locked activity of contacts of Cluster 1 (yellow circles), Cluster 2 (red circles) and Cluster 3 (green circles), in Congruent (x-axis) and Incongruent (y-axis) conditions, showing a significant temporal gradient (Mixed 2-way ANOVA, Cluster main effect p<0.001, η^2=0.378; linear polynomial contrast: p≤0.001). Squares represent mean peak time; Dotted grey line denotes the equity line; Shaded areas represent peak time distributions.

Figure 3 – Clusters exhibit a spatiotemporal gradient. (A) Clusters' spatial profile. Illustration of the localization of the contacts composing each cluster: Cluster 1 (yellow), Cluster 2 (red), Cluster 3 (green). For each cluster, dots represent contacts' localization in dorsal (middle), lateral (top) and medial (bottom) views of the right hemisphere (RH; right) and of the left hemisphere (LH; left). (B) Core-Periphery gradient: Clusters' anatomical localization follows Core-Periphery gradients [51], where the Cluster 1's contacts are the most peripheral and the Cluster 3's contacts are closest to core regions. (C) Left: Scatter plot of contacts localization along

core-periphery gradients (Cluster 1 - yellow circles, n=62 independent contacts; Cluster 2 - red circles, n=97 independent contacts; Cluster 3 – green circles, n=67 independent contacts; rectangles represent clusters' mean). Right: Violin plots of contacts localization along Core-Periphery gradients for Cluster 1 (yellow), Cluster 2 (red) and Cluster 3 (green), showing a significant core-periphery gradient (Gradient 1: 1-way ANOVA, $p<0.001$, $\eta^2=0.06$; linear polynomial contrast: $p\leq0.001$; Gradient 2: 1-way ANOVA, $p<0.001$, $\eta^2=0.28$; linear polynomial contrast: $p\leq0.001$; n=232 independent contacts in total). The box centerlines depict the medians, the bounds of the box depict the 75%/25% quartiles and the whiskers depict the top & bottom 25% percentiles. (D) Cluster contacts are structurally connected: Corrected tractography t-maps, showing the significant white matter voxels, which connect pre and post rolandic contacts within each cluster (Cluster 1 – yellow; Cluster 2 - red, Cluster 3 - green), derived from a fiber tracking analysis of 176 healthy individuals. (E) Contacts' receptive windows lengthen along the cluster gradient: Raincloud plots of individual contacts' receptive window length (circles), showing a significant linear lengthening from Cluster 1 (yellow, n=62 independent contacts), to Cluster 2 (red, n=97 independent contacts), to Cluster 3 (green, n=67 independent contacts; 1-way ANOVA: $p<0.001$, $\eta^2=0.11$; linear polynomial contrast: $p\leq0.001$; n=232 independent contacts in total). The box centerlines depict the medians, the bounds of the box depict the 75%/25% quartiles and the whiskers depict the top & bottom 25% percentiles.

Figure 4 - IOR-related neural activity. Mean target-locked long-SOA activity in Cluster 1 (yellow), Cluster 2 (red) and Cluster 3 (green), computed over trials pooled across all cluster contacts, for Congruent trials (full lines) and Incongruent trials (dashed lines). (A) In the Cluster 1, no significant Congruence effect was observed in a 3-way ANOVA with Holm multiple comparisons correction. (B) In Cluster 2 activity in Congruent and Incongruent trials (IOR-related) differed significantly in a 3-way ANOVA with Holm multiple comparisons correction at 0.24-0.3s post target (shaded red areas; Congruence main effect: largest $p=0.002$), and a significant hemispheric difference between IOR-related responses was observed at 0.14-.022s post target (shaded brown area; Hemisphere x Congruence interaction: largest $p=0.03$; Diagonally striped areas represent significant Congruence x Hemisphere post hoc comparisons ($p<0.05$)). (C) In Cluster 3 activity in Congruent and Incongruent trials differed significantly in a 3-way ANOVA with Holm multiple comparisons correction at 0.66-0.68s post target (green shaded area; Congruence main effect: largest $p=0.003$). A-C. Shaded areas around traces depict SEM; Dashed vertical lines represent Target onset (black) and Cue onset (red) at the long-SOA Condition. (D) Representative examples of HFBB power IOR-related activity in the Congruent (full line) & Incongruent (dashed line) long-SOA conditions of individual contacts of the Cluster 2, shaded areas around traces depict SEM. p values are Holm corrected.

Figure 5 - RT & visual modulation of Target-locked & Response-locked neural activity. (A) RT modulates target-locked neural activity, pooled across conditions and color coded from fastest (Magenta) to slowest (yellow) RT bin. Dashed vertical black line represents target onset; Color-coded dots at the top of each panel represent mean RT for each bin (pink – fastest RT to yellow – slowest RT); 1-way repeated measures ANOVA, Holm multiple comparisons correction. Top: Late RT modulation of activity in Cluster 1 (yellow): Main effect of RT bin at 0.5-0.54 & 0.56-0.68s post-target (shaded yellow area;, largest $p=0.002$). Middle: RT modulation of neural response offset in Cluster 2 (red): Main effect of RT bin at 0.3-0.56s post target (shaded red area; largest $p=0.028$). Bottom: RT modulation of response in Cluster 3 (green): Main effect of RT bin at 0.28-0.3 and 0.4-0.42s post target (shaded green area; largest $p=0.007$). (B) Examples of single contact neural activity in the fastest (pink) & slowest (yellow) thirds of trials for the three target-locked clusters. Vertical dashed black lines represent target onset; Vertical full lines denote mean RT for fastest (magenta) & slowest (yellow) trials, shaded areas around traces depict SEM. (C) Visual modulation of response-locked neural activity pooled across conditions, color-coded from fastest (Magenta) to slowest (yellow) bin. Dashed vertical grey line represents RT; Color-coded dots at the top of each panel represent mean target onset time for each bin (pink – earliest onset to yellow – latest onset); 1-way repeated measures ANOVA, Holm multiple comparisons correction. Top: Target onset time modulates activity in the RT-Cluster 1 (yellow): Main effect of RT-bin at 0.12-0.10s pre-response (shaded yellow area; largest $p=0.04$). Target onset time modulates activity in the RT-Cluster 2a (orange): Main effect of RT bin at 0.70-0.68s, 0.52-0.50s & 0.30-0.20s pre-response (shaded orange area; largest $p=0.004$). No significant modulation in RT-Cluster 2b (turquoise) & RT-Cluster 3 (green). Arrows between panels (A) & (C) denote the contingency between Target-locked & Response-locked clusters (see Fig. S10). (D) Examples of single contact neural activity in the fastest (pink) & slowest (yellow) thirds of trials for RT-Cluster 1 and RT-Cluster 2a. Vertical dashed grey lines represent RT; Vertical full lines denote mean target onset time for fastest (magenta) & slowest (yellow) trials, shaded areas around traces depict SEM. *p* values are Holm corrected.

Supplementary Results

Clusters' hemispheric lateralization

To test if the clusters' spatial distribution differs between right and left hemispheres, we performed a χ^2 analysis only in symmetrically covered regions (see methods), that revealed a significant lateralization

($\chi^2(5)=29.09$, $p<0.001$). Post hoc comparisons showed that this effect resulted from a significant right lateralization of Cluster 2 and a significant left lateralization of Cluster 3 (post hoc binomial tests, $p=0.01$ and $p=0.003$).

Cue time-window long-SOA effects

Cluster 1 responded only for contralateral cues (Congruence x Laterality interaction: -580 to -360ms, -180 to -60ms, -40 – 0ms pre target; largest $p=0.038$; see Fig. S6), reflecting the presence of a cue contralateral to the recording contact only in Incongruent contralateral and Congruent ipsilateral target trials, and demonstrating the visual processing properties of this cluster. Cluster 2 responded to both contralateral and ipsilateral cues but with stronger responses for cues presented contralaterally to the recording contact and with a later latency than in Cluster 1, demonstrating this cluster's spatial sensitivty (Congruence x Laterality interaction: -520 to -300ms, -220 to -200ms, -80 to -60ms pre target onset; largest $p=0.03$). Clusters 1 and 2 also showed a short triple interaction effect, (Congruence x Laterality x Hemisphere interaction; Cluster 1: -420 to -400ms; largest $p=0.044$; Cluster 2: -380 to -360ms; largest $p=0.026$). Congruence x Laterality interaction effect did not reach significance in Cluster 3, yet this cluster showed slightly stronger response for Incongruent trials compared to Congruent trials in the left hemisphere more than in the right hemisphere (Congruence x Hemisphere interaction: -80 to -40ms pre target onset; largest $p=0.046$).

Cross correlation of target-locked activity

To validate the association between cluster neural activity timing and RT we calculated the cross-correlation of target-locked neural activity across RT-bins. We computed the cross-correlation between activity at the fastest RT-bin and all subsequent bins in each condition for each cluster. If cluster activity is target-associated, maximal cross-correlation will be centered on target onset, resulting in a zero shift across all RT bins (Fig. S9). If cluster activity is response-associated, maximal cross-correlation will follow the RT, resulting in a negative shift of cross-correlation lag. To test if the lag in which the cross correlation was maximal corresponded to the RT we calculated the Pearson correlation between them. In Cluster 1, cross-correlation coefficients were centered on zero, and there was no correlation between the maximal lag and RT, suggesting that Cluster 1 activity is target-associated. In Cluster 2 and 3, cross-correlation coefficients showed a negative shifted lag that was generally correlated with RT, indicating that these clusters are response-associated.

Cross correlation of response-locked activity

To validate the association between cluster neural activity timing and target onset time we calculated the cross-correlation of response-locked neural activity across RT-bins. We computed the cross-correlation between activity at the fastest RT-bin and all subsequent bins in each condition for each cluster. If cluster activity is target-associated, maximal cross-correlation will follow the RT (here indicative of quantile's mean target-onset time), resulting in a positive shift of cross-correlation lag (Fig. S12). If cluster activity is response-associated, maximal cross-correlation will be centered on target onset, resulting in a zero shift across all RT bins. To test if the lag in which the cross correlation was maximal corresponded to target onset we calculated the Pearson correlation between the lag and RT. In RT-Cluster 1 and RT-Cluster 2a, cross-correlation coefficients were positively shifted in a spatially sensitive manner, i.e. only for contralateral targets and there were significant ($p<0.05$) positive correlations, only for contralateral targets, indicating that their activity showed visual modulation. In RT-Cluster 2b and RT-Cluster 3, cross-correlation coefficients showed no shift and were not correlated with the RT, thus their activity is response-associated.

Theta-phase dependence of neural activity

To test the hypothesis that the potential role of theta-phase in driving the observed behavioral effects. In response, we conducted an extensive analysis to investigate this possibility. To address this hypothesis, we systematically compared the alignment of the instantaneous theta phase at the onset of the Target stimulus (extracted from the raw unfiltered data using a hilbert transform) between conditions with different SOAs and congruence levels. Our analysis involved a mixed ANOVA with repeated-measures factors of SOA and Congruence, supplemented by a between-subjects factor of Cluster to test if the theta phase effect could arise differentially across different contact clusters. We could not reject the null hypothesis for any of the factors, or their interactions (SOA: *F*(1,1348)=0.049, p=0.83; Congruence: *F*(1,1348)=0.38, *p*=0.54; Cluster: *F*(6,1348)=0.24, *p*=0.97; SOA*Cluster: *F*(6,1348)=0.26, *p*=0.96; Congruence*Cluster: *F*(6,1348)=0.166, *p*=0.97; SOA*Congruence: *F*(1,1348)=6.17*10-5, *p*=0.99; SOA*Congruence*Cluster: *F*(1,1348)=0.33, *p*=0.92). A Bayesian ANOVA with the same factors (specifying a multivariate Cauchy prior on the effect [98] confirmed these negative findings, showing that the null model was the best supported one, with 7.1 (BF01) more evidence for the null compared to the next best model containing the SOA factor. These results suggest that the theta phase cannot explain the behavioral effects, not at the entire sample of contacts and not when looking into particular clusters of contacts.